# Thermoelectric Properties of $Bi_{1-x}Sb_x$ Nanowires Electrodeposited in Etched Ion-Track Membranes

Vom Fachbereich Material- und Geowissenschaften

der Technischen Universität Darmstadt

TECHNISCHE UNIVERSITÄT DARMSTADT

zur Erklärung des akademischen Grades eines

Doktors der Ingenieurwissenschaften (Dr.-Ing.)

genehmigte

**Dissertation**

von

**M. Sc. Marco Cassinelli**

aus Mantova (Italien)

Darmstadt 2016

D17

Thermoelectric Properties of $Bi_{1-x}Sb_x$ Nanowires Electrodeposited in Etched Ion-Track Membranes

genehmigte Dissertation von M. Sc. Marco Cassinelli aus Mantova (Italien)

1. Gutachten: Prof. Dr. Christina Trautmann
2. Gutachten: Prof. Dr. Wolfgang Ensinger

Tag der Einreichung: 22.03.2016
Tag der Prüfung: 15.06.2016

Darmstadt – D17

URN: urn:nbn:de:tuda-tuprints-55440

URI: http://tuprints.ulb.tu-darmstadt.de/id/eprint/5544

## Erklärung zur Dissertation

Hiermit versichere ich, die vorliegende Dissertation ohne Hilfe Dritter und nur mit den angegebenen Quellen und Hilfsmitteln angefertigt zu haben. Alle Stellen, die aus den Quellen entnommen wurden, sind als solche kenntlich gemacht worden. Diese Arbeit hat in dieser oder ähnlicher Form noch keiner Prüfungsbehörde vorgelegen.

Darmstadt, den

_____

(Marco Cassinelli)

*“Life is beautiful”*

# Zusammenfassung

Die einzigartigen Eigenschaften von Bismut-Antimon ($Bi_{1-x}Sb_x$) Nanostrukturen und die theoretische Vorhersagen über ihre verbesserte Thermoeffizienz lösten vor zwei Jahrzehnten die Entwicklung einer Vielzahl von Synthese und Charakterisierungsmethoden aus, die auf die Messungen der thermoelektrische Eigenschaften von $Bi_{1-x}Sb_x$ Nanodrähten abzielten. Dennoch ist die experimentelle Demonstration einer größenabhängigen Thermoeffizienz noch nicht aufgezeigt worden. Die Schwierigkeiten beruhen auf der Herstellung von gut definierten Nanodraht-Systemen und der Realisierung von zuverlässigen und stabilen elektrischen und thermischen Kontakten.

In dieser Arbeit wurden $Bi_{1-x}Sb_x$ Nanodraht- Arrays mit kontrollierter chemischer Zusammensetzung ($0 \leq x \leq 1$) und Durchmessern (von ~ 750 bis ~ 40 nm) durch gepulste galvanische Abscheidung in geätzten Ionenspurmembranen synthetisiert. Die thermoelektrischen Eigenschaften von $Bi_{1-x}Sb_x$ Materialen werden stark durch die anisotrope Struktur beeinflusst. Aus diesem Grund wurde besondere Aufmerksamkeit bei der Untersuchung des Einflusses der Abscheidebedingungen auf die Kristallorientierung und Zusammensetzung der Drähte für verschiedene Durchmesser gelegt. Zur Charakterisierung der Nanodrähten wurden unterschiedliche Methoden angewandt, einschließlich Röntgenbeugung, Rasterelektronenmikroskopie (SEM) und Transmissionselektronenmikroskopie (TEM).

Systematische Messungen des Seebeck-Koeffizienten und des elektrischen Widerstands von vorab charakterisierten $Bi_{1-x}Sb_x$ Nanodrähten unterschiedlicher Zusammensetzung und Durchmessern wurde im Temperaturbereich zwischen 300 und 20 K durchgeführt. Für abnehmende Drahtdurchmesser sind die Seebeck-Koeffizienten nicht-monoton. Dieses Verhalten ist durch den Einfluss von Oberflächenzuständen sowie Quanten- und klassische-Größen Effekte erklärbar.

Schließlich wurde die chemische und thermische Stabilität der $Bi_{1-x}Sb_x$ Nanodrähte in Luft sowohl bei Raum- und bei mäßigen Temperaturen untersucht. Nach der Temperaturbehandlung zeigen die Nanodrähte die rasche Bildung einer Metalloxidphase. Der Oxidationsprozess führt bereits bei niedrigen Temperaturen zu einem Anstieg der Oberflächenrauigkeit und zur Bildung von Protuberanzen bei 250° C. Diese Ergebnisse zur Oxidation erklären die häufig in der Literatur berichteten hohen Widerstandswerte und die Schwierigkeiten, einzelne $Bi_{1-x}Sb_x$ Nanodrähte elektrisch zu kontaktieren.

# Abstract

The unique properties exhibited by bismuth antimony ($Bi_{1-x}Sb_x$) nanostructures and the theoretical predictions on their enhanced thermoelectric efficiency two decades ago triggered the development of a wide variety of growth and characterization methods aiming at measuring the thermoelectric properties of $Bi_{1-x}Sb_x$ nanowires. However, the experimental demonstration of a size-dependent thermoelectric efficiency is still challenged by the difficulties to fabricate well-defined nanowire systems and to achieve reliable and stable electrical and thermal contacts.

In this work, $Bi_{1-x}Sb_x$ nanowire arrays with controlled wire composition ($0 \leq x \leq 1$) and diameter (from ~ 750 to ~ 40 nm) were synthesized by pulsed electrodeposition in etched ion-track membranes. The thermoelectric properties of $Bi_{1-x}Sb_x$ are strongly influenced by the anisotropic structure of the material. Thus, special consideration was taken in studying the influence of the electrodeposition conditions on the crystallographic orientation and composition of the wires for various diameters. To characterize the wires several methods were applied, including X-ray diffraction and both scanning (SEM) and transmission electron microscopy (TEM).

Using such pre-characterized $Bi_{1-x}Sb_x$ nanowires, measurements of the Seebeck coefficient and electrical resistance were performed in the temperature between 300 and 20 K and for a systematic variation of the composition and diameter of the wires. The Seebeck coefficient values show a non-monotonic behavior when decreasing the wire diameter, which is explained by taking into account the existence of surface states as well as quantum- and finite-size effects.

Finally, the chemical and thermal stability of the $Bi_{1-x}Sb_x$ nanowires was investigated in air both at room and moderate temperatures, revealing the rapid formation of a metal oxide phase. The oxidation process causes an increase of the nanowires surface roughness at low annealing temperatures, and the formation of protuberances at 250°C. Our results on oxidation explain the diverse and high resistance values available in literature and the difficulties to electrically contact single $Bi_{1-x}Sb_x$ nanowires reported by other group.

# Table of Contents

# 1. Introduction

The worldwide energy consumption is predicted to increase by 44% from 2006 to 2030 as both the world population and the demand of energy per capita is continuously growing [IEO09]. In addition, the unpredictability of the fuel market, as well as the negative effects on global warming have pointed out the necessity to find alternative cleaner ways to produce and save energy [Ome08, Els14]. The exploitation of natural renewable resources, like harvesting solar and wind energy [Xi07, Afs12, Kal12], and the recovery of heat waste from industrial processes and automobiles, via thermoelectric processes, are all under intensive investigation [Bel08, Szc11].

In fact, thermoelectric materials are able to convert thermal power into electrical energy and conversely, supplying a current through a thermoelectric device will generate a temperature gradient across the material to be used, e.g. for cooling applications [Vin10, Tri11]. Thermoelectric devices are very reliable since they are composed by all-solid-state units, without any moving fluids or mechanical parts. The pollution-free processes make them an attractive source of energy [Sny08, Tie13].

Today, ~ 70% of the energy is required for heating/cooling systems and electricity [Gmz12] and more than 60% of the global power is dissipated as waste heat [Fan13]. If only 10% of the waste heat could be recovered, the energy produced would be more than the sum of the most current renewable energy sources, such as solar, geothermal, wind and hydro energy [Fan13]. In fact, thermoelectrics is gaining interest because it can transform heat from power plants, factories, motor vehicles and even human body into functional electric power [Zue09, Yad11, Shi12].

## 1.1 Thermoelectrics

The field of thermoelectrics is known since the 19th century as a mean to convert thermal energy into electrical energy and vice-versa. The term thermoelectrics encompasses three different effects, namely, the Seebeck, Peltier and Thomson effects [Sel13]. The discovery of the thermoelectric effect is dated back to ~1821, when Thomas Johann Seebeck made experiments on circuits made from two dissimilar metals with junctions kept at different temperatures [See21]. He noticed a deflection on a compass magnet caused by a current induced in the circuit by the existing gradient of temperature. Since the velocity distribution of the electrons depends on the temperature, the electrons at the hot junction possess a larger velocity than at the cold junction. Thus, the electrons diffuse thermally to the cold end, causing the formation of an electric field inside the material.

Nowadays, the induction of voltage by a temperature gradient is known as Seebeck effect, and its magnitude is measured by the Seebeck coefficient or thermopower. The dependency of the built up electric field ($\vec{E}$) or voltage ($dU$) by the temperature gradient ( $\nabla_{\vec{r}}T$ or $dT$) is given by the Seebeck coefficient ($S$) as:

$$\vec{E} = S\,\nabla_{\vec{r}}T \quad or \quad dU = S\,dT\,. \tag{1.1}$$

Around ~1834, the French physicist Jean Charles Peltier observed that at the junction of two dissimilar metals, an applied current dissipated heat at one side and absorbed heat at the other side [Kas01]. This effect is evaluated by the Peltier coefficient ($\Pi$) which determines the rate of exchange heat ($\vec{Q}$) as a function of the applied current ($\vec{J}$), as:

$$\vec{Q} = \Pi\,\vec{J}\,. \tag{1.2}$$

In 1860, William Thomson, later known as Lord Kelvin, pointed out that these two effects are due to the intrinsic properties of the given material [Tho51]. Thus, in addition to Joule heating, heat absorption or emission occur proportional to the applied current and temperature gradient. The proportionality is described by the Thomson coefficient ($\tau$), defined as ($\tau = T\,\frac{dS}{dT}$).

The three coefficients are interconnected by the Kelvin relation:

$$\Pi = S\,T\,. \tag{1.3}$$

Figure 1.1 shows the scheme of thermoelectric devices based on the thermoelectric effect. The modules consist of p- and an n-type semiconductor legs connected electrically in series and thermally

in parallel. When a temperature difference is applied between the two ends of the legs, as in figure 1.1 (a), electrons and holes thermally diffuse and an electrical current is formed inside the circuit. This simple device demonstrates thermoelectric energy harvesting exploiting the Seebeck effect. Alternatively, by applying a current (figure 1.1 (b)), the Peltier effect causes a selective cooling or heating at the ends of the legs, which depends on the charge flow direction.

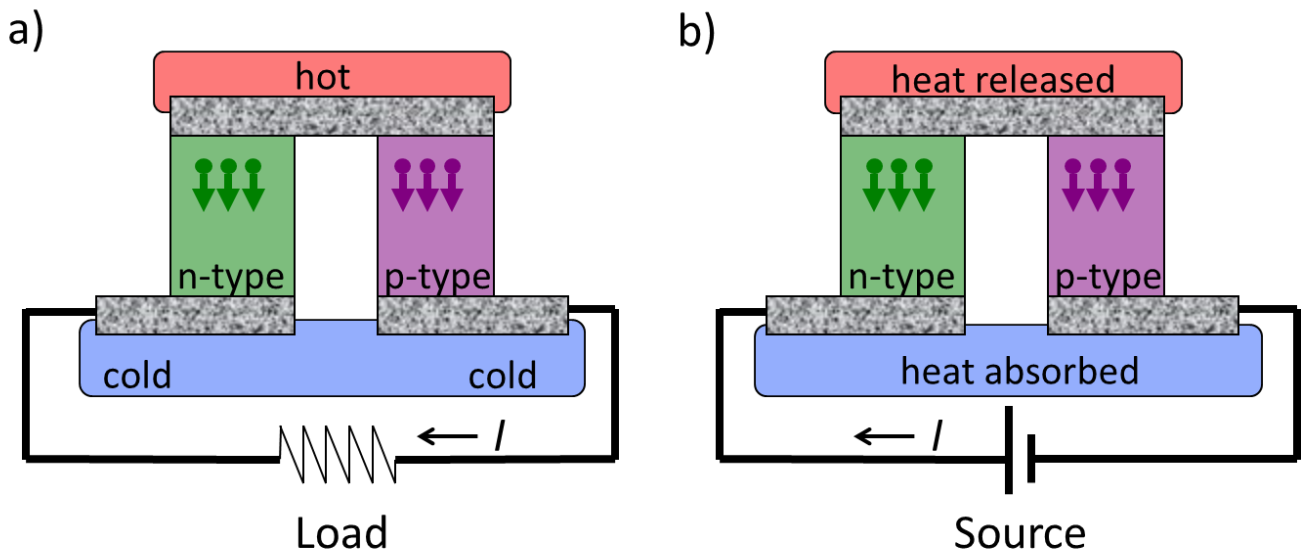


Figure 1.1: Schematic of simple thermoelectric modules with p- and n-type semiconducting leg for (a) energy generation applying a temperature gradient and (b) heating or cooling depending the on the direction of the current.

In 1949, Abraham Ioffe developed the modern theory of thermoelectrics, defining the so-called thermoelectric figure-of-merit *ZT* [Row06]. This figure of merit is a reference that allows to assess the thermoelectric efficiency of a material and to compare it with other materials. The figure-of-merit at a given temperature *T* is defined as:

$$Z\,T = \frac{S^2\sigma}{\kappa}\,T \tag{1.4}$$

$\kappa$ being the sum of the contributions of the charge carriers ($\kappa_e$) and the lattice thermal ($\kappa_L$) conductivity. For thermoelectric applications, materials with high *ZT* are desired.

This quantity is related to the efficiency ($\eta$) of a thermoelectric generator with two legs, which is given by [Row06]:

$$\eta = \frac{R_{ext}\, I^2}{(S_p - S_n) I\, T_h + \kappa(T_h - T_c) - \frac{1}{2} R_{mat}\, I^2} \quad , \tag{1.5}$$

where the temperature of the hot side is given by $T_h$ and of the cold side by $T_c$, and the Seebeck coefficient of the p- and n-type leg is defined by $S_p$ and $S_n$, respectively. In fact, when a current $I$ passes through the two legs occurs a Peltier cooling effect equal to $(S_p - S_n) I\, T_h$. The cooling is opposed by both the heat conduction from the hot junction at rate $\kappa(T_h - T_c)$ and the Joule heating within the thermoelectric materials $\frac{1}{2} R_{mat}\, I^2$. Thus, the efficiency $\eta$ corresponds to the ratio of the power of the external load $R_{ext}\, I^2$ and the heat flowing to the cold side of the device.

Considering $R_{ext} = R_{mat}$, the maximum efficiency at the mean temperature $T_m = \frac{1}{2}(T_h - T_c)$ is derived from equation 1.5 as [Row06]:

$$\eta = \frac{T_h - T_c}{T_h} \frac{\sqrt{1 + ZT_m} - 1}{\sqrt{1 + ZT_m} + \frac{T_c}{T_h}} \, . \tag{1.6}$$

In the limiting case $ZT_m \rightarrow \infty$, the total efficiency converges to the Carnot efficiency ($\eta_c = \frac{T_h - T_c}{T_h}$), which is the first term in equation 1.6.

Considering $ZT_m \sim 1$, the maximum efficiency of commercial thermoelectric bulk material at room temperature, at $T_h$ = 400 K and $T_c$ = 300 K, the efficiency is only 4.8%. It decreases to 1.1%, if the generator is working between $T_h$ = 320 K and $T_c$ = 300 K. To increase these efficiencies materials with higher $ZT$ are required.

To achieve high $ZT$ materials, the Seebeck coefficients should be high (to achieve large thermovoltages even for small temperature gradients), the electrical conductivity should be large (to minimize the Joule heating within the material), and the thermal conductivity should be low (to minimize heat losses and maintain the temperature gradients) [Soo09, Dav11]. However, in bulk materials, these quantities are interconnected. In figure 1.2 (a) the interplay of the contributions of $S$, $\sigma$, $\kappa_e$ and $\kappa_L$ to the total $ZT$ as a function of the charge carrier density ($n$) of the material is displayed. In general, materials with large $n$ are not suitable since $S$ is low and $\kappa_e$ has a high value. On the contrary, enhance $n$ results in a decrease of the thermopower with a decreasing of $\sigma$. The thermoelectric materials with highest $ZT$ are expected in the range of semimetals and semiconductors.

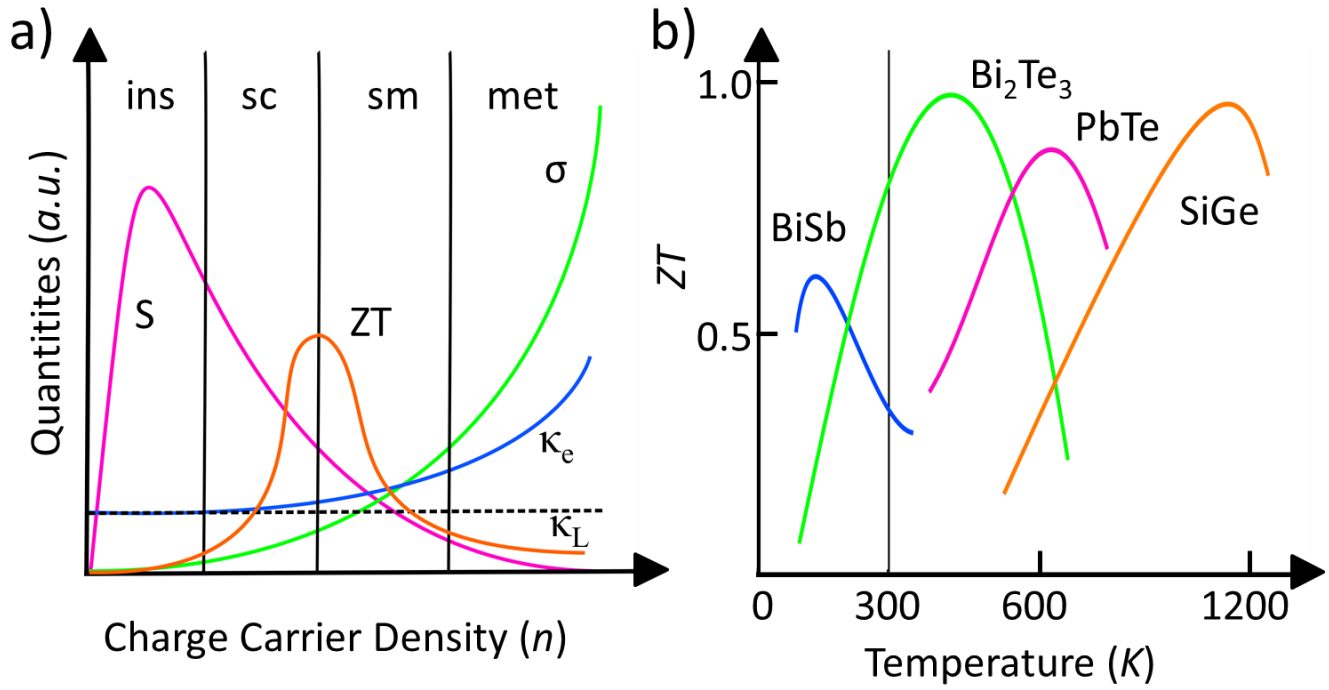


Figure 1.2: Schematic of (a) properties $S$, $\sigma$, $k_e$, $k_L$ and $ZT$ as a function of the charge carrier density [Row06] defining the different material phase: (*ins*) insulator, (*sc*) semiconductor, (*sm*) semimetal and (*met*) metal. (b) thermoelectric figure-of-merit $ZT$ of different semiconductor-semimetal materials as a function of temperature [Som07]. The vertical line shows the room temperature.

The correlation between $\sigma$ and $\kappa_e$ was experimentally observed by Wiedemann and Franz in different metals. Their ratio is given by [Wie53]:

$$\frac{\kappa_e}{\sigma} = \frac{1}{3}\left(\frac{\pi k_B}{e}\right)^2 T = L\,T\,, \tag{1.7}$$

where $L$ is the Lorenz number and equals to $2.44\ 10^{-8}\ W\Omega K^{-2}$.

Figure 1.2 (b) reports the $ZT$ of common semiconductor-semimetal alloys as a function of the temperature. At room temperature, $Bi_2Te_3$ has the largest figure-of-merit. In $Bi_{1-x}Sb_x$ alloys the maxima of $ZT$ appears at lower temperatures [Iss06]. Figure 1.2 (b) clearly shows that bulk thermoelectric materials do not achieve $ZT > 1$. The values are still too low to compete with traditional fossil fuels ($ZT > 2$) [Bel08], vapor compression-based ($ZT > 3$) [Cas08] energy production or freon based refrigeration systems ($ZT >$ 2-4) [Row06]. For this reason, thermoelectric devices are nowadays relegated to a range of niche applications, where the efficiency is not as important as the availability and reliability of the power production [Dre07].

Thermoelectric generators are used because of their high reliability providing little amount of electric power through small temperature gradient, for example, in remote earth locations [Bel08] or to

charge small electric devices like mobile phones and laptops [TES11]. Radioisotope thermoelectric generators are also present in space missions, exploiting for the production of electrical power the heat released during the isotope decay [Dav11]. Moreover, thermoelectric coolers/heaters are used on cars to control the temperature of the seats [Dav11] and on special suits to remove heat from the human body [Che12]. Recently, the utilization of thermoelectric generators combined with advanced photovoltaic cells has been proposed to increase the efficiency of the solar-to-electrical conversion [Fis14, Su14].

## 1.2 Low-dimensional Thermoelectric Materials

The Wiedemann-Franz law (eq. 1.7) and the dependency of the Seebeck coefficient on the charge carrier density cause an impasse in the pursuit of increasing the thermoelectric figure-of-merit in bulk materials [Els14]. After almost four decades of relatively slow progress in the thermoelectric research, a renewed interest began in the nineties due to predictions on how to enhance *ZT* [Ala13]. One of the new approaches aims to reduce the lattice thermal conductivity of bulk materials by increasing phonon scattering. Various methods are suggested including the introduction of mass fluctuation scattering centers by mixing crystals of different compounds [Liu12] or increasing interface scattering in multilayer systems [Wan12b]. Another approach to enhance *ZT* is to lower the dimensions of the material, i.e. confining the bulk structure (3D) in one direction to thin films (2D), in two directions to nanowires (1D), or in three directions to quantum dots (0D). Theoretical calculations by Hicks and Dresselhaus in 1993 predicted an increase of the thermoelectric figure-of-merit for quantum-well $Bi_2Te_3$ superlattice structures [Hic93b] and an even higher *ZT* for $Bi_2Te_3$ nanowires of very small diameters (~ 1-10 nm) [Hic93a, Sin03, Bej08]. In this case, the *ZT* increase is due to the changes in the material properties when the size of the low-dimensional structures becomes comparable to the Fermi wavelength of the charge carriers and to the charge carrier and phonon mean free path of the material [Far06].

In nanowire of diameter comparable to the electron Fermi wavelength, the charge carriers become confined in two dimensions and have discrete energy levels in agreement with quantum mechanics [Har05]. Thus, the density-of-states (*D(E)*) of the spatially confined material exhibits sub-bands located at certain energy (*E*) [Lin00b] instead of the continuous *D(E)* function in the bulk. A schematic of this transition is shown in figure 1.3, including also the other low-dimensional materials. Quantization effects of the charge carrier density and the subsequent formation of sharp peak maxima in *D(E)* are predicted to enhance the Seebeck coefficient of the material and the power factor ($S^2\sigma$) [Her05]. On the other hand, when the size of the structure is comparable to the phonon mean free path,

the contribution of the lattice thermal conductivity to the total thermal conductivity is significantly reduced due to the enhanced phonon boundary scattering at the nanowire surface [Li10, Hoc08]. A reduction of the bulk thermal conductivity by a factor about 100 was reported for rough-surface Si nanowires, and attributed to the increase of the phonon scattering [Bou06, Hoc08]. Moreover, current studies question that for nanostructures the Wiedemann-Franz law (eq. 1.7) remains valid [Kum93]. Experiments on Pt [Völ09b] and Ag [Koj15] nanowires indicated a Lorenz number lower than the bulk counterpart, which decreases with decreasing temperature.

Given by the theoretical predictions, considerable efforts focused on the synthesis and thermoelectric characterization of low-dimensional structures. However, only in few cases the measurements of the three thermoelectric properties, namely Seebeck coefficient, electrical and thermal conductivity, were carried out on the same sample which would provide a comprehensive result of the figure-of-merit. As an example, a high value of $ZT \sim 2.4$ at room temperature was presented for p-type $Bi_2Te_3/Sb_2Te_3$ [Ven01], $ZT > 1.5$ for PbSeTe quantum dot superlattices [Har02] and $ZT \sim 1.35$ for multilayered $Bi_2Te_3$ [Tan07], all values higher than $ZT$ of bulk.

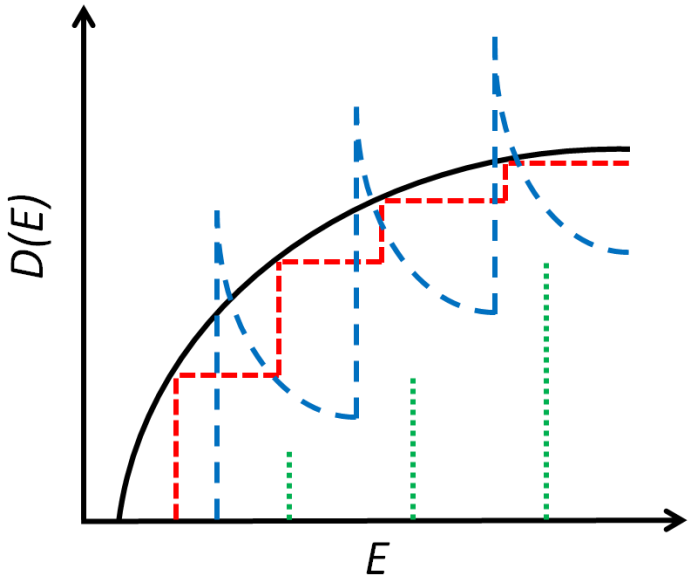


Figure 1.3: Schematic of the charge carrier density-of-states ($D(E)$) vs. energy ($E$) for bulk (black solid line), quantum well (red dashed line), quantum wire (blue dashed line) and quantum dot (green dots) [Dre03].

## 1.3 Properties of $Bi_{1-x}Sb_x$ Alloys

Bismuth (Bi), antimony (Sb) and bismuth-antimony ($Bi_{1-x}Sb_x$) bulk compounds crystallize in the rhombohedral structure belonging to the space group R3m. This is also called the $A_7$ structure, with the rhombohedral primitive cell containing two atoms per unit cell. The $A_7$ structure is slightly deformed with respect to the cubic structure. This small distortion induces that bismuth and antimony are semimetals characterized by a small overlap between the conduction and the valence bands [Len96]. Equivalently, the hexagonal notation can be used to describe the structure. The hexagonal unit cell of the material possesses six atoms per unit cell [Tan14b] and the lattice parameters almost follow Vegard´s law, varying monotonically from $a$ = 4.5465 Å and $c$ = 11.8616 Å for pure Bi to $a$ = 4.3085 Å and $c$ = 11.2732 Å for pure Sb at room temperature [Cuc62, Dis68]. Such similarity of the lattice parameters allows forming solid bismuth-antimony solutions over the whole composition range [Len96].

The electronic band structure of the bismuth-antimony solution varies significantly as a function of the stoichiometry [Tan14a], as reported in figure 1.4. To describe the structure three points of the Brillouin zone are of special interest, namely the T-, H- and L-point.

In pure Bi, the holes fill pockets at the T-point and the electrons at the L-point [Her05]. The indirect band overlap between the valence T-point and the conduction L-point band edge is estimated to be around 40 meV at 0 K [Len96]. Moreover, a direct band gap of 10 meV is present at the L-point. The dispersion relation is parabolic for the holes and non-parabolic at the L-point due to the strong coupling between the charge carriers, described by the Lax two-band model [Lax60].

Adding antimony decreases the band overlap and the direct band gap of the electronic structure. At $x$ = 0.04, the structure is gapless and beyond this composition the bonding and antibonding bands at the L-point is inverted. The band overlap vanishes at $x$ = 0.07, leading to a transition to an indirect gap semiconductor phase between the T- and L-point [Tan12]. At $x$ > 0.09, the alloy presents a direct gap semiconductor phase, since the T-point band possesses a lower energy than the L-point. Simultaneously, the valence band edge at the H-point raises and crosses the L-point conduction band edge at $x$ = 0.15-0.17, modifying the structure into an indirect gap semiconductor [Tan12]. At $x$ = 0.22 the valence band creates again an indirect band overlap and defines the semimetal phase [Len96].

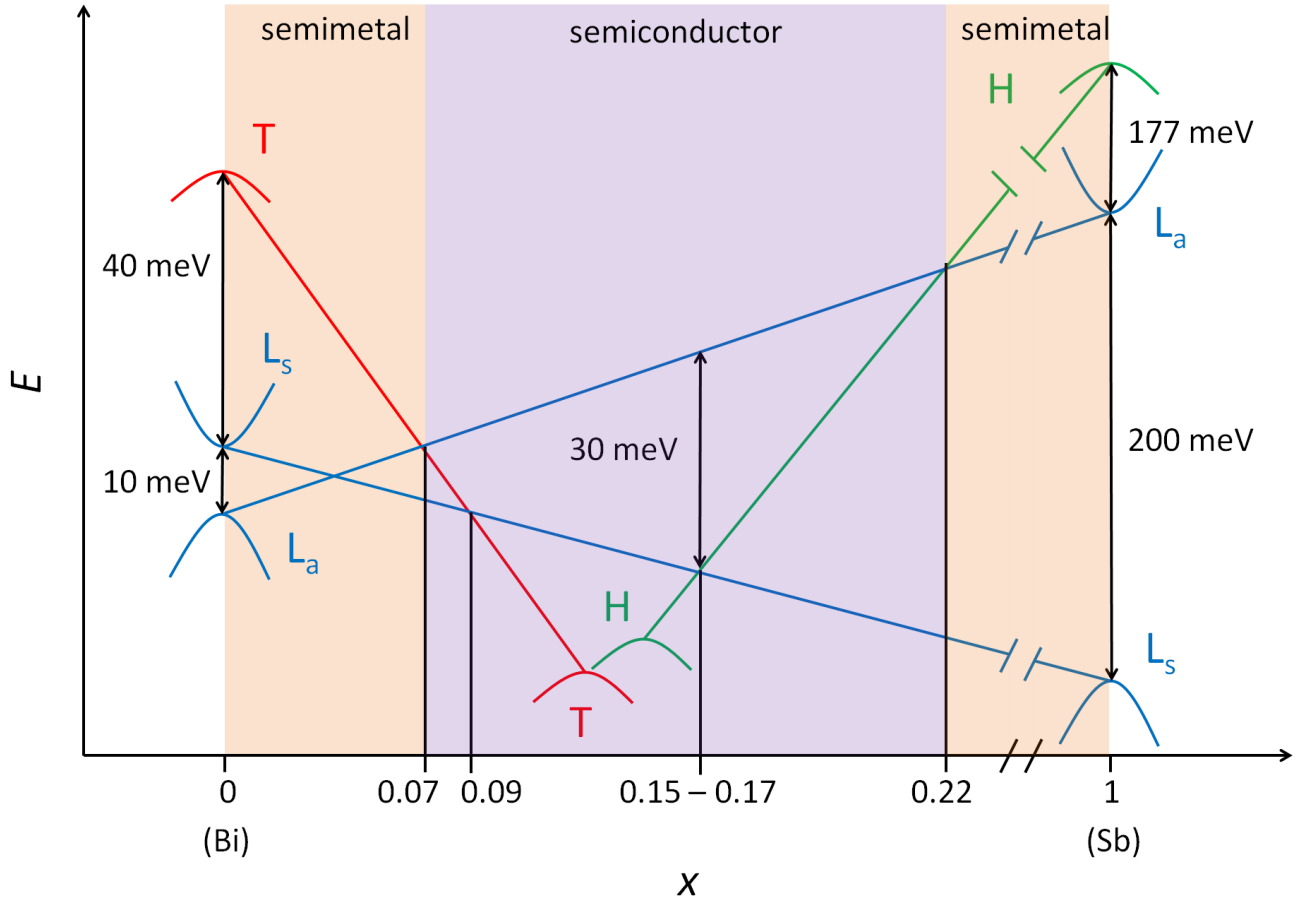


Figure 1.4: Schematic of band structure of $Bi_{1-x}Sb_x$ bulk alloy at 0 K as a function of the composition ($x$) according to ref. [Len96].

Bismuth bulk is known to possess better thermoelectric properties compared with $Bi_2Te_3$ at low-temperatures [Len96b]. Both bulk bismuth and antimony have a large anisotropic electronic Fermi surface. All thermoelectric transport properties depend thus strongly on the crystal direction [Iss79]. A general enhancement of the thermoelectric figure-of-merit was observed when adding Sb to Bi, yielding to a maximum of $ZT$ of ~ 0.4 at 70 K and ~ 0.5 for $x$ = 0.08 and 0.16, respectively [Iss06]. The maxima lie in the semiconductor phase of the alloy, as visible in figure 1.4. The small band overlap in pure bismuth leads to an equal number of electrons and holes in the electronic structure, which both contribute oppositely to the total Seebeck coefficient of the material [Her99]. Alloying with antimony and the creation of a bandgap create a transport structure with enhanced thermopower [Dre99].

Nanostructuring provides another benefit to further enhance the thermoelectric figure-of-merit of $Bi_{1-x}Sb_x$ the alloy [Tan14a]. Because bismuth possesses at room temperature an extremely large electron Fermi wavelength ($\lambda_e$ ~ 40-70 nm) [Cor10] and a very low effective mass ($m^*$ ~ 0.001-0.26 $m_e$), quantization effects are expected already in wires of relatively large diameter [Cor06b].

Moreover, as a consequence of the energy bands splitting into sub-bands, the energies of the conduction and valence band edges shift as a function of the structure dimension (figure 1.5). Thus,

lowering the dimension of the material leads to the formation of a gap in the electronic band structure [Lin02], causing the transition to semiconductor phase. Theoretical calculations for Bi wires predict this transition for wire diameters below 50 nm [Rab01]. Electrical measurements reported this change at such low wire diameter [Lin02].

Compared to bulk a reduction of the total thermal conductivity is expected in nanowires [Li10, Hoc08]. Bismuth nanowires of diameter ~ 200 nm showed already a 6 times suppressed total thermal conductivity with respect to bulk. This observation is ascribed to diffuse phonon-surface and phonon–grain boundary scattering [Moo09].

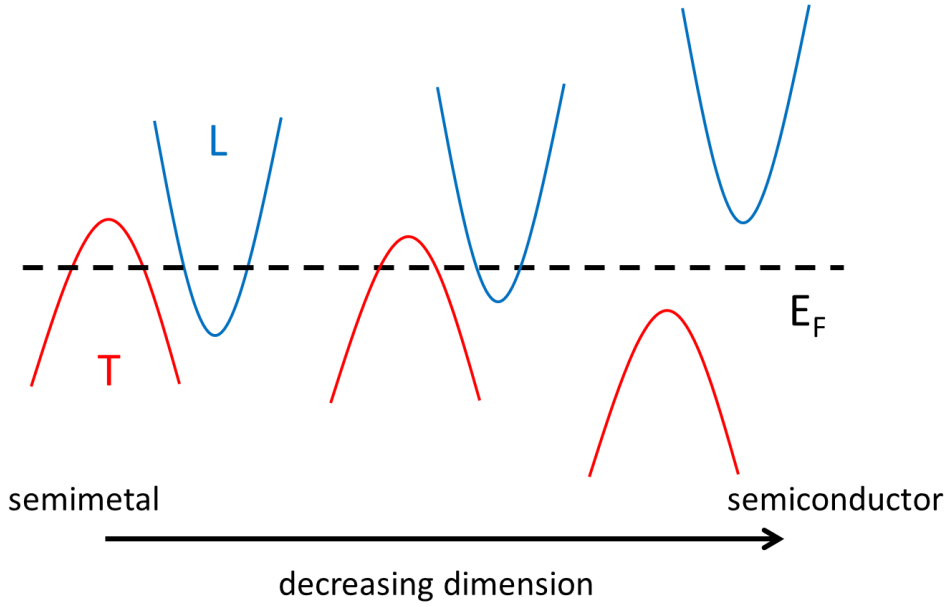


Figure 1.5: Schematic of the band gap of bismuth nanowires when decreasing the structure dimensions.

Therefore, it was expected that $Bi_{1-x}Sb_x$ nanowires could potentially have a higher thermoelectric efficiency compared to the bulk counterparts. Theoretical calculations based on semi-classical Boltzmann transport equations supported this idea pointing out an enhanced *ZT* by decreasing wire diameter and adjusting doping [Lin00, Tan14b]. In particular, in $Bi_{0.87}Sb_{0.13}$ a value of *ZT* around 1.5 was predicted for Bi nanowire with diameter ~ 15 nm, and around *ZT* ~ 2.5 for 40 nm nanowire diameter [Rab01].

Despite the promising theoretical predictions, comprehensive and systematic measurements on the thermoelectric properties of $Bi_{1-x}Sb_x$ alloy nanowires as a function of wire diameter and orientation are scarce [Tan14a]. The difficulties are both in the synthesis of $Bi_{1-x}Sb_x$ alloy nanowires with the desired geometrical, compositional, and structural characteristics and, subsequently, in contacting single nanowires to measure the Seebeck coefficient as well as electrical and thermal conductivity.

**This work** focuses on the synthesis of $Bi_{1-x}Sb_x$ ($0 \leq x \leq 1$) nanowires and the characterization of their thermoelectric properties. Measurements of the Seebeck coefficient and electrical resistance of $Bi_{1-x}Sb_x$ nanowire arrays were performed varying both wire diameter and composition. For the interpretation of the data, a systematic investigation of the crystallographic orientation and composition of the wire was performed.

The following chapter provides a detailed study of the influence of the deposition parameters on the composition and on the crystallographic orientation of the nanowires of different diameters. The production of the track-etched templates is described, including the irradiation with swift heavy-ion and chemical track etching. The subsequent electrochemical deposition of the $Bi_{1-x}Sb_x$ alloy into the pores by both pulsed and potentiostatic method is presented with a **systematical** change of the Bi:Sb ratio concentration in the electrolyte and of the diameter of the pores. The influence of these parameters on the composition and crystallographic orientation of the wire is investigated by X-ray diffraction as well as by scanning and transmission electron microscopy. These characterization results are essential for the comprehension of the successive thermoelectric measurements.

The third chapter reports measurements of the Seebeck coefficient and electrical resistance of $Bi_{1-x}Sb_x$ nanowire arrays. These experiments are performed in a setup specifically designed for nanowire arrays where excellent thermal contacts to the sample were developed. The measurements were carried out varying **systematically** composition ($0 \leq x \leq 1$) and diameter (from ~ 750 to ~ 40 nm) of the wires in a temperature range between 300 and 20 K. The influence of both wire diameter and composition on the Seebeck values was interpreted considering both quantum- and finite-size effects. However, also the influence of the surface states is considered, employing a two-band theoretical model that describes the interplay of both bulk and surface states on the total thermopower of the nanostructure.

Since the exposition to heat and air is a basic requirement for thermoelectric **applications**, in the last chapter, the effects of the annealing on the composition and morphology of individual $Bi_{1-x}Sb_x$ nanowires are investigated.

# 2. Synthesis and Characterization of $Bi_{1-x}Sb_x$ Nanowires

This chapter reports the synthesis of $Bi_{1-x}Sb_x$ alloy nanowires ($0 \leq x \leq 1$) by electrodeposition in the channels of polycarbonate etched ion-track membranes. The nanowire arrays were subsequently characterized by various techniques to study morphology, crystallography, and composition of the wires as a function of the deposition conditions.

First, we introduce the ion-track technology to produce the templates in which the nanowires are electrodeposited. The template fabrication process includes the irradiation of polymer foils with swift heavy ions of MeV-GeV kinetic energy and subsequent chemical etching in a suitable solution to dissolve selectively the ion tracks and form nanopores of tailored diameter. Finally, the nanowires were electrochemically deposited in the cylindrical pores by using both potentiostatic and pulsed voltage conditions.

The characterization of the nanowire arrays revealed the influence of the deposition conditions of the wire growth rate over the whole sample area and over the nanowire diameter as well as of elemental composition and crystallographic orientation. The first property is important to facilitate the subsequent contact of the arrays between two macroscopic metal layers, used as electrode, and thus measuring their thermoelectric properties, especially the Seebeck coefficient, whose evaluation is presented in the next chapter.

## 2.1 Experimental Details on Wire Synthesis and Characterization

The synthesis of $Bi_{1-x}Sb_x$ nanowires has been reported in literature using several different techniques, such as solvothermal methods [Tan09], laser vaporization [Rep07], whiskering of Bi films [Sta12], precipitation of Bi from molten Bi-Ga mixtures [Bhi05], Taylor process [Glo77], electron beam writing [Chi04] and synthesis in aqueous solutions via a free-template route [Zho07]. With respect to most of these methods, electrochemical deposition in templates is known to offer an excellent control on the thermoelectrically relevant nanowire parameters, including wire diameter, crystallographic orientation and crystallinity [Mar03, Lim15].

The growth of $Bi_{1-x}Sb_x$ nanowire arrays with uniform wire length was previously reported by electrochemical deposition into the channels of porous alumina templates [Pri01, Li04]. However, the use of polymer templates presents two main advantages: (i) polycarbonate membranes possess a lower thermal conductivity (~ 0.19 W/mK) than alumina (~ 10-30 W/mK) [Mob12], allowing the proper thermoelectric characterization of embedded nanowire arrays, (ii) polymer can be easily dissolved in suitable organic solvents, like dichloromethane, without affecting the nanowire surface, while alumina templates need to be dissolved by strong bases or acids that results in oxidized surface layers.

The synthesis of nanowires by electrochemical deposition in polycarbonate etched ion-track templates includes the fabrication of the template and the electrodeposition process. Both steps are explained in the sections below.

### 2.1.1. Production of Etched Ion-Track Membranes

Commercial polycarbonate (PC) foils (Makrofol N, Bayer AG, thickness 30 μm )[Mob12] were irradiated with high energy heavy ions at the UNILAC linear accelerator of GSI Helmholtz Centre for Heavy Ion Research (Darmstadt, Germany). On their way through the polymer foil, each heavy ion (e.g. Au, Pb or Bi) creates a cylindrical track consisting of damaged material [Ang96, Tra10]. Along their trajectories through the polymer, the ions loose energy due to the interaction with atoms (nuclear energy loss) and with electrons (electronic energy loss) [Yao06]. The electronic energy loss ($\frac{dE}{dx}_{el}$) can be described by the Bethe-Bloch Formula [Bet30, Blo33]:

$$-\frac{dE}{dx}_{el} = 4\pi \frac{Z_{eff}^2 n_e e^4}{m_e c^2 \beta^2}\left[\ln\left(\frac{2m_e c^2 \beta^2}{I(1-\beta^2)}\right) - \beta^2 - \delta - U\right] \quad , \tag{2.1}$$

where $dE$ is the energy loss per path length $dx$, $\beta$ the ions velocity relative to the speed of light $c$, $I$ the averaged ionization energy of the target atoms, $Z_{eff}$ the effective charge of the ion passing through matter, $n_e$ the electron density of the target material, $m_e$ the free electron mass, $e$ the elementary charge and δ and U correction terms. The effective charge depends on the ion velocity. At a given velocity, ions in matter lose and catch electrons until the equilibrium is achieved [Mei01].

The range of the ion in a given material ($I_{Range}$) is given by:

$$I_{Range} = \int_{E_0}^{0} \left(\frac{dE}{dx}\right)^{-1} dE \quad , \tag{2.2}$$

assuming that the ion is stopped when the total energy, the integral of the nuclear and electronic energy loss, is completely transferred to the target.

The irradiation of the polymer samples was performed with Au ions of ~ 2.2 GeV kinetic energies, corresponding to a specific energy of ~ 11.1 MeV per nucleon (MeV/u). The energy losses and the projected range of the Au ions in polycarbonate were calculated using the SRIM 2003 code [Zie04]. The results are displayed in figure 2.1 (a) and (b), respectively.

The penetration depth of gold ions accelerated to ~ 2.2 GeV is ~180 µm. After passing three 30 µm thick polycarbonate foils, normally irradiated as a foil stack, the ions still possess a total energy of ~1.1 GeV, as reported in figure 2.1 (b). The total energy loss over the thickness of the three foils is almost constant, as visible in figure 2.1 (a), leading to a homogenous modification of the physical and chemical properties of the target along the ion path, the so-called latent ion track [Pet95, Ape98].

Two models describe the formation of tracks in solids by swift heavy ions: the thermal spike model, which assumes a high temperature along the ions trajectory due to the deposited energy [Wan94], and the Coulomb explosion model, which predicts first pronounced ionization of atoms along the trajectory and a subsequent repulsion, leading to the formation of disorder [Fle65]. In polymers, the track core has a typical diameter of less than 10 nm whereas the track halo may reach up to 1 µm, depending on the deposited energy density, the radiation sensitivity and other parameters [Sun03, Deh03].

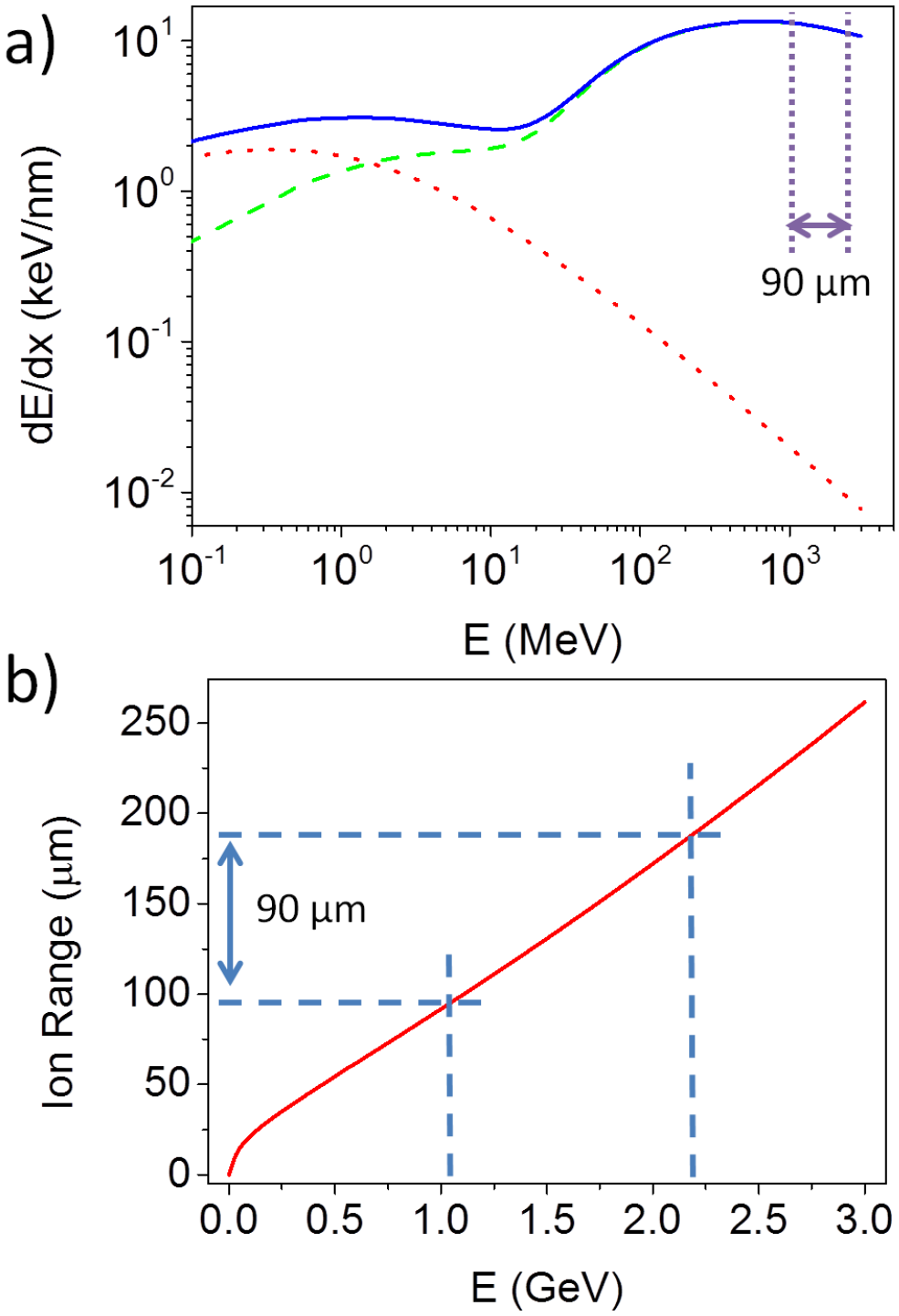


Figure 2.1: SRIM calculations for Au ions passing through polycarbonate membranes providing: (a) nuclear (dotted red line), electronic (dash green line) and total (solid blue line) energy loss of the ions and (b) the projected ion range as function of the ions total energy. Blue dotted vertical lines indicate the ion energy at the entrance of the first polymer of the stack and after passing the three foils (total thickness ~ 90 µm).

Subsequent to the ion irradiation, the tracks are selectively dissolved and converted into nanochannels by chemical etching [Fle75, Tra96]. The foils are introduced into a suitable etching agent, which for PC is a concentrated sodium hydroxide solution [Cor10]. During the etching process, the damaged zone of the latent tracks are preferentially removed and transformed into hollow channels. To form cylindrical nanochannels, the anisotropic track etch rate ($v_T$) has to be much larger than the isotropic bulk etch rate ($v_B$). As visible from figure 2.2, the bulk-to-track etching ratio determines the opening angle $\alpha$ of the pores by:

$$\sin \alpha \approx \frac{v_B}{v_T} \quad . \tag{2.3}$$

In practice a $v_T$ to $v_B$ ratio of the order of $10^3$ can be achieved in PC foil [Tra96].

In this work, the irradiated polycarbonate foils were etched in 6 mol/l NaOH at 50°C yielding an etching rate of ~ 22 nm/min. Selecting a certain etching time enables us to adjust the diameter of the channels, and of the subsequent deposited nanowires [Fis83, Cor10].

Prior to etching, the samples were exposed to UV light (T-30M Vilber Lourmat lamp, 30 W, 312 nm) for one hour on each side, to increase the track-etch velocity $v_T$ [Tra95] and to improve the homogeneity of the etching process. This treatment is known to result in a narrower pore diameter distribution [Pep07, DeS79].

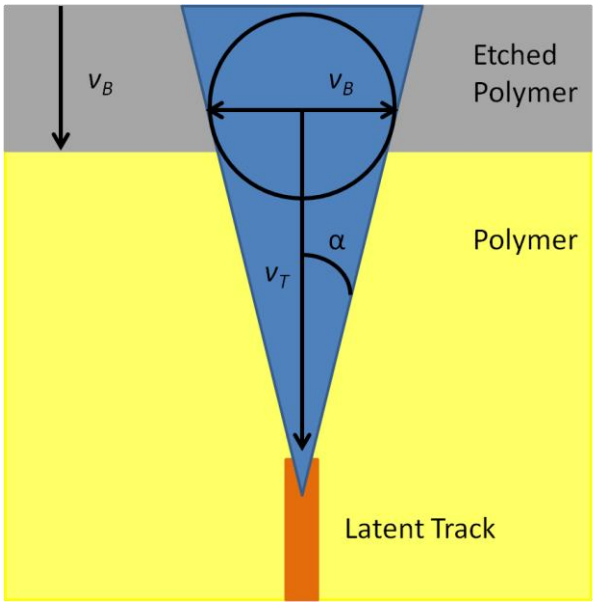


Figure 2.2: Schematic of the ion-track etching process with bulk and track velocities for etchant interaction with the polycarbonate membrane.

### 2.1.2 Electrochemical Deposition of $Bi_{1-x}Sb_x$ Nanowires

After etching, a thin conductive Au layer (thickness ~ 200 nm) was sputtered onto one side of the etched ion-track membranes, using an Edwards Sputter Coater S150B (pressure $10^{-1}$ Torr, voltage 1.5 kV, current 15 mA, 5 minutes). The template was subsequently placed between two teflon compartments as depicted in figure 2.3. The sputtered layer was reinforced by electrochemical deposition of an approximately 1 µm thick Au layer (applying 1 V for 10 min to Au sulfide (AuSF) solution by Metakem) using a two-electrodes setup, as reported in figure 2.3 (a). The conductive Au layer acts as working electrode, while the $Pt_{0.90}Ir_{0.10}$ spiral and a saturated calomel electrode (SCE) (Meinsberg) act as counter and reference electrode, respectively, in the three-electrodes setup, as displayed in figure 2.3 (b). The deposition setup was built by extending a former two-electrodes setup by the integration of a potentiostat and the SCE, in order to better control better the deposition potential in a reproducible way. The potentiostat monitors the voltage at the reference electrode and, by comparison with the desired deposition voltage, adjusts the voltage provided to the counter electrode. The setup allows keeping the potential at the reference electrode equals to the selected deposition potential [Mül12b]. Bismuth and antimony are deposited into the nanochannels at room temperature using an electrolyte consisting of 1.95 mol/L HCl acid (≥ 37%, Merck KGaA), 1.09 mol/L glycerol (≥ 99,5%, Merck KGaA), 0.2 mol/L NaCl (≥ 99,5%, LS Laborservice), 0.3 mol/L tartaric acid (≥ 99,5%, Merck KGaA), Bi(III)-chloride (≥ 98%, Merck KGaA) as well as Sb(III)-chloride (≥ 99%,Merck KGaA) in a total concentration of 0.1 mol/L. The material deposition takes place according to the reaction [Cor05]:

$$(1-x)Bi^{3+} + xSb^{3+} + 3e^{-} \Leftrightarrow Bi_{1-x}Sb_x\,. \tag{2.4}$$

The electrolyte is based on hydrochloric acid to allow the complete dissolution of Bi(III)- and Sb(III)-chloride [Ver03]. The electrolyte was introduced into one of the Teflon compartments, as indicated in figure 2.3, and left for thirty minutes before starting the deposition. This ensures sure that the electrolyte has penetrated into the pores of the membrane.

For the deposition, six solutions with six different concentrations of Sb ions (*c(Sb)*), namely 0, 0.01, 0.015, 0.02, 0.03, and 0.1 mol/L were employed. The concentration of Bi ions (*c(Bi)*) was adjusted in each case to achieve a total concentration of 0.1 mol/L of Bi and Sb ions in the electrolyte.

The different stages of the nanowires deposition was followed by recording the current as a function of the deposition time. Figure 2.4 displays the four characteristic deposition phases occurring during nanowire growth [Toi01]: (1) a sharp current increase followed by a decrease attributed to the charging of the electrical double layer and to the formation of the diffusion layer. (2) a nearly constant current,

occurring during the deposition of material in the channels. (3) an increase of the current as soon as the cylindrical pores are completed filled and the deposition is no longer constricted by the pore geometry. If the process continues, material grows on top of the nanowires forming so-called caps. (4) For extended deposition times, the caps coalesce and form a continuous layer. When this is the case, the deposition current reaches another plateau.

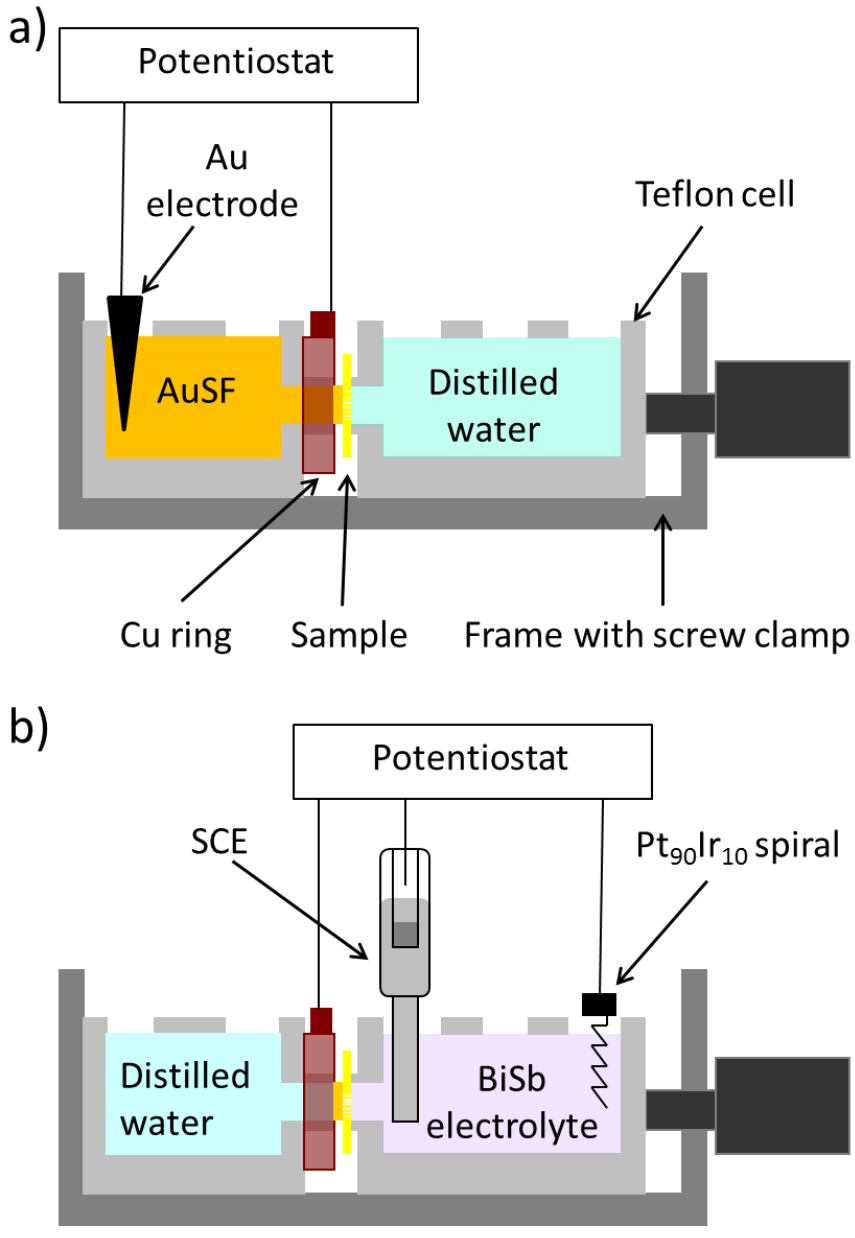


Figure 2.3: Schematic of experimental setup for the electrodeposition of (a) Au substrate on the sputtered Au layer of the template and (b) nanowires in track-etched nanochannels of polycarbonate membrane.

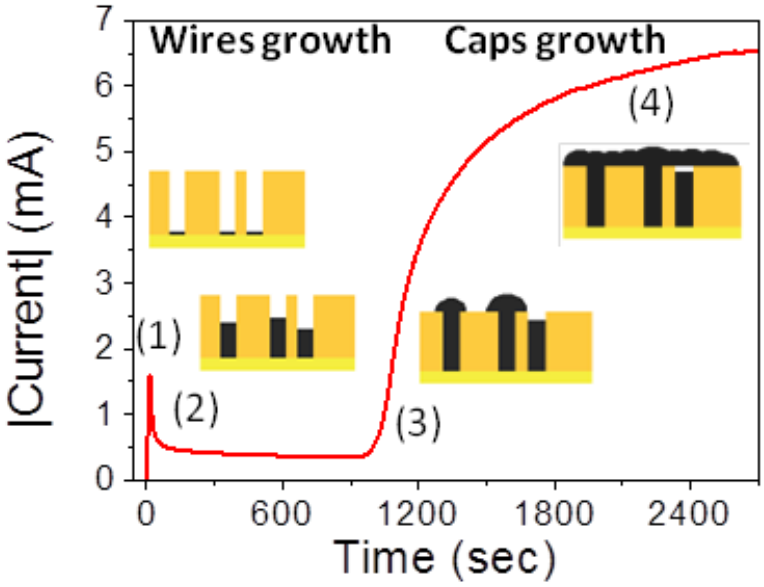


Figure 2.4: Representative chronoamperometric curve (*I-t*) for electrodeposition of nanowires in etched ion-track membrane illustrating the four different stages of the deposition process (1)-(4).

## 2.2. Characterization Techniques

The thermoelectric properties of $Bi_{1-x}Sb_x$ nanowires are known to be strongly dependent on both nanowires composition and crystallographic orientation [Len96, Tan15]. Therefore, a detailed investigation of composition, orientation, surface structure and crystalline size of the nanowires is required to understand the properties of the material and the subsequent thermoelectric measurements performed on both individual and array of nanowires [Lin00, Dre99].

The crystallographic orientation and composition of the $Bi_{1-x}Sb_x$ nanowire arrays embedded in the polycarbonate template was investigated by X-ray diffraction (XRD). Moreover, the morphology and geometry of single nanowires were investigated by high resolution scanning electron microscopy (SEM). The composition was analyzed by energy dispersive X-ray analysis (EDX) and the crystalline size and orientation of the grains inside the nanostructure were studied by transmission electron microscopy (TEM).

### 2.2.1 Scanning and Transmission Electron Microscopy

The surface morphology of the nanowire arrays was analyzed using a JEOL JSM-7401F high-resolution scanning electron microscope. SEM images are produced by the signals generated from the interaction of the finely focused electron beam with the sample surface. Figure 2.5 displays the schematic of the excitation bulb formed by the incident electron beam interacting with the sample at various depths [Rei85, Sal11]. Near the sample surface, this process leads to the emission of both Auger (maximum depth ~ 5 nm) and secondary electrons (SE) (depth 5-50 nm) [Eve60]. Backscattering electrons (BSE) are emitted from a deeper region of the sample (up to ~ 200 nm) [Oat72] and the emission of both Bremsstrahlung and fluorescence radiations occur in thick sample up to ~ 450 and ~ 550 nm, respectively [Rei98]. Moreover, if the electron beam has a sufficient high energy, characteristic X-rays are formed during the interaction in a depth up to ~ 350 nm, providing quantitative information about the composition of the sample [Gol07].

In this work, mainly the SE detector was used to analyze the samples. Since this type of electrons have a low energy (< 50 eV), only electrons from the surface of the samples reach the detector, providing information about the morphology and surface of the nanowires.

Moreover, single nanowires on the TEM grids were analyzed by the integrated scanning electron transmission in SEM (STEM-in-SEM) detector. The imaging of this method is based on the detection of electrons transmitted through the samples.

The samples for SEM and TEM analysis were prepared as follow. The electrodeposition of $Bi_{1-x}Sb_x$ nanowires was stopped after the growth of the caps (region 4 of figure 2.4). To observe the caps on the surface of the membrane, a piece of the sample was placed directly on a SEM sample-holder and analyzed. To study the shape and composition of single nanowires, a piece of the metal-filled membrane was put on the base of a small funnel and drops of dichloromethane were used to dissolve the polymer and release the wires. At the end of the funnel, Cu TEM grids with a lacey carbon film or a small piece of silicon substrate collected the nanowires. After complete evaporation of the dichloromethane, the samples were directly transferred into the microscope.

At the Institute of Applied Physics (Tübingen, Germany), single nanowires on Cu-lacey TEM grids were analyzed by bright-field (BF) and dark-field (DF) imaging in a Zeiss 912 Ω transmission electron microscope operated with an electron beam energy of 120 keV. In BF imaging the pictures are formed from the unscattered electrons passed through the sample. Contrast in these images is due to differences of the thickness or density of the sample. On the other hand, DF imaging uses the scattered electrons to form the images. This makes the areas of the sample with different crystal orientation or structure respect the sample zone producing the diffracted beam, appearing darker [Wil96].

The samples for TEM investigations were prepared by transferring single nanowires onto Cu-lacey TEM grids as for the SEM measurements previously reported. To obtain suitable signal from the transmitted electrons, the sample thickness must be smaller than ~ 100 nm. For this reason the nanowires analyzed in this work by TEM possess a diameter of ~ 80 nm.

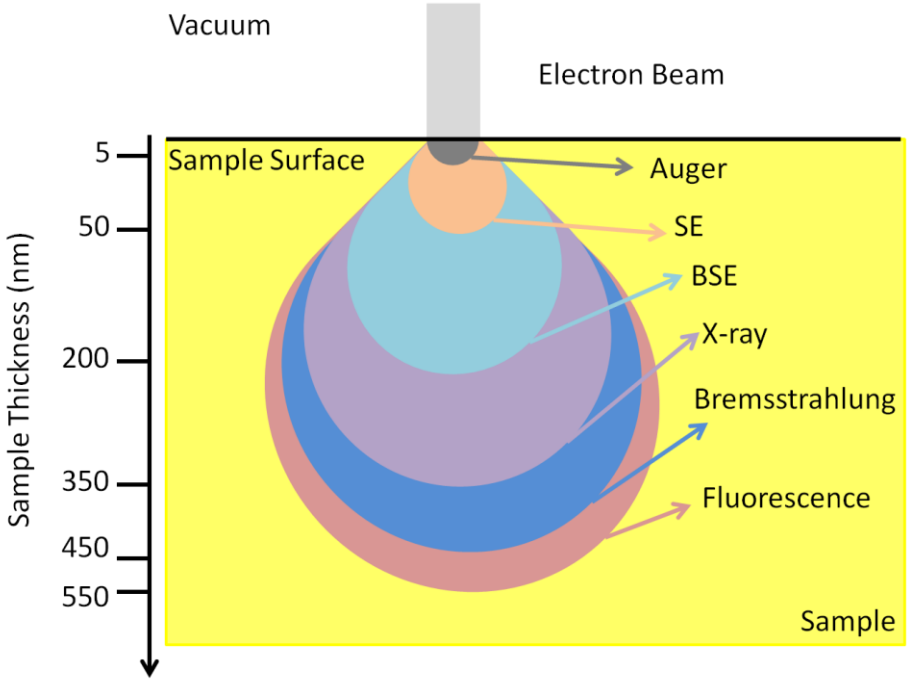


Figure 2.5: Schematic of the excitation bulb of the incident electron beam in the sample at different sample depth. The interaction with the sample leads to Auger electrons, secondary (SE) and backscattered (BSE) electrons, as well as characteristics X-ray, bremsstrahlung and fluorescence emission [Rei85, Sal11].

### 2.2.2 Energy Dispersive X-ray Analysis

Energy dispersive X-ray analysis (EDX) was employed to determine the nanowires composition. The characteristic emitted X-ray is specific of the elements can be used to identify the chemical composition of the samples. The measurements were performed on single nanowires placed onto Cu-lacey TEM grids. The selected wires were positioned across a hole in the middle of the carbon film. The usage of the TEM grids as substrate for the analysis enables not only the electrons transmission through the specimen and their detection both into TEM and SEM, by the STEM-in-SEM detector, but also the minimization of the background effects on the detected signals.

For quantitative EDX analysis of the nanowires a Bruker XFlash 5030 system in the SEM was used. The electron beam energy was selected to 10 keV. This allows performing quantitative analysis by

using the Sb-L (excitation energy $E_C$ 4.132 keV) and Bi-M ($E_C$ 2.580 keV) shell transition line series [Bea67]. Information about the nanowire composition was obtained also by TEM-EDX in a JEM ARM 200CF operated at 400 keV at the Max Planck Institute for Intelligent Systems (Stuttgart, Germany). The results are presented in chapter 4.

### 2.2.3 X-ray Diffraction

The preferred crystallographic orientation of the grains inside the nanowires and the composition of $Bi_{1-x}Sb_x$ nanowire arrays embedded in the PC template were investigated by X-ray diffraction (XRD). The X-ray diffractograms were recorded using the Cu-$K_{\alpha1}$ ($\lambda$ = 0.15405 nm) and Cu-$K_{\alpha2}$ ($\lambda$ = 0.15444 nm) [Höl97] radiation of a Seifert X-ray generator and a HZG-4 goniometer in a Bragg-Brentano geometry with a step size of 0.02° and acquisition time of 2 sec/step. The Cu-$K_{\alpha2}$ radiations were filtered out with a monochromator placed after the X-ray generator. Prior to diffraction analysis, the Au cathode was removed from the PC membrane by $KI/I_2$ solution to avoid reflections from the gold substrate. Figure 2.6 shows the schematic of the geometrical arrangement used in this experiment.

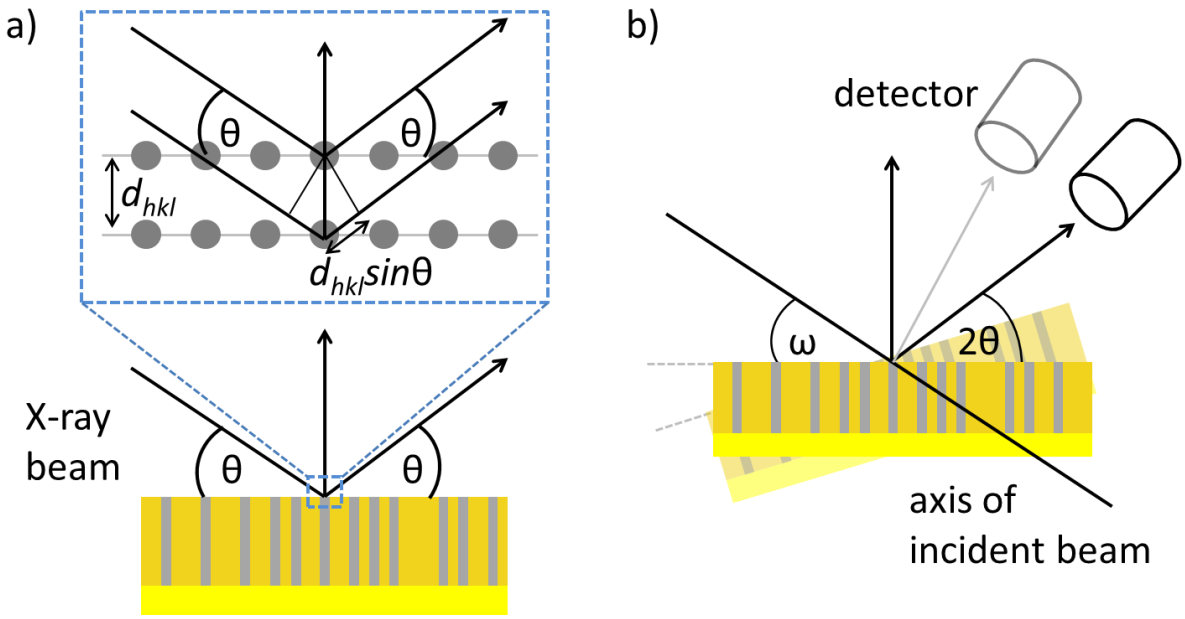


Figure 2.6: Scheme of reflection geometry of (a) lattice planes inside the sample and (b) XRD setup with Bragg-Brentano geometry.

The incident X-rays are diffracted by the sample lattice planes defined by the Miller indices *hkl*, according to Bragg´s law:

$$n\lambda = 2d_{hkl}\sin\theta\,, \tag{2.5}$$

where *n* is the order of diffraction, $d_{hkl}$ the spacing between the lattice planes and $\theta$ the diffraction angle. $Bi_{1-x}Sb_x$ alloys belong to the same space group R3m and the symmetry rules of this group allow values of *hkl* that fulfill $-h + k + l = 3n$, with *n* being a positive integer [Hah05].

Comparing the relative peak intensities (*I*) of a $2\theta$ scan diffractogram with standard powder diffraction patterns ($I_0$), reported for Bi and Sb [SPP], it is possible to calculate the texture coefficient (*TC*) of a nanowire array and to evidence the preferred orientation of grains inside the nanowires. *TC* is defined as [Har52]:

$$TC\left[(hkl)_j\right] = n \cdot \frac{I\left[(hkl)_j\right] / I_0\left[(hkl)_j\right]}{\sum_{i=1}^{n} I\left[(hkl)_j\right] / I_0\left[(hkl)_j\right]}\,, \tag{2.6}$$

with *n* being the number of considered reflections with Miller indexes $(hkl)_j$.

A texture coefficient of $TC[(hkl)_j]$ larger than one indicates a preferential orientation of the crystals in the nanowire with the planes *(hkl)* perpendicular to the wire axis. On the contrary, if the $TC[(hkl)_j]$ has a value ~ 1 for all the considered planes, the structure does not present any preferential orientation. The position and shape of the peaks are also influenced by other effects, including defects like grain boundaries, stacking faults, and chemical heterogeneities [Ung01]. In the case of $Bi_{1-x}Sb_x$, Dismukes et al. reported a monotonic decrease of the lattice parameters *a* and *c* with increasing Sb content in $Bi_{1-x}Sb_x$ alloys, with slight deviations from the values predicted by the Vegard´s law [Dis68]. For a given set of planes, the reflection angle $2\theta$ shifts to lower values for higher concentration of Sb. Thus, the position of the reflections peaks in the XRD diffractograms supplies information about the *x(Sb)* content in the wires.

## 2.3 Synthesis and Characterization Results

In this section we present the results from the synthesis and characterization of $Bi_{1-x}Sb_x$ nanowires grown both by potentiostatic and pulsed deposition.

We first studied the influence of the deposition conditions on the homogeneity of the wires growth over the whole sample area (subsection 2.3.1). The higher homogeneity ensures a similar wire growth process inside all the nanopores, reducing structural properties differences between wires of the same array.

The second part presents the results on the investigations of the crystallographic orientation and composition of the wires varying the Bi:Sb ratio concentration in the electrolyte (subsection 2.3.2). Similar systematic investigations then focused on how the crystalline orientation is influenced by the pore diameter for given compositions of the electrolyte (subsection 2.3.3).

These characterizations of the nanowire structure are essential to interpret the thermoelectric measurements as a function of both wires composition and diameter (chapter 3).

### 2.3.1 Potentiostatic and Pulsed Deposition

In this subsection we apply two different deposition methods (potentiostatic and pulsed deposition) to study the homogeneity of the wire growth over the whole sample. For this, we fabricated a series of etched ion-track membranes with identical parameters (thickness 30 µm, pore diameter 79 ± 8 nm, and pore density ~ $7\times10^8$ $cm^{-2}$) and used them as templates for the growth of $Bi_{1-x}Sb_x$ nanowire arrays with various electrolytes.

Figure 2.7 reports the chronoamperometric current vs. time (*I-t*) curves recorded during the nanowire potentiostatic (a) and pulsed (c) deposition using five different electrolytes with Sb concentrations between 0 and 0.1 mol/L. For the potentiostatic deposition, the potential $U$ = -220 mV vs. SCE was kept constant during the whole process. On the contrary, for pulsed deposition, the potential was varied between $U_1$ = -220 mV vs. SCE ($t_1$ = 20 ms) and $U_2$ = -150mV vs. SCE ($t_2$ = 100 ms), as reported in figure 2.7 (b). As visible in figure 2.7 (b), the deposition current drops fast to zero during $t_2$ because no deposition takes place, allowing the replenishment of electrolyte ions close to the cathode before the next reduction pulse is applied.

To compare the wires growth, all depositions were stopped when the current just started to increase, i.e. when the deposited material had reached the top of the membrane. The absence of caps on top of the metal-filled membrane is important for the subsequent XRD analysis.

Figure 2.7 (a) shows the absolute values of the chronoamperometric current vs. time (*I-t*) curves recorded during potentiostatic deposition using five electrolytes with different Sb concentrations, namely 0 (black line), 0.01 (red), 0.02 (green), 0.03 (blue) and 0.1 (magenta) mol/L. The data show that the deposition current is lower when the concentration of Sb ions in the electrolyte is higher. Assuming that the deposition area is the same (the membranes were prepared under identical conditions), a lower recorded current implies also a lower current density. On the other hand, the deposition time increases then enhancing the Sb concentration, starting from ~ 20 sec for pure Bi to ~ 390 sec for pure Sb wires.

Figure 2.7 (c) presents the deposition current (averaged every 10 consecutive pulses) vs. time for nanowires deposited with pulsed potential using identical membranes and same electrolytes as for the potentiostatic growth. The average *I-t* curves display the same qualitative behavior as for the potentiostatic growth (figure 2.7 (a)), namely a higher Sb concentration results in a lower deposition current and an increase of the deposition time.

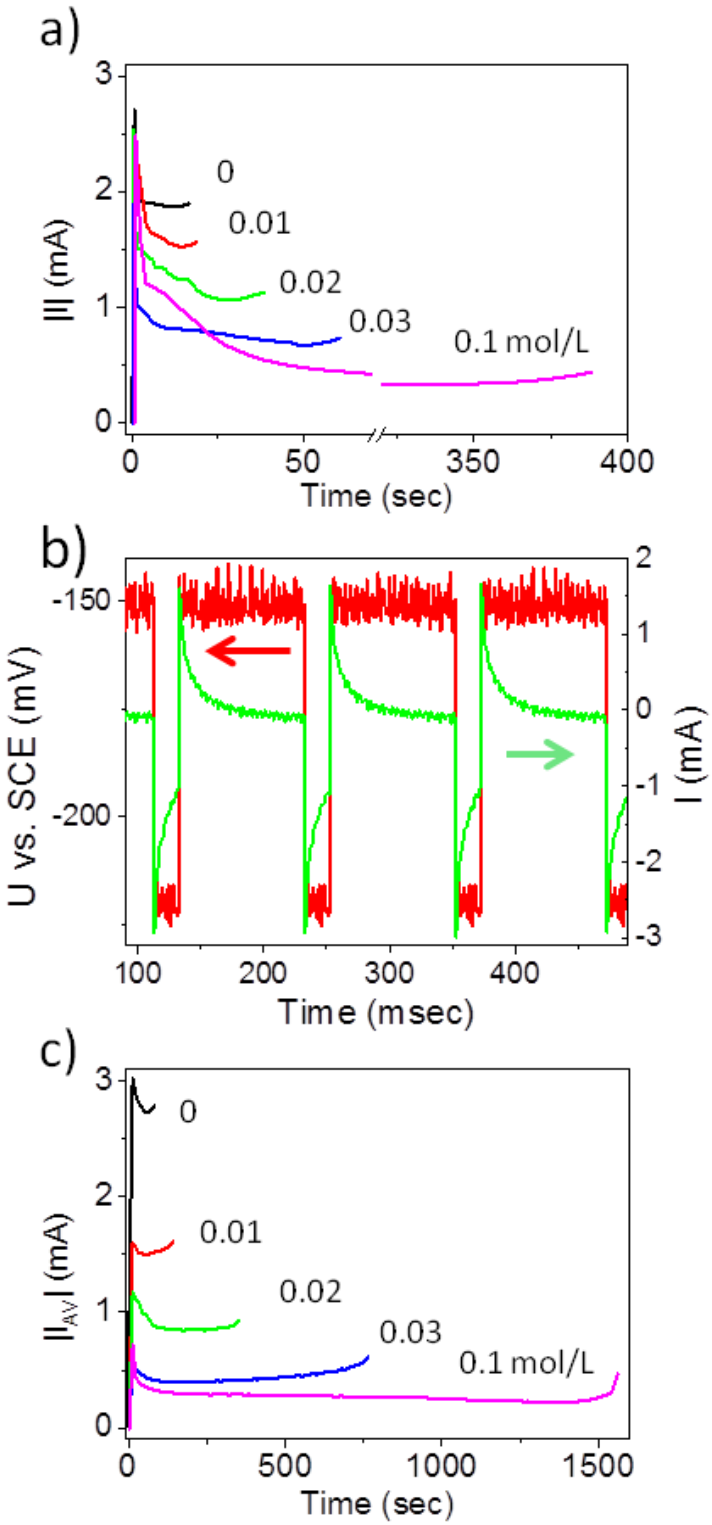


Figure 2.7: (a) Chronoamperometric curves (*I-t*) recorded by applying a potentiostatic voltage at *U* = -220 mV vs. SCE with electrolytes containing different Sb concentrations *c(Sb)* 0 (black), 0.01 (red), 0.02 (green), 0.03 (blue), and 0.1 mol/L (magenta). (b) Selected applied voltage pulses *U-t* (red) and the corresponding recorded current *I-t* (green) recorded during pulsed deposition. (c) Averaged current ($I_{AV}$) vs. time of the pulsed depositions of $Bi_{1-x}Sb_x$ nanowire arrays in nanopores membrane using electrolytes with various Sb concentrations given in mol/L.

To understand which deposition method yields more homogenous growth, the experimental charge ($Q_{exp}$), associated to the material deposited in the membrane channels, was estimated by integrating *I-t* curves in zones 1 and 2 (see Fig. 2.4) until the time at which cap growth starts [Ham07]. For potentiostatic and pulsed deposition $Q_{exp}$ as a function of *c(Sb)* is presented in figure 2.8. The experimental charge for pulsed deposition is larger than for potentiostatic deposition for all Sb concentrations. The larger deposited charge indicates that more channels were filled under pulsed potential conditions. This result suggests that the ion concentration close to the nanoelectrodes (the conductive layer at the bottom of each pore) is effectively increased during the second pulse $t_2$, yielding a more homogeneous growth rate among all the nanopores in the membrane. In the case of potentiostatic deposition, small variations of the growth rate among the wires in different channels get more pronounced as the deposition proceeds leading to a less homogeneous filling of the pores.

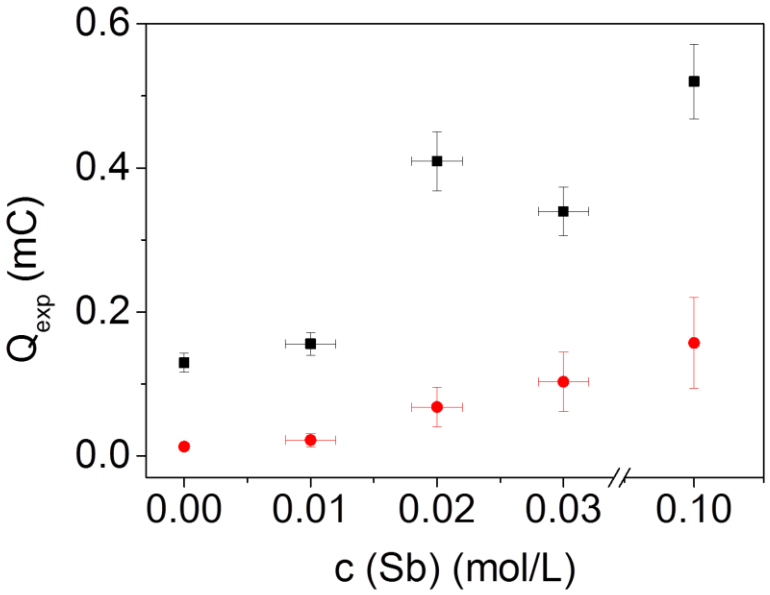


Figure 2.8: Experimental charge ($Q_{exp}$) measured after the growth of $Bi_{1-x}Sb_x$ nanowire arrays of samples reported in figure 2.7 by (a) potentiostatic (red points) and (c) pulsed deposition (black points) as a function of different concentration of antimony ions (*c(Sb)*) in the electrolyte.

The higher wire-growth homogeneity for pulsed deposition is also supported by SEM investigations. Figure 2.9 shows the top view of a membrane surface after the growth of Bi nanowire arrays by (a) potentiostatic and (b) pulsed deposition, respectively. Comparing the SEM images, it is clearly noticed that the number of wires reaching the top at the same time is significantly higher in the case of pulsed deposition due to the higher density of caps on the top surface, in agreement with the

higher measured experimental deposited charge ($Q_{exp}$) of figure 2.8. The figure insets show in both cases single caps surrounded by pores (marked with red circles for clarity). During the deposition process, some wires reach the template surface earlier than others and then quickly develop caps. The early arrival of some of the wires is attributed to the micrometer-scale film roughness in the membrane channel, causing fluctuations of the channel lenghts. A study by Wagner et al. revealed that only ~ 60% of Sb wires (deposited under similar pulsed deposition) reached the top surface at the same time [Wag15]. When, removing ~ 1 µm polycarbonate membrane for the top surface by reactive ion etching technique, the filling percentage enhanced to over 95%. This increase is supposed to be due to the roughness of the polymer foil. In our cases, the pronounced difference in $Q_{exp}$ (Fig. 2.8) indicates that it is also possible that the deposition does not take place in some channels due to, e.g., insufficient contact to the cathode or due to the presence of small air bubbles in the pores.

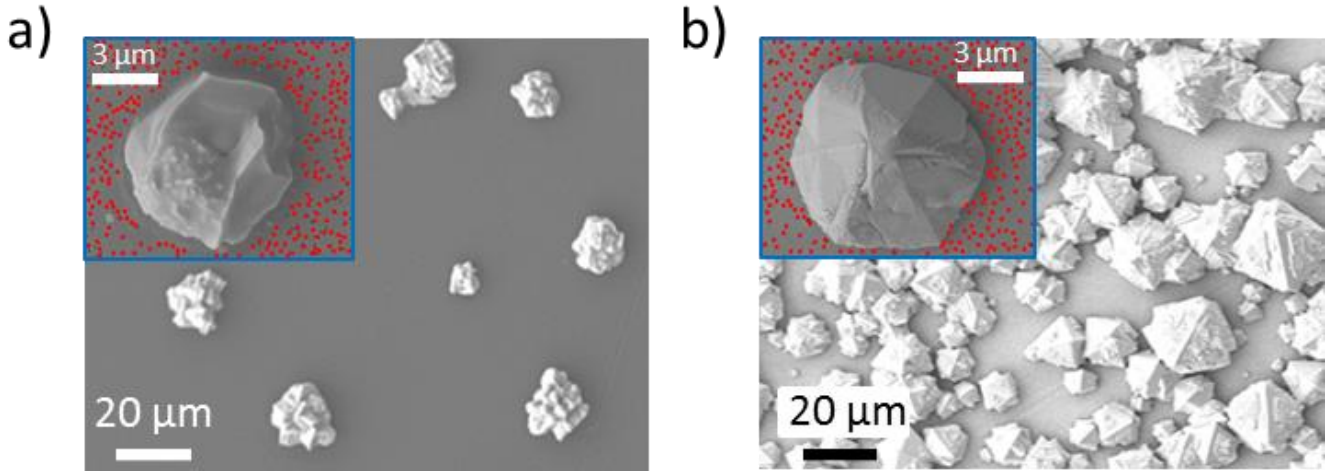


Figure 2.9: SEM images of the polymer surface displaying caps grown on top of Bi nanowires by (a) potentiostatic and (b) pulsed conditions. Both insets show an individual cap surrounded by empty pores marked in red circles.

In addition, the morphology of the caps of the two samples is different. In figure 2.9 (b) the caps exhibit large facets and long edges, indicating larger grains and twins in the nanowires structure. Whereas the caps in figure 2.9 (a) display a more irregular morphology and seem to consist of smaller grains. Previous works on bismuth nanowires [Cor05, Toi04] reported that the cap morphology is an indication of wire crystallinity. Faceted caps were found on top of single-crystalline wires or on wires consisting of few large crystals, whereas irregular and round caps were grown on top of poly-crystalline wires.

From the calculation of experimental charge and the number and shape of the caps, we can conclude that higher homogenous growth of $Bi_{1-x}Sb_x$ nanowire arrays can be obtained by pulsed deposition.

However, increasing the Sb ions concentration in the electrolyte leads to a larger experimental charge, as notable in figure 2.8, and at the same time to a lower deposition current and longer deposition time (figure 2.7) for both growth conditions. This behavior can be explained by cyclic voltammetry (CV) measurements performed with the same electrolytes used for the wires deposition. CVs on planar Au electrodes were performed using a Gamry potentiostat at a scan rate of 50 mV/sec for 5 cycles. Figure 2.10 reveals a shift in the main reduction peak from -312 mV vs. SCE for *c(Sb)* = 0 mol/L (magenta dashed line) to -396 mV vs. SCE for c(Sb) = 0.1 mol/L (black dashed line). This shift towards a more negative potential for a higher Sb concentration in the electrolyte is associated with the corresponding current decrease obtained in the deposition applying a deposition voltage of -220 mV vs. SCE.

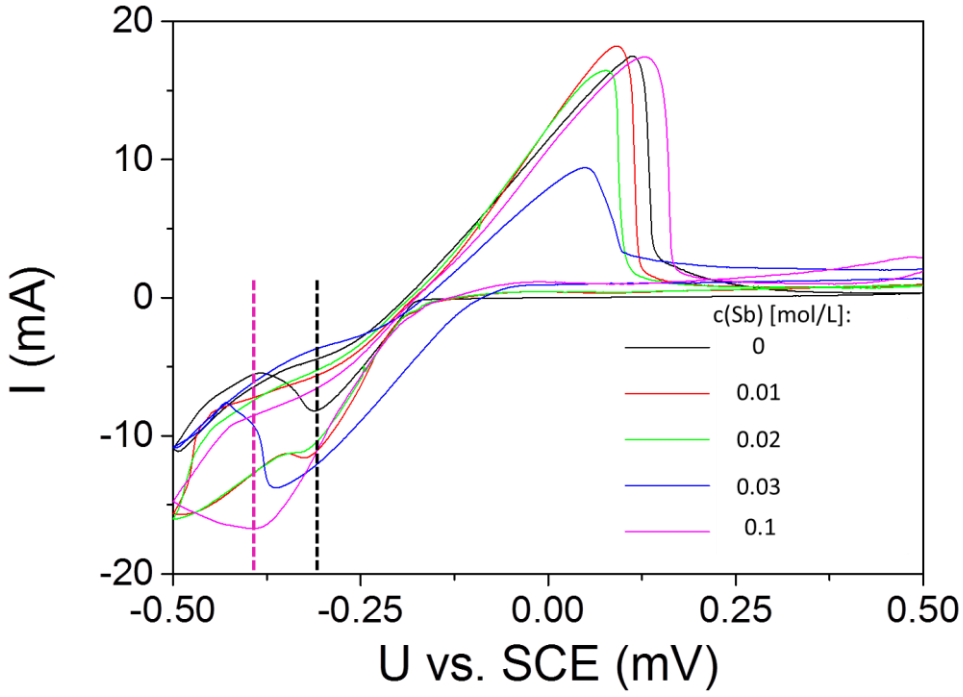


Figure 2.10: Cyclic voltammograms recorded on planar Au electrodes for different Sb ion concentrations of the electrolyte. The scan rate was fixed at 50 mV/sec. The reduction potentials of Bi and Sb are marked in black and magenta vertical line, respectively.

### 2.3.2 Crystallographic Orientation and Composition

Figure 2.11 (a) presents X-ray diffractograms measured on $Bi_{1-x}Sb_x$ nanowire arrays synthesized and studied in the previous section using pulsed deposition and electrolytes of different *c(Sb)*. To avoid the presence of caps on the top surface of the membrane, which influences the subsequent X-ray diffraction analysis, the sample deposition was stopped as soon as the current started increasing (see figure 2.7 (c)). In figure 2.11 (a), the employed Sb concentration in the electrolyte increases from the bottom (*c(Sb)* = 0, black) to the top curve (*c(Sb)* = 0.1 mol/L, magenta). The vertical bars represent the position and relative intensity of the reflections of standard Bi (black) and Au (orange) [SPP]. The intensities of all diffractograms were normalized to the corresponding (012) reflection.

The diffraction pattern of pure Bi wires exhibits two main reflections at $2\theta$ = 27.16° and 39.60°, corresponding to the (012) and (110) planes oriented perpendicular to the wire axis [SPP]. This is also the case for $Bi_{1-x}Sb_x$ nanowire arrays deposited with *c(Sb)* = 0.01 (red) and 0.02 mol/L (green). Nanowire arrays deposited with higher Sb concentrations, namely *c(Sb)* = 0.03 and 0.1 mol/L, exhibit both a preferred (012) orientation. In few cases, weak reflections appear at 2θ = 48.69° and 56.02°, corresponding to the (202) and (024) orientation, respectively, and the presence of the Au is still visible at $2\theta$ = 38.29° and 44.49°, corresponding to the orientation (111) and (200) [SPP], despite having dissolved most of the Au substrate with a $KI/I_2$ solution. The Au dissolution was performed because the Bi (104) peak partially overlaps with the Au (111) reflection. However, no (104) reflections were detected in any of the samples for which the Au substrate had been removed totally.

Comparing these XRD diffractograms with previously reported data on $Bi_{1-x}Sb_x$ nanowire arrays grown potentiostatically with the same electrolytes and deposition voltage *U* [Mül12], we notice that arrays of wires deposited with *c(Sb)* = 0.01, 0.02 and 0.03 mol/L and similar nanowire diameter, exhibited also preferred (110) and (012) reflection peaks. This indicates that both pulsed and potentiostatic deposition yield to the same preferred crystallographic orientation.

Superior thermoelectric properties were predicted in nanowires with diameters below ~ 20 nm due to quantum- and finite-size effects [Hic93a, Tan14]. To check possible differences in the crystallographic orientation, series of 30 µm thick polycarbonate membranes with pore density ~ $7\times10^8$ $cm^{-2}$ were prepared with pore diameter of 18 ± 3 nm. The nanowires were deposited at room temperature applying a slightly more negative deposition potential $U_1$ = -250 mV vs. SCE for $t_1$ = 20 ms and $U_2$ = -150 mV vs. SCE for $t_2$ = 100 ms, using different concentration of Sb ions. The corresponding XRD diffractograms are presented in figure 2.11 (b). The diffractogram of pure Bi nanowires (black) displays two reflections, namely (012) and (110), as present also in thicker nanowires. However, when using Sb concentration 0.02 mol/L (green) or higher, all diffractograms

exhibit a clear preferred (012) orientation and very small reflections for the (202) and (024) orientations, which are not present for *c(Sb)* 0.1 mol/L. It is noticeable that the pattern recorded for the array deposited with a Sb concentration of 0.015 mol/L (brown) exhibits, unlike any other in this series, a distinct (110) preferred orientation. To further investigate this result, the crystallographic orientation of nanowire arrays deposited with *c(Sb)* 0.015 mol/L was investigated as function of wire diameter. The measurements are presented in the next section.

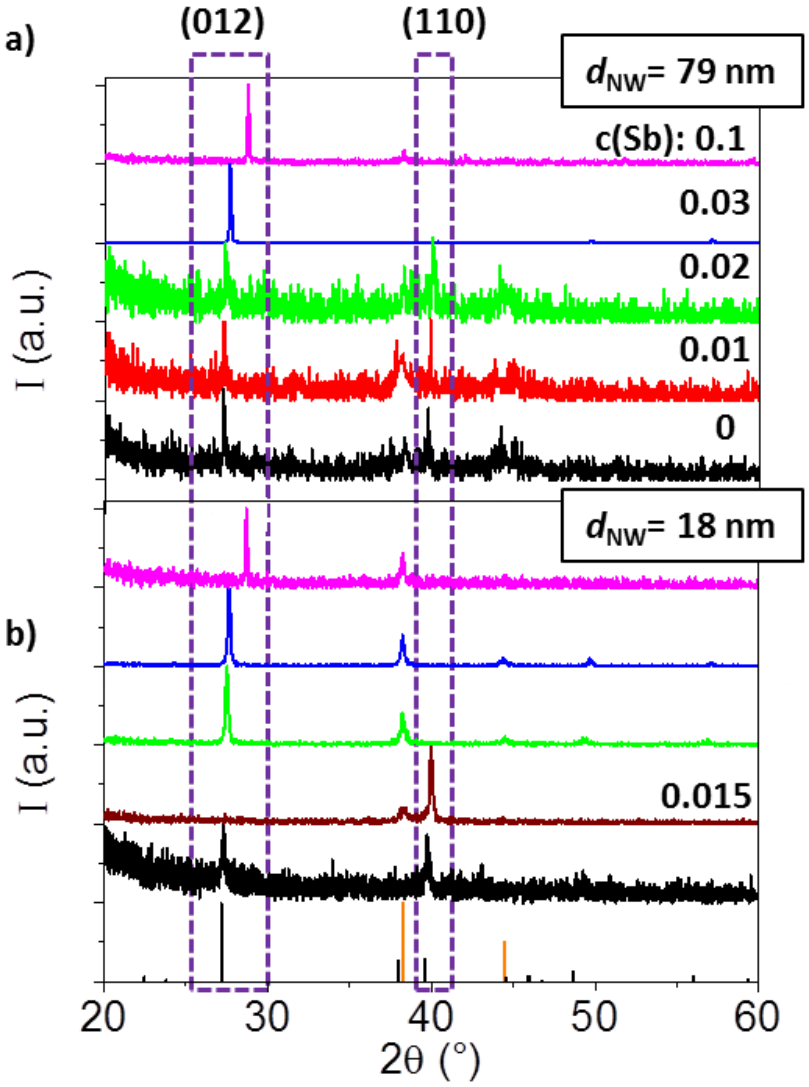


Figure 2.11: X-ray diffractograms measured on (a) arrays of $Bi_{1-x}Sb_x$ nanowires with diameter (79 ± 8) nm, made by pulsed deposition with $U_1$ = -220 mV vs. SCE for $t_1$ = 20 ms and $U_2$ = -150 mV vs. SCE for $t_2$ = 100 ms and different *c(Sb)* in the electrolyte. (b) arrays of $Bi_{1-x}Sb_x$ nanowires with diameter 18 ± 3 nm deposited applying $U_1$ = -250 mV vs. SCE for $t_1$ = 20 ms and $U_2$ = -150 mV vs. SCE for $t_2$ = 100 ms and different *c(Sb)* in the electrolyte. Vertical lines in the bottom graph indicate the standard powder diffraction pattern of Bi (black) and Au (orange), as provided in ref. [SPP]. Legend for (a) and (b) of different concentration of Sb ions in the electrolyte used for the deposition, *c(Sb)* = 0 (black), 0.01 (red), 0.015(brown) 0.02 (green), 0.03 (blue), 0.1 (magenta) mol/L. The Sb content in the nanowires depends on the *c(Sb)* in the electrolyte. The calculations of the composition *x* of $Bi_{1-x}Sb_x$ nanowires are presented in figure 2.12.

From figure 2.11, we calculated the texture coefficients (*TC*), using Eq. 2.6, for all nanowire arrays of ~ 79 nm and ~ 18 nm diameter, taking in consideration only two dominant reflections, namely (012) and (110). For both wire diameters, an increase of the Sb concentration in the electrolyte results in an increase of the crystals oriented with the (012) planes perpendicular to the wire axis (figure 2.12 (a)). A similar dependency was reported for ~ 79 nm diameter $Bi_{1-x}Sb_x$ nanowire arrays deposited potentiostatically increasing the Sb concentration in the electrolyte [Mül12a].

Thus, using pulsed deposition increases the growth uniformity and does not affect the preferred orientation of the nanowires. However, the best orientation for thermoelectric application is along the trigonal axis [Lin00] which was not detected in none of our nanowires.

The XRD patterns in figure 2.11 (a) and (b) exhibit a clear shift of the (012) and (110) reflection peaks to larger angles for higher Sb concentration (see purple dashed boxes). The crystalline structure of Bi and Sb belongs to the same space group and this shift confirms that the lattice parameters change with increasing *c(Sb)* [Dis68]. This was also observed for $Bi_{1-x}Sb_x$ nanowires deposited potentiostatically [Mül12a]. Using Bragg's law (Eq. 2.5), it is possible to determine the interplanar distance *d*(*hkl*) for each set of planes. We compared out values with the unit cell data in ref. [Dis68] to determine the Sb composition (*x(Sb)*) in the nanowire. Figure 2.12 (b) shows the *x(Sb)* values as a function of the electrolyte composition obtained by both XRD and EDX in STEM-SEM mode. The *x(Sb)* in the nanowires becomes larger with increasing the concentration of Sb ions *c(Sb)* in the solution. This behavior was also reported for potentiostatic depositions [Mül12a]. The experimental composition uncertainties in the plots are given by the standard deviation obtained by SEM-EDX measurements on several single nanowires from the same array, and by the full width at half maximum of the XRD diffractogram reflection peaks.

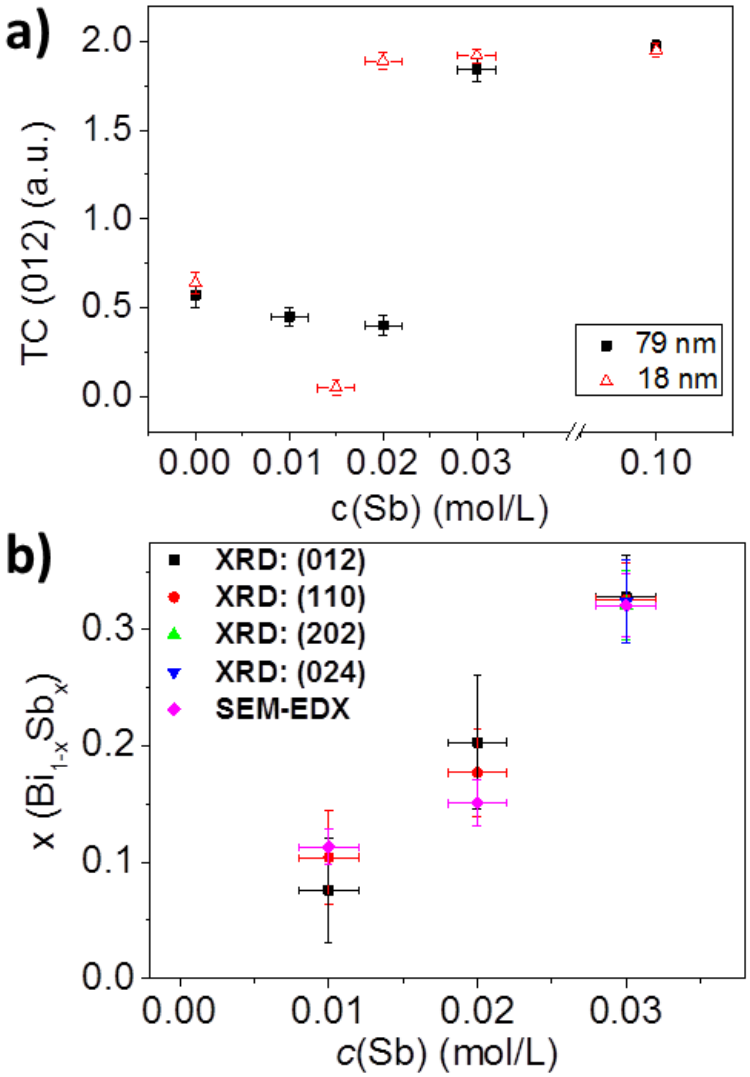


Figure 2.12: (a) Texture coefficients TC for the (012) reflections calculated from the XRD diffractograms reported in figure 2.11 for $Bi_{1-x}Sb_x$ nanowire arrays with nanowire diameter (79 ± 8) nm (black full square) and (18 ± 3) nm (red open triangle) as a function of different *c(Sb)* in the electrolyte. (b) Composition *x* of $Bi_{1-x}Sb_x$ nanowires with diameter 79 ± 8 nm as a function of *c(Sb)* comparing the evaluation of the XRD peak positions, reported in figure 2.11 (a), with the data in ref. [Dis68], and SEM-EDX analysis.

Nanowires synthesized by pulsed deposition (figure 2.7 (c)) were further analyzed by TEM. The orientation of the crystal *c* axis with respect to the nanowire axis was determined from electron diffraction patterns acquired at various selected regions of the nanowires , using an electron beam spot of ~ 750 nm [Per07]. The crystallite sizes were determined by TEM dark-field images in two-beam diffraction conditions [Eyi01, Per12]. Figure 2.13 reports the images of nanowires electrodeposited with *c(Sb)* = 0.02 mol/L in the electrolyte. Figure 2.13 (a) shows a collage of bright-field TEM images of a wire with ~ 21 µm in length and ~ 88 nm in diameter. Along the wire, several selected area

electron diffraction (SAED) patterns were acquired at positions indicated by blue marks in the bright-field image. The black-white contrast of the SAEDs was inverted for better visibility. The SAED data clearly shows the (00*l*) reflections and an angle of about 82° between the 00l direction and the wire axis in the central part of the nanowire. At outer sections, the inclination angles are slightly smaller between 67° and 80°. The SAED data provide evidence of single crystallinity for segments up to 10 µm long, which yields almost perfect electronic transport along the basal plane.

Dark-field TEM imaging of the same nanowire, presented in figure 2.13 (b), shows a ~ 2 µm long single-crystalline segments interrupted by 30 nm short crystallites (indicated by red arrows) and dislocations (D) oriented perpendicular to the wire axis. In comparison, wires deposited potentiostatically with the same electrolyte exhibited a polycrystalline structure with crystallite size of 100 nm in length [Mül12a].

In conclusion, our results reveal that $Bi_{1-x}Sb_x$ nanowire arrays synthesized by both pulsed and potentiostatic deposition exhibit a similar preferential orientation of the grains in the wire, texture coefficient and a controlled linear increase of the Sb concentration as a function of the Sb concentration in the electrolyte. However, TEM SAED data and dark-field imaging of pulsed-deposited nanowires evidence larger single-crystalline sections for pulsed deposition compared to potentiostatic deposition, in agreement with the corresponding cap morphologies observed by SEM on top of the membranes (figure 2.10).

The larger single-crystallinity and the higher growth homogeneity make the pulsed deposited samples suitable for the study of the thermoelectric properties of $Bi_{1-x}Sb_x$ nanowires [Cas15a]. In order to understand subsequent measurements of the thermoelectric properties, the crystallographic orientation and composition of the wires need to be studied as function of the wire diameter. This is described below.

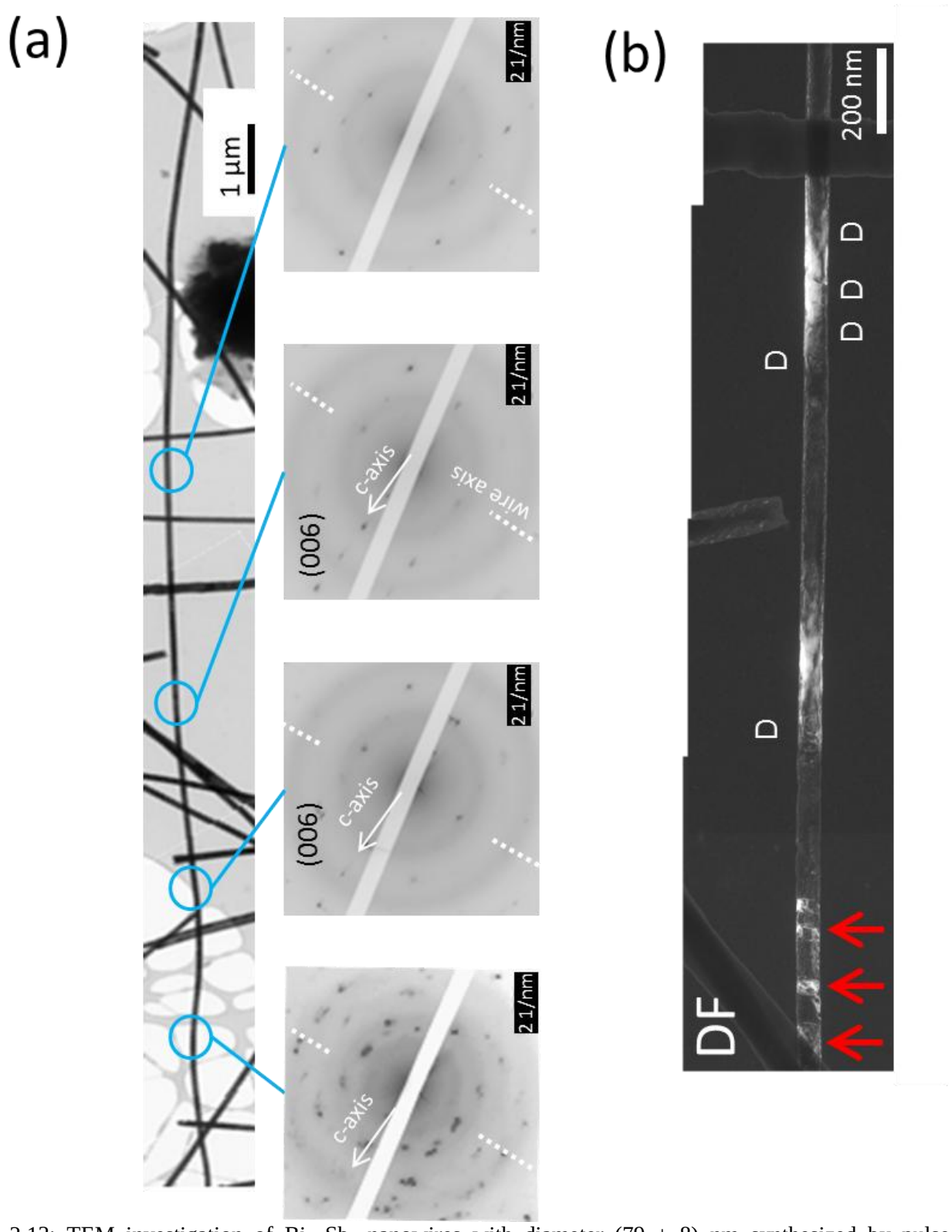


Figure 2.13: TEM investigation of $Bi_{1-x}Sb_x$ nanowires with diameter (79 ± 8) nm synthesized by pulsed deposition and with *c(Sb)* = 0.02 mol/L in the electrolyte. (a) collage of bright- field TEM images (left) and diffraction patterns (right) acquired at blue marks. The dotted lines indicate the nanowire axis. (b) Collage of TEM dark-field images of a nanowire grown under the same deposition conditions showing an ~ 2 µm long single-crystalline segment. Presence of dislocations perpendicular to the wire axis (D) and short crystallites (red arrows) are indicated.

The investigation of the thermoelectric properties of nanowires as a function of size is interesting because theoretical predictions have pointed out an enhancement of these properties due to the presence of finite- and quantum-size effects [Hic93a, Tan14]. In principle this requires to fabricate structures with various diameters but keeping all the other relevant parameters, including preferred orientation, composition and crystallinity, constant. However, for most synthesis methods, including the template electrodeposition, the resulting crystallographic characteristics may vary as a function of wire size.

We studied the influence of the channel diameter on the resulting nanowire array characteristics by electrodepositing $Bi_{1-x}Sb_x$ in a series of membranes with same channel characteristics as in the two previous sections, namely channel density ~ $7\times10^8$ $cm^{-2}$ and length 30 µm, but different channel diameters, namely (130 ± 10) nm, (79 ± 8) nm, (30 ± 4) nm, and (18 ± 3) nm. Three series of nanowire arrays were deposited at room temperature applying $U_1$ = -250 mV vs. SCE for $t_1$ = 20 ms and $U_2$ = -150 mV vs. SCE for $t_2$ = 100 ms, each using a different electrolyte composition, namely *c(Sb)* = 0, 0.015, and 0.1 mol/L.

Figure 2.14 presents the corresponding XRD spectra measured on wires (a) Sb (*c(Sb)* = 0.1 mol/L, (b) $Bi_{1-x}Sb_x$ (*c(Sb)* = 0.015 mol/L) and (c) Bi (*c(Sb)* = 0 mol/L). The pure Bi nanowire arrays in figure 2.15 (c) display two main reflections for all wire diameters, namely (012) and (110). The ratio between both reflections is similar to the ratio measured for the Bi nanowires with diameter ~ 79 and ~ 18 nm applying a slightly less negative reduction potential (black curves in Figs. 2.11 (a) and (b), respectively). The XRD patterns of pure Sb nanowire arrays (Fig. 2.14 (a)) exhibit only a (012) reflection for all nanowire diameters and smaller reflections for (202) and (024) directions, detected at $2\theta$ = 51.57° and 59.37°, respectively, for thicker wires. All patterns are in agreement with data in figure 2.11. In turn, XRD performed on $Bi_{1-x}Sb_x$ nanowire arrays (figure 2.14 (b)), with intensities normalized to the (110) reflection, display a preferential (110) orientation, which is more pronounced for smaller wire diameters. These results show that under pulsed deposition conditions, the nanochannel size does not influence the crystalline orientation of the deposited material in the case of pure Bi and pure Sb wires, whereas it affects the preferred orientation of the deposited $Bi_{1-x}Sb_x$ alloy. Since $Bi_{1-x}Sb_x$ alloy presents large anisotropy properties [Len98], this must be taken into careful consideration when analyzing thermoelectric properties of alloy nanowire arrays.

Finally, figure 2.15 shows the composition of $Bi_{1-x}Sb_x$ nanowire arrays deposited with an electrolyte containing *c(Sb)* = 0.015 mol/L as function of the wire diameter. The analysis was performed by XRD and SEM-EDX as discussed in the previous section. For both methods, the results indicate a slightly increase of the Sb concentration *x(Sb)* in thinner wires, but in good agreement with *c(Sb)* in the electrolyte.

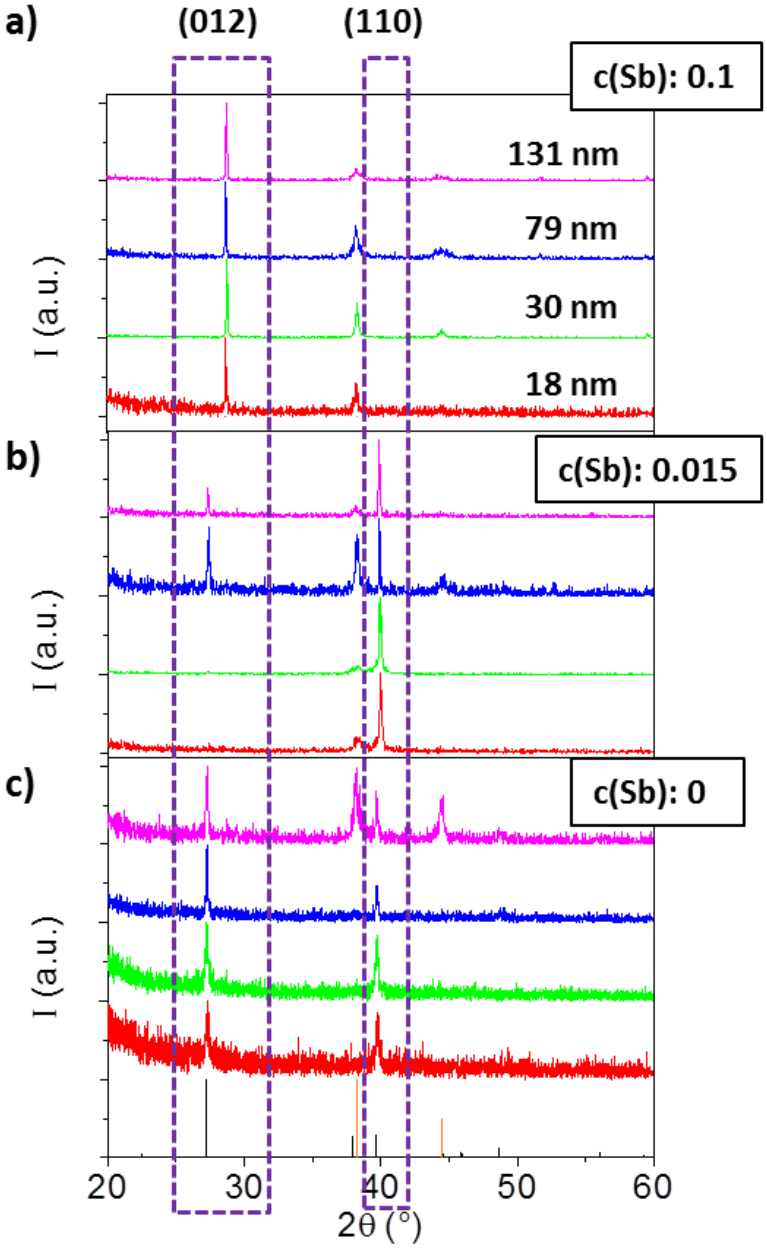


Figure 2.14: (a) X-ray diffractograms measured on $Bi_{1-x}Sb_x$ nanowire arrays grown by pulsed deposition with electrolytes of different *c(Sb)*: (a) 0.1, (b) 0.015, and (c) 0 mol/L. Legend for (a), (b), and (c) of different nanowire diameter: 131 ± 10 nm (magenta), 79 ± 8 nm (green), 30 ± 4 nm (blue), and 18 ± 3 nm (red). The vertical lines in the bottom of the graph indicate standard powder diffraction pattern of Bi (black) and Au (orange), according to Ref. [SPP].

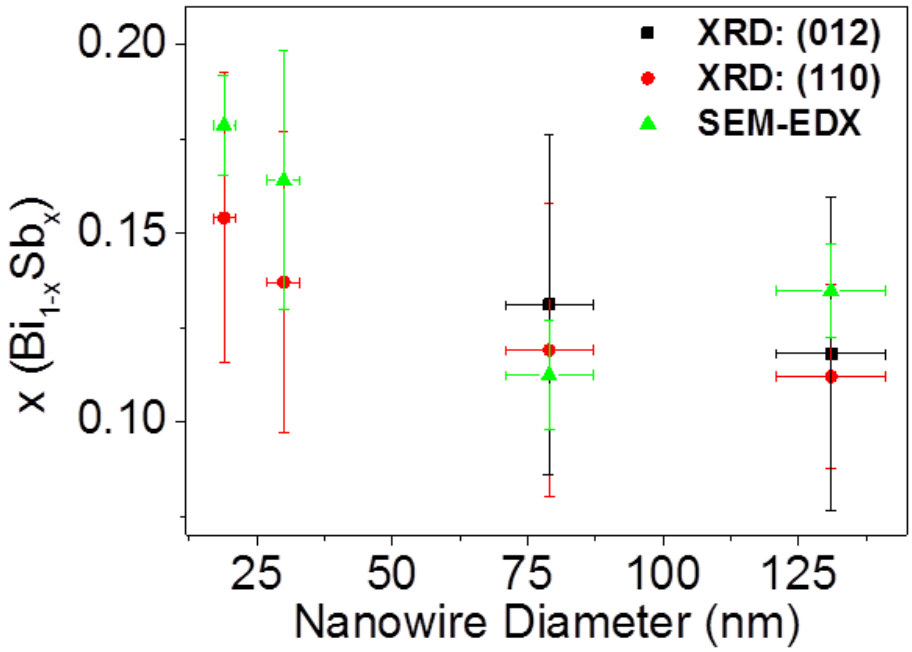


Figure 2.15: Sb content *x(Sb)* of $Bi_{1-x}Sb_x$ nanowire as a function of nanowire diameter ($D_{NW}$) obtained from XRD and SEM-EDX analysis. The wires were deposited with *c(Sb)* = 0.015 mol/L. The corresponding XRD diffractograms are reported in figure 2.14 (b).

## 2.4 Resume of Nanowire Analysis

Summarizing the obtained results regarding the crystallographic characteristics of $Bi_{1-x}Sb_x$ nanowires synthesized both by potentiostatic and pulsed deposition in etched ion-track membranes, we can clearly state that pulsed depositions lead to a more uniform nanowire growth rate of nanowires, and to a more homogeneous filling of the template nanochannels. In addition, pulsing the applied reduction potential does not affect significantly the preferred crystallographic orientation and the composition of the nanowires, but yields larger grain sizes. Additional TEM analysis reveals several µm long, single-crystalline wire sections. Both X-ray diffraction and SEM-EDX analysis indicate that the Sb concentration in the wires can be adjusted by varying the concentration of Sb ions in the electrolyte, as for potentiostatic conditions. The composition and the crystallographic orientation of pulsed-deposited nanowires show only a weak dependence on the wire size.

To conclude, pulsed electrochemical deposition of $Bi_{1-x}Sb_x$ nanowires in the pores of polycarbonate membranes yields excellent control over composition, size and crystallographic orientation of nanowires [Cas15a]. The obtained narrow length distribution is a mandatory requirement for thermoelectric characterization of nanowires and for the development of nanowire-based sensors.

# 3. Seebeck Coefficient and Resistance Measurements of $Bi_{1-x}Sb_x$ Nanowire Arrays

The Seebeck coefficient, or thermopower, is a property of the material that gauges the magnitude of the induced thermovoltage in response to a gradient of temperature applied across the material [Gold10, Row06]. This number manifests the presence of the Seebeck effect within the material, due to thermal diffusion of the charge carriers (electrons or holes) towards the cold side of the system [Ala13, Szc11]. As presented in the introduction, for thermoelectric applications, i.e. thermoelectric power generators or as thermoelectric coolers, high Seebeck coefficients are necessary in order to produce significant amount of electrical power when applying small gradients of temperature or vice-versa [Dav11, Kas01].

In general, $Bi_{1-x}Sb_x$ alloy nanowires are expected to exhibit different thermoelectric properties compared to bulk materials if the wire diameter is small enough for quantum- and finite-size effects [Dre99, Hic93a]. Theoretical calculations based on semi-classical Boltzmann transport equations support this idea suggesting a higher thermoelectric figure-of-merit *ZT* (defined in equation 1.4) when decreasing the wire diameter and adjusting doping [Lin00, Tan14b]. A value of *ZT* around 1.5 is predicted for Bi nanowires with diameter ~ 15 nm, and even *ZT* ~ 2.5 for ~ 40 nm diameter $Bi_{1-x}Sb_x$

alloy nanowires with $x$ = 0.13 [Rab01], while for bulk $Bi_{1-x}Sb_x$ with $x$ = 0.16 a $ZT$ ~ 0.5 was measured at 70 K [Iss79].

Despite these promising theoretical predictions, comprehensive and systematic measurements of the thermoelectric properties, namely Seebeck coefficient, and thermal and electrical conductivity of $Bi_{1-x}Sb_x$ alloy nanowires as a function of wire diameter and composition are scarce [Tan14].

The difficulties concern the synthesis of $Bi_{1-x}Sb_x$ alloy nanowires with the desired geometrical and compositional characteristics as well as contacting single nanowires to measure the value of the thermoelectric properties without affecting the chemical and mechanical properties.

Although special chips were already developed to obtain reliable thermoelectric measurements of individual nanowires [Völ09, Zho05, Wha12], the electrical contacting is still challenging. At present, only few measurements of the electrical resistance and thermopower of single Bi nanowires are available [i.e., Bou06, Has09] and only recently, the $ZT$ of single Bi nanowires synthesized by the on-film formation method were presented for wire diameters between 180 and 20 nm [Kim15]. The advantage of our template synthesis is the fact that the measurements of the Seebeck coefficient can be performed on nanowire arrays embedded in the polymer matrix. The Seebeck coefficient is independent of the number of wires connected, making the measurement on nanowire array as informative as on single nanowires [Dre03, Her99].

Heremans et al. reported measurements of the electrical resistance of both Bi [Her00] and Sb [Her01] nanowire arrays with wire diameters decreasing from 200 to 10 nm. The measured nanowire arrays were deposited in porous alumina templates through vapor-deposition technique. However, the authors showed only measurements of the Seebeck coefficient of a Bi nanowire array with wire diameter of 200 nm testing different solutions to find suitable thermal contacts for the experiment [Her99]. In particular, the measured thermopower for such large wire diameter was reported to be lower than the value expected for bulk Bi, although the authors used both silver paint and Wood's metal to enhance the thermal contact between sample and measuring unit [Her99]. The fact that the thermal conductivity of the alumina template is relatively high may have influenced the results.

The measurements of the electrical resistance for various wire compositions was reported by Lin et al. for $Bi_{1-x}Sb_x$ nanowire arrays with diameter of 65 [Lin02] and 45 nm [Lin01, Zha99] with $x$ = 0, 0.05 and 0.15. Here, the nanowire arrays were synthesized by pressure injection of molten alloys into the nanopores of anodic alumina membranes. In this case, the Seebeck coefficient was measured on samples with only $x$ = 0 and 0.05, yielding respective room temperature values of -50 and -55 µV/K, for 65 nm wide wires [Lin02b].

The thermopower and electrical resistance of a Bi nanowire arrays deposited in porous anodic alumina templates by pressure injection was also measured by Huber et al. for wire diameters between

200 and 20 nm [Hub11]. In this case, the thermal contact to the sample was obtained by inserting a thin indium foil. The results showed a non-monotonic decrease of the thermopower as a function of the temperature for the different wire diameters. 200-nm thick Bi wires exhibited a Seebeck coefficient of -20 µV/K at room temperature. This value is much lower than the expected Bi bulk thermopower, which is ~ 60 µV/K [Yam02, Her02]. This difference may again underline the need of improving the thermal contacts.

Comparing the results from different groups is challenging or, actually, not possible. One reason is the usage of rather different setups, which yields different results depending on the thermal contact between the nanowire arrays and the metal contacts. A second reason is that the wires are synthesized using different methods leading to different crystallographic orientations, which strongly influences the highly anisotropic thermoelectric transport properties of $Bi_{1-x}Sb_x$ [Iss79]. Moreover, as described in the previous section, Bi and $Bi_{1-x}Sb_x$ nanowires electrodeposited in templates under identical conditions but in pores of different diameter exhibit different crystallographic orientations. When performing thermoelectric measurements the structure and composition of the nanowires should be well defined.

In this chapter, we present measurements of the Seebeck coefficient and electrical resistance of template-embedded $Bi_{1-x}Sb_x$ nanowire arrays. Using a custom-made experimental setup and after optimizing the thermal contacts to the nanowire arrays, we performed systematic measurements on $Bi_{1-x}Sb_x$ nanowire arrays varying both the wire diameter (between ~ 750 and ~ 40 nm) and composition ($0 \leq x \leq 1$) in an independent controlled manner. The wires for these measurements were previously characterized by X-ray diffraction and scanning and transmission electron microscopy (chapter 2), and their preferential crystallographic orientation and composition is taken into account during the data evaluation. We observed small variations of both crystallographic orientation and composition with decreasing wire diameter. This allows comparing the measurements of the Seebeck coefficient and electrical resistivity of the nanowire arrays as function of the wire size.

## 3.1 Experimental Details on Thermoelectric Measurements

In this section, we present the experimental setup for the measurements of the Seebeck coefficient and electrical resistance of our nanowire arrays. The design was previously specifically developed to perform the measurements on template-embedded nanowire arrays [Mül12b]. During this work, the setup was tested and optimized.

The measurements of the electrical resistance and of the Seebeck coefficient were performed on nanowires still embedded in polycarbonate membranes which are electrically insulating and possess a low thermal conductivity of ~ 0.19 W $m^{-1}$ $K^{-1}$ [Mob12]. The nanowire arrays were grown as described in chapter 2 [Cas15a]. To ensure electrical contact to the nanowire arrays, the electrodeposition of the wires was continued until small individual caps were formed on the membrane surface. Subsequently, a thin Au layer (~ 400 nm thickness) was sputtered onto the upper membrane surface covering the caps (and the pores in which the wires have not yet reached the top), forming a homogenous continuous top contact layer.

To investigate the influence of the caps on the top of the array on both electrical and thermal contacts, series of samples were produced with different average cap size by varying the deposition time. To study the influence of nanowire diameter and composition on both electrical resistance and Seebeck coefficient, series of nanowire arrays with wire diameters between 753 ± 37 nm and 41 ± 5 nm and compositions of the $Bi_{1-x}Sb_x$ nanowires between $0 \leq x \leq 1$ were synthesized and characterized.

Figure 3.1 (a) depicts the schematic of the setup employed for the Seebeck measurements. A nanowire array embedded in the polycarbonate membrane (1) is placed between two massive copper blocks (2). On each block two gold-plated electrical contacts (3) and one Si diode (4) are attached. The embedded sample and the copper blocks are fixed in between two stainless steel frames (5), held together by thermally insulating nylon screws (6) and covered with a metal shield (9), consisting of many layers of thin thermal isolation material. This setup was mounted onto a cooling finger (7), with a heating wire coiled around (8).

The measurements were performed in a vacuum chamber at a pressure of $10^{-6}$ mbar (attained by a pre-vacuum and a turbomolecular pump). The cryostat COOLPAK 6000 with helium evaporation cooler allows the cooling of the setup down to 20 K. The temperature of the system is regulated by a LakeShore 336 temperature controller, which heats up the wire, coiled around the cooling finger. Electrical measurements were performed using a Keithley 2182A Nanovoltmeter and a Keithley 2400 Sourcemeter. Figure 3.1 (b) shows a photograph of the sample holder mounted on the cooling finger and inside the chamber. First, the resistance of the nanowire array was measured as a function of the temperature. Afterwards, high grade thermal compound (fig. 3.1(a) – (10)) by Prolimatech, composed

of about 80% Al, was applied on both sides of the nanowire array to improve the thermal contact between the sample and the copper blocks.

Figure 3.1 (c) presents schematically the connections and measuring devices of the setup, as well as the different temperatures defined for the evaluation of the results. The temperatures on the Cu blocks at the bottom, near the cooling finger, and at the top are named $T_A$ and $T_B$ and are measured by the diodes *A* and *B*, respectively. To improve the thermal contact, thin layers of indium were inserted between the copper and the Si diodes. The diode *A* was used as calibrated by LakeShore, providing an absolute accuracy of 0.25 K. Diode B was self-calibrated to diode A, reducing the resulting error $T_A$-$T_B$ to 0.02 K. $T_A$ and $T_B$ were recorded using the LakeShore 336 temperature controller, with which we also adjusted the power of the heating wire and so, the rate at which the set temperature was reached during the measurements.

The voltage at zero current $U(0)$ and the *I-U* curves were measured with the Keithley 2182A Nanovoltmeter and the Keithley 2400 Sourcemeter, respectively. Leads to contacts and sensors were made by a non-magnetic phospor bronze by LakesShore, which exhibits low thermal conductivity and Seebeck coefficient over the whole temperature range (< 1 µV/K) [Sha08].

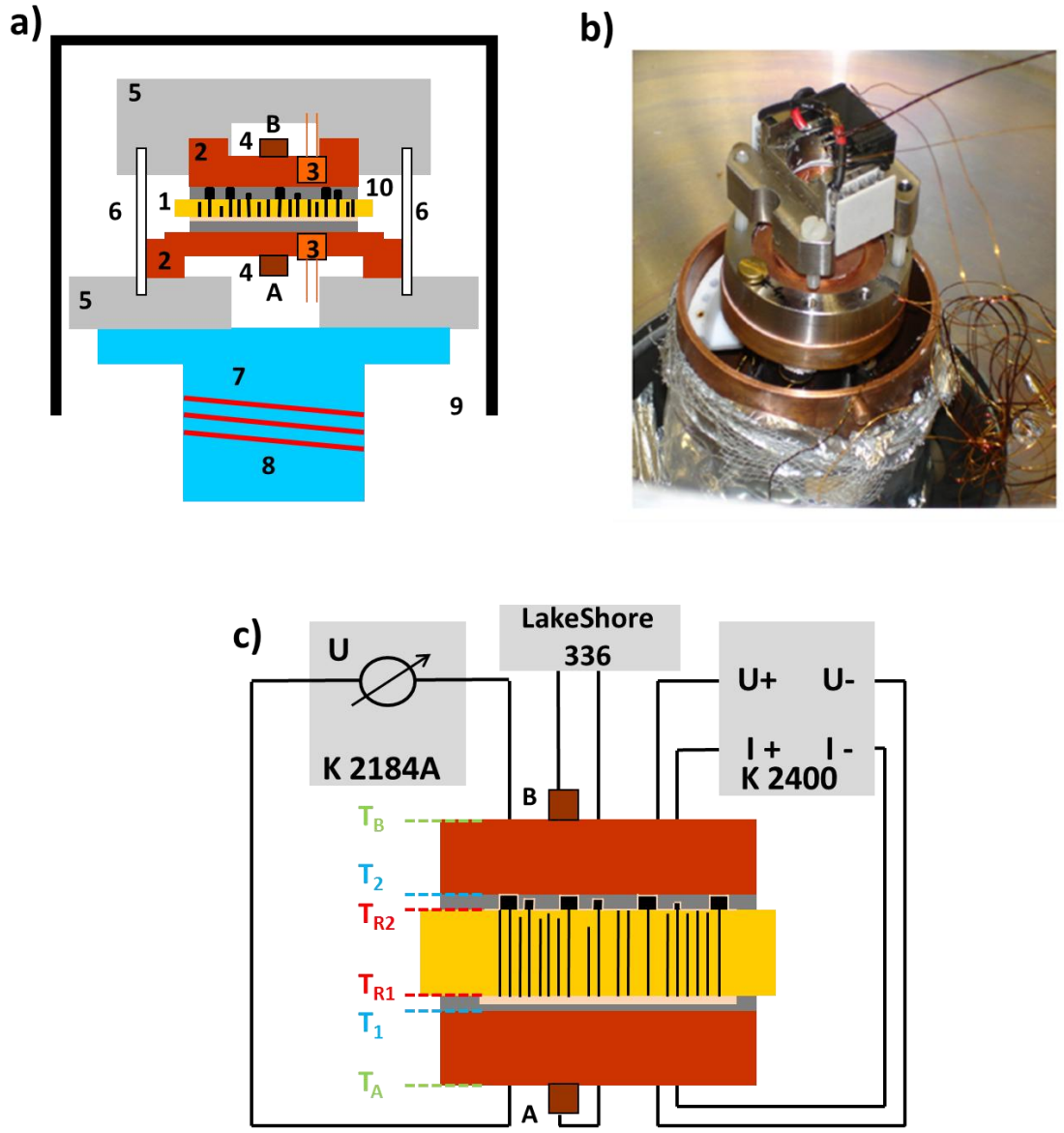


Figure 3.1: (a) Schematic of sample holder: (1) nanowire array sample, (2) copper blocks, (3) electrical contacts, (4) Si diode A and B, (5) stainless steel frames, (6) nylon screws, (7) cooling finger, (8) heating wire, (9) metal shield, (10) thermal paste. (b) Photograph of sample holder on the cooling finger mounted in the chamber. (c) Schematic of sample between two copper blocks. The temperatures and electrical contacts are indicated.

The general equation for the evaluation of both electrical resistance and Seebeck coefficient is given by:

$$U = RI + S\Delta T \quad . \tag{3.1}$$

The equation points out that the resistance of the nanowire array $R$ can be obtained from the slope of the $I$-$U$ curves. During the data acquisition the current was swept between $-I_{MAX}$ and $I_{MAX}$ to determine $R$. $I_{MAX}$ was kept low (maximum ~ mA) to minimize the Joule heating and the heat transfer by Peltier effect between the two sides of the sample [Wan13]. Subsequently, the voltage at zero

current, $U(0)$, as well as the temperatures $T_A$ and $T_B$ are measured and used to calculate the Seebeck coefficient, as reported in equation 3.2.

Figure 3.2 displays a representative set of data, recorded and employed for the evaluation of the Seebeck coefficient and the electrical resistance of a Bi nanowire array with wire diameter 130 ± 10 nm and length 30 µm. Figure 3.2 (a) shows the temperatures $T_A$ (red) and $T_B$ (blue) recorded at various temperatures from 300 K down to 30 K. The temperature set point was varied every 60 minutes in steps of 30 K and the temperature was let oscillating around the set points. As notable in the inset of figure 3.2 (a), $T_A$ oscillates around the set point, in this case 300 K. $T_B$ follows the change of temperature but with a certain time delay, since the upper copper block is thermally separated by the nanowire array embedded in the polycarbonate membrane and the nylon screws, as visible in the inset of figure 3.2 (a). The magnitude of the temperature oscillations above and below the set points can be adjusted by PID (proportional, integral and derivative) control system of the LakeShore 336. These oscillations create a temperature gradient between the two sides of the sample, which in turn induces a thermal voltage $U(0)$ as a function of the temperature difference $\Delta T = T_A - T_B$ for all ten selected set temperature points.

The related induced voltage $U(0)$ values are displayed in figure 3.2 (b). The voltage varies between +10 µV and -10 µV during the temperature oscillations around the set point and presents higher voltage values due to a larger temperature gradient during the transition to the next set temperature point. The data during the transitions were not used for the subsequent evaluation of the thermopower.

The Seebeck coefficient is obtained from the slope of the linear fit:

$$S = \frac{U(0)}{\Delta T} \quad . \tag{3.2}$$

The voltage $U(0)$ and the temperature gradient $\Delta T$ include contributions from the copper blocks, thermal compound, and the leads of the setup.

Using linear approximations, the value $U(0)$ can be defined as:

$$U = S_{NW}\Delta T_R + S_{Comp}(\Delta T_C - \Delta T_R) + S_{Cu}(\Delta T - \Delta T_C) + S_{Lea}(\Delta T - \Delta T_C) \quad , \tag{3.3}$$

with $S_{NW}$, $S_{Cu}$, $S_{Comp}$ and $S_{Lea}$ being the Seebeck coefficient of the nanowire array, thermal compound layer, copper blocks and leads, respectively, and $\Delta T = T_A - T_B$ , $\Delta T_C = T_2 - T_1$ and $\Delta T_R = T_{R2} - T_{R1}$, as shown in figure 3.1(c). The Seebeck coefficient of the leads ($S_{Lea}$ < 1 µV/K) [Sha08], copper blocks ($S_{Cu}$ ~ 1.83 µV/K [Cus58]) and of the thermal paste ($S_{Al}$ ~ -1.8 µV/K) [Saf01] has negligible magnitude compared to Bi and Sb. Thus, the measured $U(0)$ is mainly given from the voltage created between both sides of the nanowire array.

To avoid underestimation of the thermopower, the measured $\Delta T$ needs to be as similar as possible to $\Delta T_R$ [Her99, Wer09]. In our setup, the copper blocks are ideal heat sinks due to their high thermal conductivity [Li92], making $\Delta T \approx \Delta T_C$. Adding a layer of thermal compound on both sides of the sample improves the thermal contact between the sample surface and the copper blocks, yielding $\Delta T_R \approx \Delta T_C \approx \Delta T$. Such thermal contacts allow a reliable evaluation of the Seebeck coefficient.

In some cases, $U(0)$ had a small voltage offset of few µV for null temperature gradient (few µV). The values remained constant while decreasing the temperature, and thus did not influence the measured Seebeck coefficient [Deb13].

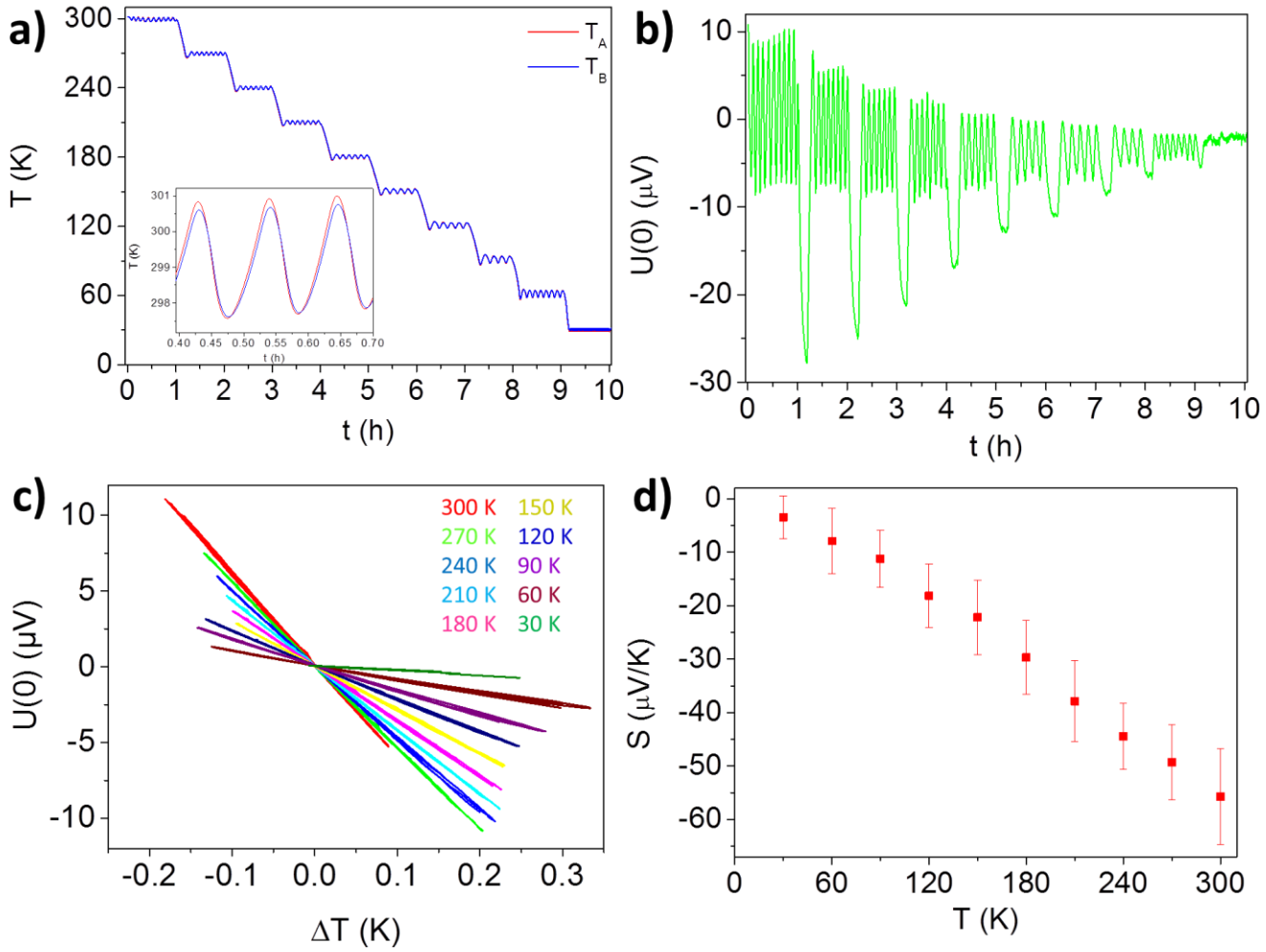


Figure 3.2: Experimental data evaluation of the Seebeck coefficient of Bi nanowire array with wire diameter of (130 ± 10) nm. (a) Measured temperature $T_A$ (red) and $T_B$ (blue) as a function of time during the oscillations. (b) Recorded voltage $U(0)$ created by the temperature different between the two side of the sample as a function of time. (c) Voltage $U(0)$ versus temperature gradient for ten different set temperature points. (d) Seebeck coefficient resulting from the linear fit of the slope reported in (c) for different set temperatures points as a function of the temperature averaged during the oscillations.

## 3.2 Optimization of Thermal Contacts

Here, we discuss the importance of optimizing the thermal contacts between the sample and the adjacent copper blocks to systematically and reliably investigate the Seebeck coefficient. For this, we performed different tests using arrays of Bi nanowires with wire diameter ~ 130 nm. For such a large wire diameter a thermopower value similar to the bulk material is expected.

Figure 3.3 (a) shows SEM images of the top surfaces (investigated area ~ 0.04 $mm^2$) of samples at different time of caps growth. From the time at which the current started to increase (phase 3 of figure 2.4 in chapter 2), the deposition was continued for 5 (blue), 15 (green), 30 (red) and 60 (black) minutes, respectively. After 5 minutes, the top surface exhibits a low number of small caps (5-15 μm). After 15 minutes of growth, the size and density of the caps increased, and the caps started to coalescence (phase 4 of figure 2.4). Density and size continue to increase after 30 minutes of growth and at 60 minutes the surface is almost totally covered by overlapping of caps.

All four samples were prepared and mounted identically for the thermopower measurements without applying the thermal compound. Figure 3.3 (b) presents their corresponding measured Seebeck coefficients. The thermopower for the Bi nanowire arrays at room temperature increases as enhancing the caps density on the top of the membrane, from ~ -13 μV/K for 5 minutes caps growth (blue data) to ~ -43 μV/K for 60 minutes (black data).

Since the nanowire arrays characteristics of all four samples are identical (same deposition conditions, same diameter, same orientation), the increase of the measured Seebeck coefficient for longer caps deposition times indicates a smaller gradient of temperature caused by an improved thermal contact between the top surface and the Cu block. This also means that the lower measured values of Seebeck coefficient for samples with lower caps density is due to suboptimal thermal contact. This might be due to large spaces between caps and membrane and Cu block. On the other hand, the presence of overlapping caps is similar to a Bi thin film on the top of membrane. To avoid caps contribution to the measured thermopower, the cap growth needs to be interrupted for small cap sizes and before start to coalescence, i.e. after 5 minutes of growth. This condition was set for all samples subsequently measured.

To reduce heat losses, the thermal compound was applied on the top of the membrane to fill the space between the caps and form a homogenous contact layer to the copper block. This arrangement allowed us to improve the accuracy of the detected temperature on the surface of the sample.

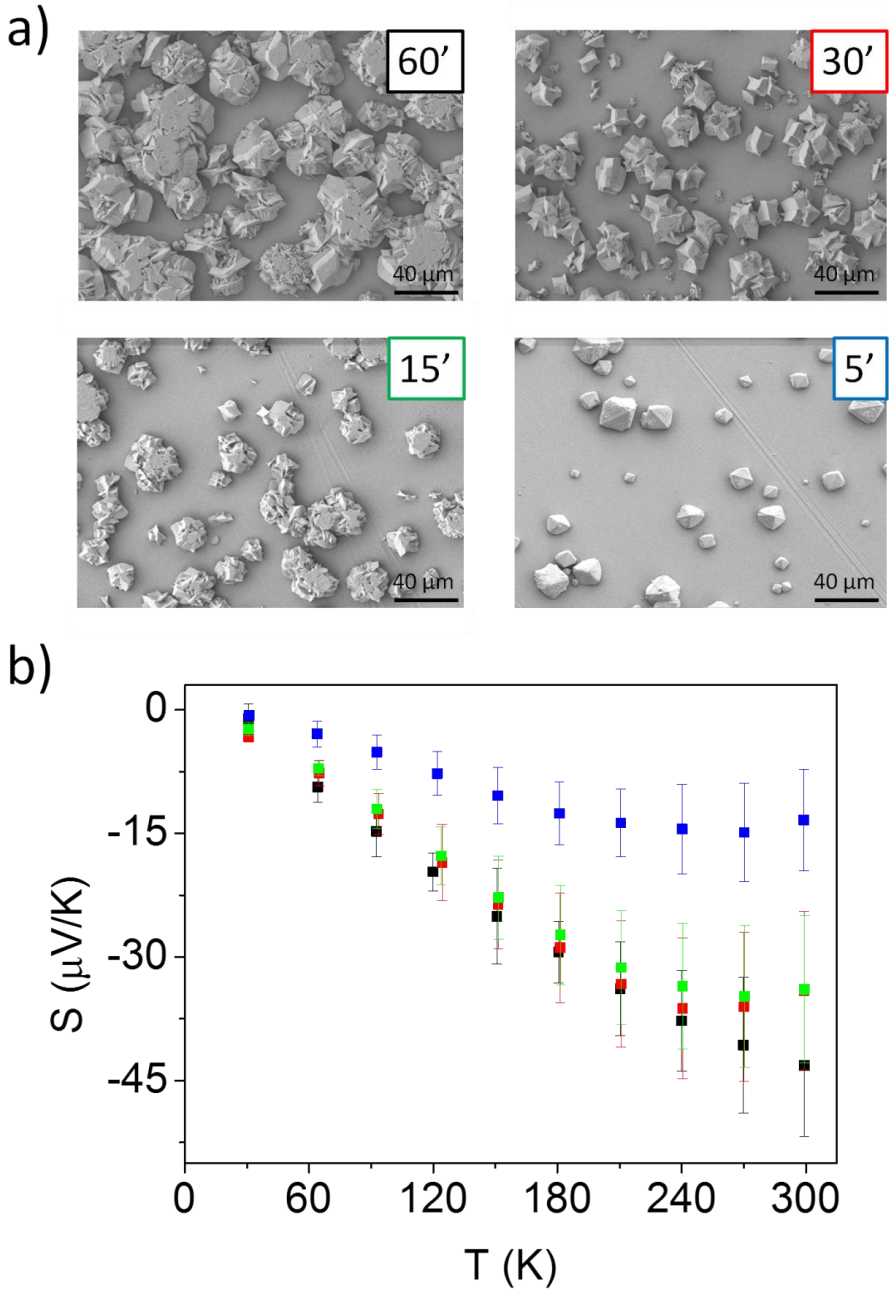


Figure 3.3: Seebeck coefficient of Bi nanowire arrays with wire diameter of 130 ± 10 nm as a function of temperature and cap size and density. (a) SEM images of the top surface of the membrane with caps grown for 5 (blue), 15 (green), 30 (red) and 60 (black) minutes. (b) the corresponding measured Seebeck coefficient.

Also the accuracy of the measured Seebeck coefficients values depends strongly on a precise determination of the temperatures detected on the two sides of the sample [Wer09, Her00]. As visible by Eq. 3.2, an overestimation of the calculated temperature difference leads to an underestimation of the corresponding thermopower.

The thermal compound has a high thermal conductivity (~ 10.2 W $m^{-1}$ $K^{-1}$) [Pro], making it possible to decrease the difference between the temperatures detected by the two Si diodes ($T_A$ and $T_B$) and the actual temperature of the sample surfaces ($T_{R1}$ and $T_{R2}$). The optimal amount of thermal paste should

be such that it just fills the space between the caps and that the creation of high thermal resistances film at the contacts between the individual caps and the copper block is avoided. We found that the best thermal contacts were achieved by adding ~ 34 mg to the sample surfaces (~ 12 $cm^2$), leading to the highest value of Seebeck coefficient for each samples. Applying this procedure, the resulting temperature gradient decreased significantly to values < 1 K.

To investigate the influence of the temperature gradient on the Seebeck coefficient values, we performed additional measurements on Bi nanowire arrays by mounting a second heating wire on the upper block near the sample surface, as schematically presented in figure 3.4 (a). In this way we were able to create larger temperature gradients (up to 3 K) by heating up the upper sample surface stronger than the lower surface. Figure 3.4 (b) reports the temperatures measured around the set point at 270 K, using the two heating wires. The temperature $T_B$ is higher than $T_A$ and the difference is about 2 degrees, thus larger than the one reported for one heating wire (inset of figure 3.2 (a)).

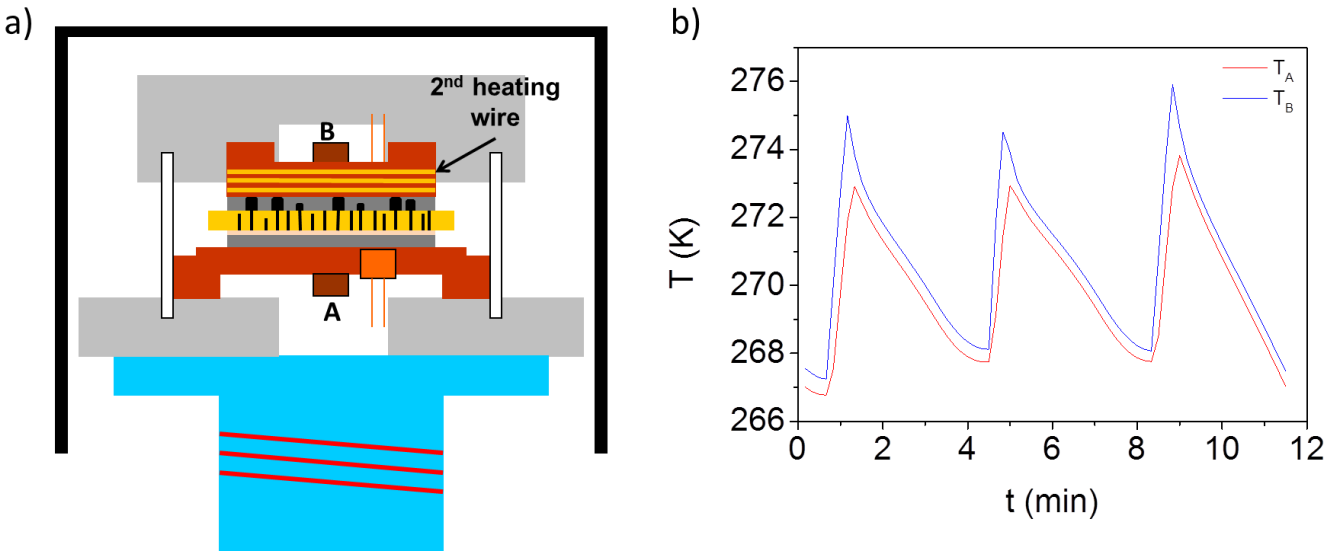


Figure 3.4: (a) Schematic of sample holder setup with second heating wire placed on the top cooper block electrode. (b) Measured temperature $T_A$ (red) and $T_B$ (blue) as a function of time during the oscillations of temperature caused by the two heating wires, causing a large temperature gradient between the two sides of the sample.

Figure 3.5 (a) and (b) present the $U(0)$-$\Delta T$ data at 300 and 240 K, respectively. As expected the temperature gradient increases from ~ 0.5 K for measurements with one heating wire, to ~ 3 K using also the second wire. The resulting Seebeck coefficients are very similar for both settings. At 300 K, we calculated a thermopower of -40 ± 4 µV/K for one and -38 ± 3 µV/K for two heating wires, respectively. At 240 K, the corresponding evaluated values are -36 ± 3 µV/K and -35 ± 3 µV/K. The

good agreement demonstrates that the determination of the Seebeck coefficient can also be undertaken with one heating wire.

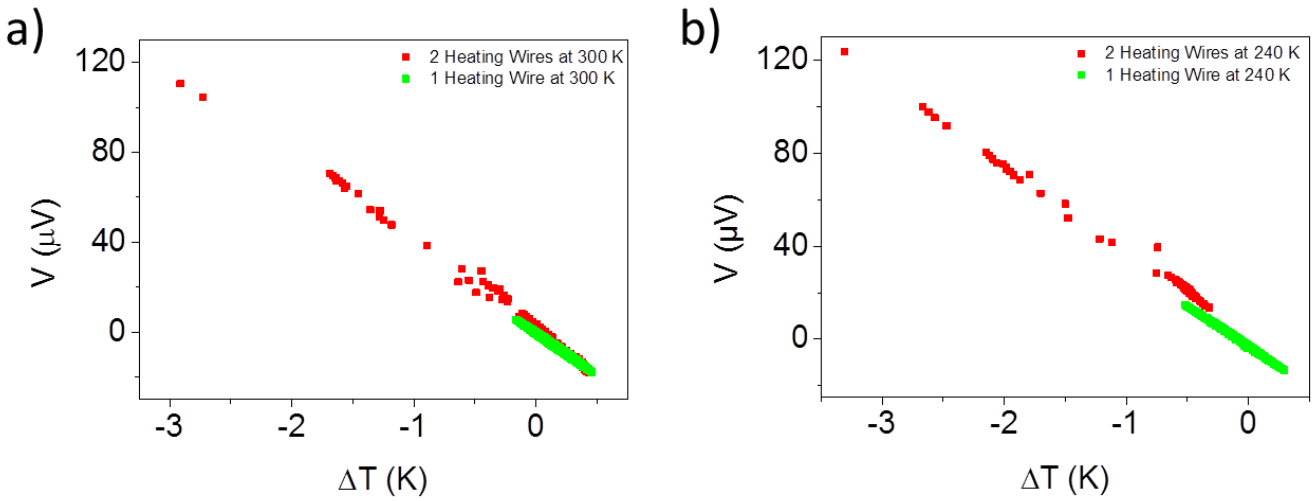


Figure 3.5: Thermovoltage as a function of temperature gradient of a Bi nanowire array with wire diameter of (79 ± 8) nm at (a) 300 K and (b) 240 K, using one heating wire (green) and two heating wires (red).

Finally, to test the accuracy of the measurements, we evaluated the Seebeck coefficient of a Cu nanowire array with wire diameter ~ 130 nm and compared the data with values reported for bulk Cu. Copper is a good model system to test the accuracy of our setup since metal elements possess a very low Seebeck coefficient (for bulk Cu ~ 1.83 µV/K at 300 K [Cus58]) and neither finite- nor quantum-size effects are expected. Thus, this allows us to test the sensitivity of the system at various temperature points with metal nanowire arrays which present the same geometry and both thermal and electrical contacts as the Bi-based sample that will be investigated afterwards.

Cu nanowires were electrodeposited in the pores of polycarbonate membranes under the same conditions as reported in [Toi03]. The measured wire array has caps on the top surface. After applying the right amount of thermal compound, the measurements were carried out and the evaluations are presented in figure 3.6.

The thermopower values of thick Cu wire (figure 3.6) are similar to experimental data reported for bulk Cu [Cus58, Bla76, Okr11]. This demonstrates that our experimental setup possesses a high sensitivity with respect to small voltage changes as function of thee temperature gradient between the two sides of the sample.

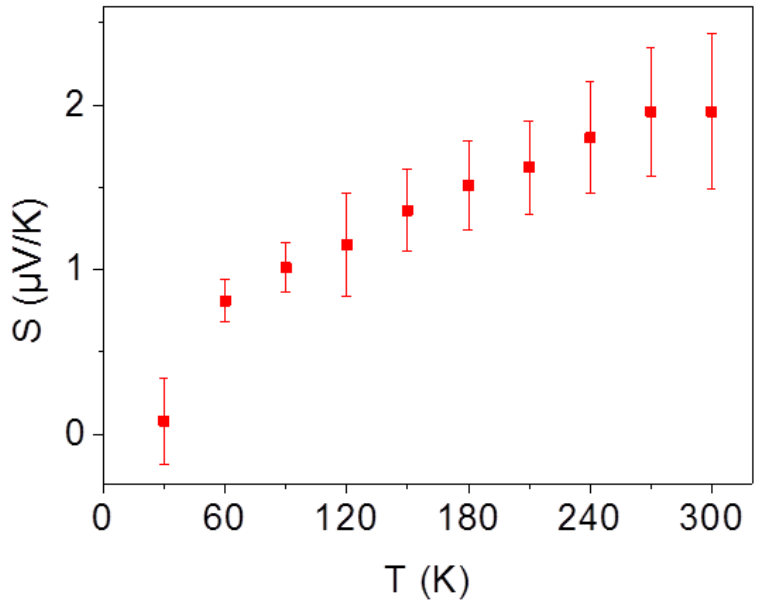


Figure 3.6: Experimental Seebeck coefficients of a Cu nanowire array with wire diameter of (130 ± 10) nm.

## 3.3 Seebeck Coefficient of $Bi_{1-x}Sb_x$ Nanowire Arrays

In this section the thermovoltage measurements of $Bi_{1-x}Sb_x$ alloy nanowires array with $0 \leq x \leq 1$ are presented. The wire diameter ranged from 753 ± 37 nm to 41 ± 5 nm and the temperatures varied between 300 and 20 K.

The nanowires were grown as discussed in detail in chapter 2. As revealed through X-ray diffraction and both transmission and electron microscopy investigations, the composition and the preferential orientation of the nanowires vary weakly as a function of nanowire size. In particular, for $Bi_{0.85}Sb_{0.15}$ nanowire arrays electrochemically deposited with a concentration of Sb (*c(Sb)*) in the electrolyte of 0.015 mol/L, compositional analysis revealed a slightly increase of the amount of Sb (*x(Sb)*) in the nanowire from 0.12 to 0.16 when lowering the wire diameter from ~ 130 nm to ~ 30 nm. X-ray analysis showed a preferential orientation along the (012) and (110) direction for Sb and $Bi_{0.85}Sb_{0.15}$ nanowire arrays, respectively. On the other hand, Bi nanowires X-ray diffractogramms displayed peaks along both the (110) and (012) direction [Cas15a].

Moreover, as presented in chapter 2, pulsed electrodeposition resulted in a more homogenous wire growth rate over the whole area (diameter ~ 10 mm) than in the potentiostatic case [Cas15a]. Although the Seebeck coefficient value is independent of the number of wires contacted during the measurements [Dre03, Lin02], homogenous growth of the nanowire array allows more wires to reach the top of the channel simultaneously, forming caps of similar size and being homogeneously

distributed over the membrane surface when the process is continued for a short time. This enhanced the chance for optimal electrical contacts of the sample within our setup.

Figure 3.7 (a) presents the experimental evaluations of the Seebeck coefficient of different nanowire arrays. For Bi nanowires we noticed a negative value of the thermopower within the experimental temperature range, ascribable to Bi n-type [Con14], and a monotonic decrease of its absolute value as the temperature decreases. In particular, the Seebeck coefficient detected at 300 K varies between -(61 ± 6) μV/K for (431 ± 29) nm, and -(30 ± 3) μV/K for wire diameter (58 ± 6) nm. Between room temperature and 30 K, the Seebeck coeffiicent decreases linearly to values within -(3 ± 2) μV/K, measured for (130 ± 10) nm, and -(0.4 ± 0.6) μV/K for (79 ± 8) nm wire diameter.

A monotonic decrease of the absolute value of the Seebeck coefficient was also measured in $Bi_{0.85}Sb_{0.15}$ and Sb nanowire arrays, presented in figure 3.7 (b) and (c), respectively. In contrast to Bi-based samples, the thermovoltage of Sb nanowires has positive values, caused by thermal diffusion of holes in the system instead of electrons, ascribable to Sb p-type [Bra72, Nab13].

The monotonic decreasing of the thermopower was measured in a similar temperature range for bulk Bi and Sb [Iss06]. An analog behavior was reported for individual Bi nanowires [Bou06], defining the thermovoltage as the entropy per electric charge, which must decrease to zero at 0 K.

Figure 3.7 (d) presents the evaluated Seebeck coefficient of Bi, $Bi_{0.85}Sb_{0.15}$ and Sb nanowire arrays at 300 K as a function of wire diameter. For all the three materials, the data reveal a non-monotonic behavior of the thermopower for all the materials as a function of the wire diameter.

For Bi nanowires (black squares), we can distinguish three different regimes: (i) for wire diameters above (130 ± 10 nm) (red background area) all experimental Seebeck coefficients are similar to the values reported for bulk Bi, namely ~ -60 μV/K [Yam02, Her02] independently on the wire diameter. (ii) With wire diameter decreasing from (130 ± 10 nm) to (58 ± 6 nm) (green area), the Seebeck coefficient of the nanowire arrays decreases monotonically. (iii) For nanowires with diameter smaller than ~ 60 nm, the absolute value of the Seebeck coefficient increases (blue background area).

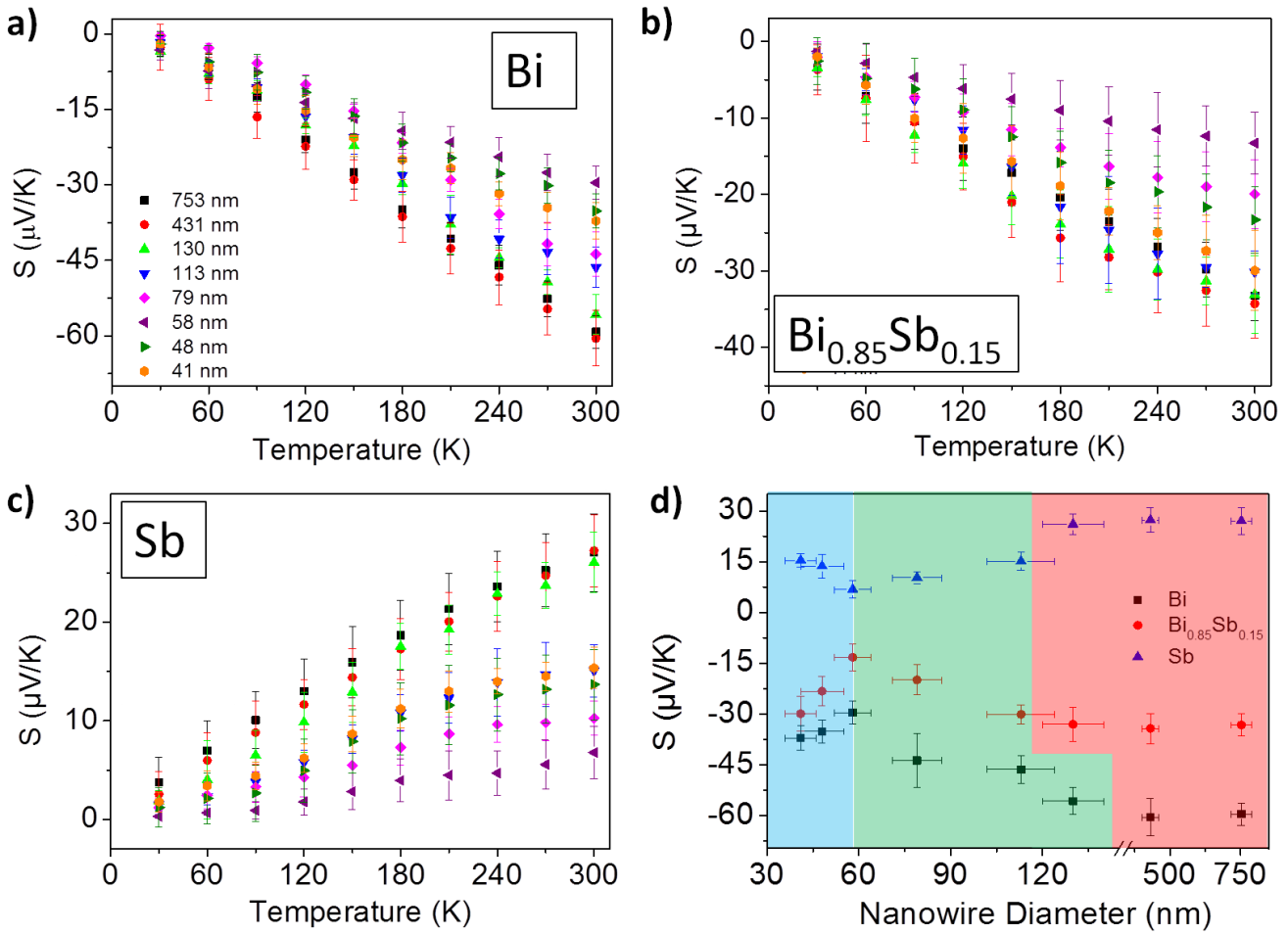


Figure 3.7: Seebeck coefficient of nanowire arrays with different wire diameters as a function of temperature. The wire diameters are: (753 ± 37) (black), (431 ± 29) (red), (130 ± 10) (light green), (113 ± 11) (blue), (79 ± 8) (magenta), (58 ± 6) (brown), (48 ± 7) (green) and (41 ± 5) (orange) nm, and the different wire composition: (a) Bi, (b) $Bi_{0.85}Sb_{0.15}$ and (c) Sb nanowire arrays. (d) Seebeck coefficient of nanowire arrays measured at 300 K as a function of the wire diameter for the different compositions: (black) Bi, (red) $Bi_{0.85}Sb_{0.15}$ and (blue) Sb.

We tentatively attribute the monotonic decreasing behavior in region (ii) to the opposite contributions of the bulk and surface states to the total thermopower of Bi nanowires. Since the discovery of the topological insulator nature in $Bi_{1-x}Sb_x$, research efforts are focused on studying the surface states properties of this alloy [Hsi08]. As a consequence of the higher surface-to-volume ratio of nanostructures, the influence of surface states on transport properties increases with decreasing the wire diameter [Kim14]. Previous measurements performed on both individual $Bi_2Te_3$ [Ham13] and ternary BiSbTe [Bäß13] nanowires as well as theoretical studies [Goo15] pointed out a monotonic reduction of the thermopower when decreasing wire diameter, due to the increasing contribution of the metal-like surface states to the transport properties.

In this regime, the Seebeck coefficient can be calculated using a two-channel model, considering the simultaneous contribution of bulk and surface states, as [Nol01]:

$$S = \frac{S_{BS}\sigma_{BS} + S_{SS}\sigma_{SS} * 4\left(\frac{L}{d} - \frac{L^2}{d^2}\right)}{\sigma_{BS} + \sigma_{SS} * 4\left(\frac{L}{d} - \frac{L^2}{d^2}\right)} \quad , \tag{3.4}$$

with $S$ and $\sigma$ being the Seebeck coefficient and electrical conductivity of the bulk states (*BS*) and surface states (*SS*), respectively, $L$ the thickness of the surface states layer and $d$ the diameter of the wires.

Figure 3.8 (a) presents the experimental (black) and estimated (blue) values of the Seebeck coefficient as a function of the wire diameter at 300 K for Bi nanowires. The data were calculated with equation 3.4 considering at room temperature a $S_{BS}$ = -63 µV/K [Has09], $\sigma_{BS} = 0.867 \cdot 10^6$ S/m [Cor10b] and assuming $L$ = 0.6 nm, corresponding to ~ 1.5 layer of atoms for Bi. In this case, the fit is optimized for a thermopower and electrical conductivity at room temperature of the surface states of $S_{SS}$ = 360 µV/K and $\sigma_{SS} = 1.11 \cdot 10^6$ S/m, respectively. Since the surface states possess metallic properties [Kim15, Kim14, Hub11], the electrical conductivity of the surface is expected to be higher than the bulk states of semimetal Bi. In addition, the value of the surface-state thermopower has a reverse sign (positive) compared to the Seebeck coefficient of the bulk states (negative). This would means that the transport properties of the surface states are due to holes and conversely, to electrons in the bulk states.

To better understand the influence of the different parameters on the values obtained by the two-channel model, we plotted various set of data using equation 3.4 and changing one value per time respect to the best fit values reported for figure 3.8 (a), namely $S_{BS}$ = -63 µV/K, $\sigma_{BS} = 0.867 \cdot 10^6$ S/m, $S_{SS}$ = 360 µV/K, $\sigma_{SS} = 1.11 \cdot 10^6$ S/m and $L$ = 0.6 nm. This study is reported in figure 3.8 (b).

First, we varied the $S_{BS}$ using two different values reported in literature for Bi bulk at room temperature, namely ~ -45 µV/K by [Lin02] and ~ -72 µV/K by [Nak11b]. However, the best value fits to our experimental data is obtained for $S_{BS}$ = -63 µV/K [Has09]. Subsequently, we modified $S_{SS}$ using nominal values of 600 µV/K and 100 µV/K, respectively. A fit value of 600 µV/K better follows the data. Lastly, we showed the influence of the thickness of the surface-state layer on the total thermopower, considering values of $L$ = 0.3 nm and 1.2 nm. The best fit was obtained with the thicker $L$.

Thus, considering higher values of $S_{SS}$ and $L$, the estimated data still fit quite accurately the experimental points. This underlines that the values estimated using equation 3.4 need to be considered within a certain range of magnitude.

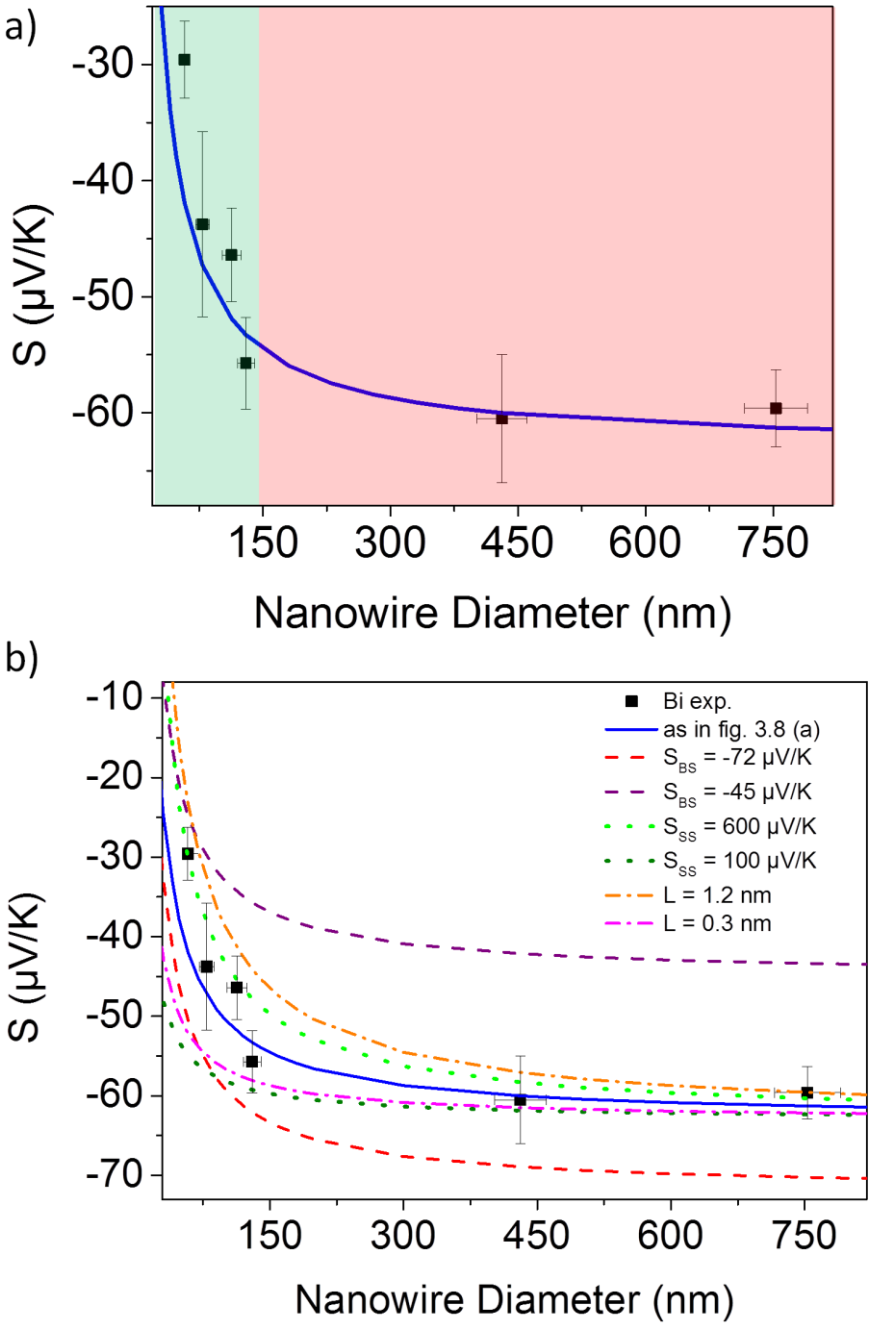


Figure 3.8: (a) Seebeck coefficient of Bi nanowire array measured (black squares) at 300 K as a function of the wire diameter and estimated Seebeck coefficient (blue line) from a two-channel model (equation 3.4) (b) Measured Seebeck coefficient (black squares) and thermopower calculations using eq. 3.4 considering $S_{BS}$ = -63 μV/K, $\sigma_{BS} = 0.867 \cdot 10^6$ S/m, $S_{SS}$ = 360 μV/K, $\sigma_{SS} = 1.11 \cdot 10^6$ S/m and $L$ = 0.6 nm and varying respectively: $S_{BS}$ = -72 μV/K (red dash line) and -45 μV/K (purple dash line), $S_{SS}$ = 600 μV/K (green dotted line) and 100 μV/K (dark green dotted line), and $L$ = 1.2 nm (orange dash-dot line) and 0.3 nm (magenta dash-dot line).

The increasing contribution of the surface states to the total thermopower can be explained also by calculating the charge carrier density of Bi nanowires. The carrier concentration ($n$) in the nanostructure from the evaluated Seebeck coefficients is estimated using the Mott relation [Mot71]:

$$n = \frac{1}{3\pi}\left(\frac{\pi^2 k_B^2 m^*}{\hbar^2 e}\frac{T}{S}\right)^{3/2} \quad , \tag{3.5}$$

where $k_B$ is the Boltzmann constant, $\hbar$ Planck´s constant, $e$ the electric charge, $m^*$ the charge effective mass, $S$ the thermopower and $T$ the temperature.

In recent experiments [Hub09] carried out on thin trigonal-oriented Bi nanowires, $m^*$ of both bulk and surface states was deduced independently as ~ 0.06 $m_e$ and ~ 0.3 $m_e$, respectively. Considering this $m^*$ for the bulk states, the charge carrier density at room temperature for bulk-like Bi nanowires (red area in figure 3.7 (d)) is ~ 3 x $10^{18}$ $cm^{-3}$, a value similar to $n$ detected in bulk Bi [Jai59].

For thinner nanowires (green area in figure 3.7 (d)) we expect a lower bulk charge carrier density due to the decrease of the band overlap of semimetal Bi [Dre03]. This influences strongly the transport properties of thin nanostructures. For such small diameters (region (iii)), the appearance of quantum size effects are discussed for Bi nanowires, since the nanowire diameter is comparable to the Fermi wavelength of the electrons in Bi [Cor10b], and the semimetal-to-semiconductor transition, creates a bandgap in the electronic structure [Lin00]. Both these effects lead theoretically to an enhancement of the absolute value of the thermopower [Her02]. Moreover, it was also reported that in thin nanostructures the metallic surface states can hybridize, creating a bandgap in their electronic structure, similar to a narrow-gap semiconductor [Tak12, Gha10]. Thus, also the surface states may contribute to enhance the total thermopower in small nanowires. In general, for nanowire diameter below 60 nm, the increase of the Seebeck coefficient is attributed to modifications of the electronic structure of both bulk and surface states of Bi nanowires and additional measurements with other experimental techniques are required to investigate this in more detail.

In general, the charge carriers of the surface states possess a specific wavelength ($\lambda_{SS}$) which, depending on its magnitude, interacts with the charge carrier of the bulk states. This characteristic was reported to define the effective spatial range of the surface states [Hub11]. Thus, we reconsidered equation 3.4 by approximating $L \sim \lambda_{SS}$.

If we estimate that for wire diameters below 58 nm the possible hybridization of the surface starts [Tak12, Gha10], we can consider $\lambda_{SS}$ ~ 29 nm. This $\lambda_{SS}$ values is similar to values reported by Huber et al. for Bi nanowires synthesized by melting pressure injection [Hub11].

In this case, the transport properties in the thinner wires are dominated by the surface-states charge carriers [Kim15], and $S_{SS}$ can be estimated equal to the value measured for Bi nanowires at ~ 58 nm, namely -29.6 μV/K. Thus, contrarily to the first considerations (see above), this assumption defines the carriers at the surface of the wire as electrons.

Figure 3.9 reports the new set of data calculated using equation 3.4, considering at room temperature $S_{SS}$ = -29.6 μV/K, $S_{BS}$ = -63 μV/K [Has09] and $\sigma_{BS} = 0.867 \cdot 10^6$ S/m [Cor10b]. The graph was developed varying $\lambda_{SS}$ and $\sigma_{SS}$ to understand the influence of these parameters on the estimated thermopower. In particular, we have decided to define $\sigma_{SS}$ as equal to $\sigma_{BS}$ and two times $\sigma_{BS}$. This two values were selected since in literature are reported estimation of both surface-state charge carrier density (~ 3 x $10^{18}$ $cm^{-3}$) [Kim15] and mobility (~ 2 $m^2$ $V^{-1}$ $sec^{-1}$) [Hub11] for 60 nm Bi nanowires, allowing to presume that $\sigma_{SS} \sim 1.1 \cdot 10^6$ S/m. This value lies inside the chosen range.

The expected data reported in figure 3.9, using $\lambda_{SS}$ = 29 nm and $\sigma_{SS} = 0.867 \cdot 10^6$ S/m (red line), interpolate the experimental points with similar accuracy as the fit in figure 3.8 (a). However, increasing $\sigma_{SS}$ (blue line) reduces the accuracy of the fit. Furthermore, we consider $\lambda_{SS}$ = 17 nm, value estimated by [Hub11] for other Bi nanowires, and obtain the best fit for a higher value of $\sigma_{SS}$. To fit the experimental data, we notice that considering higher values of $\sigma_{SS}$ requires lower $\lambda_{SS}$ and vice-versa.

In general, the calculations reported in figure 3.8 and 3.9 help us understanding quantitatively the complex interplay of the surface and bulk states. In the first case, the fit states that the surface states are made of holes, which supply opposite contribution to the total wire thermopower with respect to the electrons present in the bulk states. On the contrary, by replacing $L$ with $\lambda_{SS}$ in the two-channel model equation, we estimated that electrons are the carriers present at the wire surface. However, these carriers render the surface lower $S_{SS}$ and slightly higher $\sigma_{SS}$ than the electrons in semimetal bulk states. Thus, since surface dominates the transport properties in thin wires, the total Seebeck coefficient decreases until it achieves the value equal to $S_{SS}$.

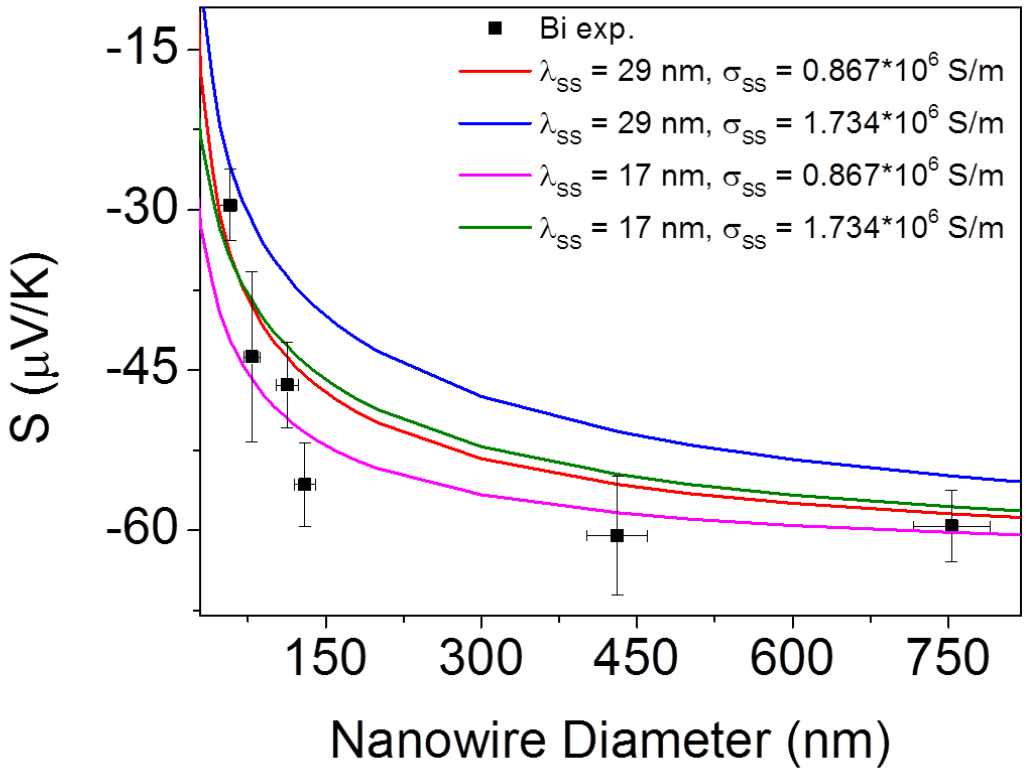


Figure 3.9: Seebeck coefficient of Bi nanowire array measured (black squares) at 300 K as a function of the wire diameter and estimated Seebeck coefficient from the two-channel model (equation 3.4) considering $S_{BS}$ = -63 μV/K, $\sigma_{BS} = 0.867 \cdot 10^6$ S/m, $S_{SS}$ = -29.6 μV/K and varying contemporary $\lambda_{SS}$ and $\sigma_{SS}$ as reported in the graph.

Figure 3.7 shows in addition, the Seebeck coefficient of nanowire arrays of $Bi_{0.85}Sb_{0.15}$ (red circles) and Sb (blue triangles). The Seebeck coefficient as a function of the wire diameter at room temperature for both materials exhibits a non-monotonic outline similar to Bi nanowire arrays. In fact, although a smaller critical diameter for the transition to the semiconductor phase for Sb nanowires was predicted [Her05], a decrease of its band overlap is expected beginning at around 60 nm [Her05] and the electron Fermi wavelength possesses a similar value as Bi [Zha06]. For $Bi_{0.85}Sb_{0.15}$ nanowires, we expect a similar long electron Fermi wavelength as in the case of Bi and Sb. However, theoretical studies pointed out a larger critical diameter of the semiconductor transition than in pure Bi nanowires [Rab01, Lin02]. In addition, the presence of surface states in $Bi_{1-x}Sb_x$ alloy and pure Sb with similar properties as pure Bi [Hsi08] allows us to discuss the thermopower behavior of the two materials with lowering wire diameter (figure 3.8) due to similar processes as considered for Bi nanowires.

Finally, the data in figure 3.7 (d) exhibits a lower Seebeck coefficient for $Bi_{0.85}Sb_{0.15}$ nanowires compared to pure Bi for all diameters. This was unexpected since Lin et al. reported higher values of

the thermopower of $Bi_{0.95}Sb_{0.05}$ nanowires compared to Bi [Tan14a, Lin02]. To better understand their behavior, we have measured the thermopower of a series of nanowire array presenting the same wire diameter but with different amount of Sb in the alloy. The results are presented in the next section.

The non-monotonic size dependence of the nanowires thermopower was studied at different temperatures. Figure 3.10 reports the thermopower of the three nanowire alloys as function of the wire diameter registered at 300 K (black squares), 150 K (red circles) and 60 K (blue triangles). We notice that for $Bi_{0.85}Sb_{0.15}$ (figure 3.10 (b)) and Sb (figure 3.10 (c)) nanowire arrays, the minimum of the deduced Seebeck coefficient is always measured for the (58 ± 6) nm diameter wires. However, for Bi nanowire arrays (figure 3.10 (a)) the thermopower minimum is observed for slightly larger values of wire diameter within a range between (58 ± 6) nm and (79 ± 8) nm at 150 and 60 K.

This slight shift is probably related to the higher sensibility of the band-structure parameters on the temperature [Vec74, Gal63], compared to the other alloys. In particular, semimetal Bi possesses a lower overlap between the valence and conduction band than Sb at room temperature [Zha06]. The overlap is reported to decrease when lowering the temperature [Gal63], inducing the semimetal-to-semiconductor transition in Bi at higher temperature than in Sb [Zha06].

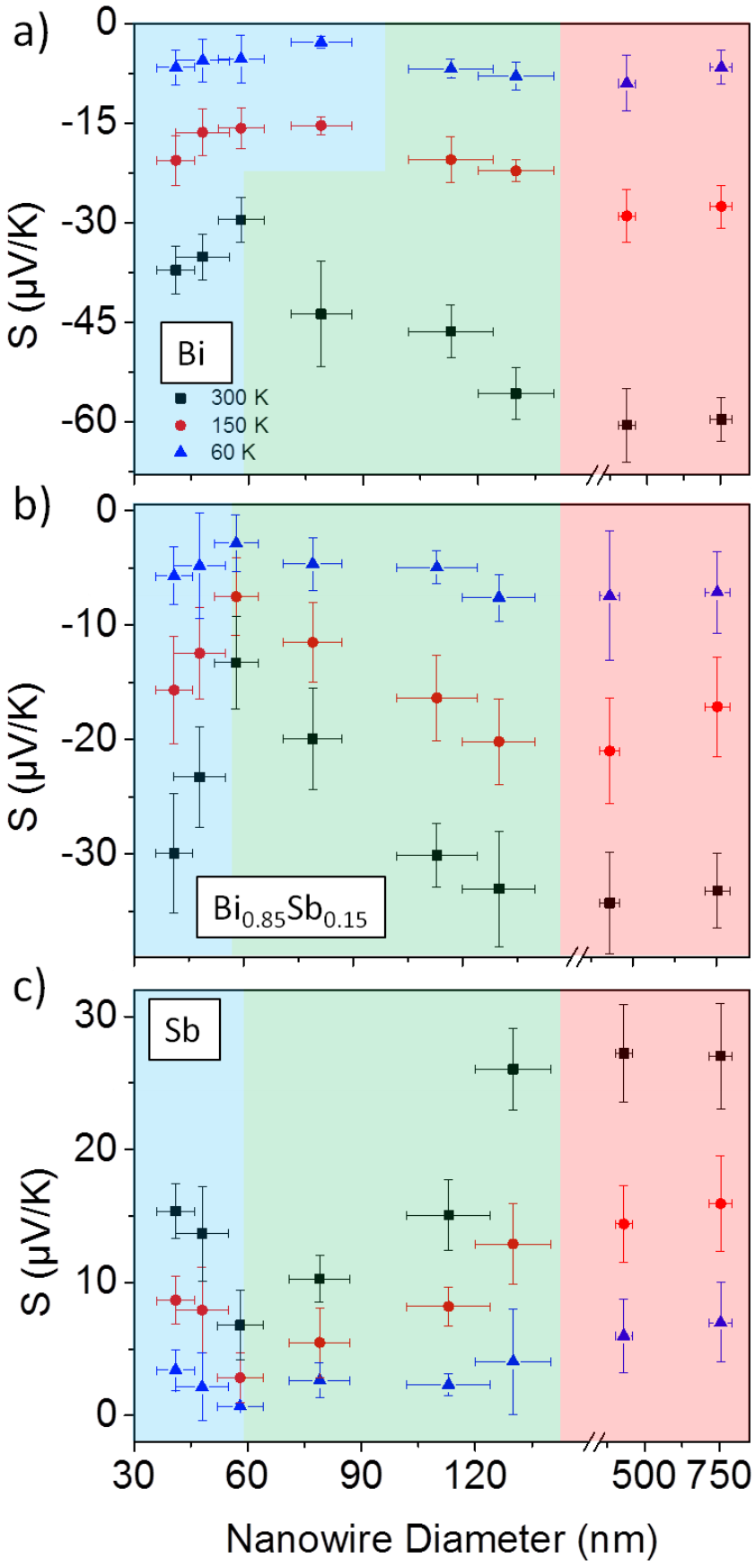


Figure 3.10: Seebeck coefficient of nanowire arrays with different wire diameters and compositions: (a) Bi, (b) $Bi_{0.85}Sb_{0.15}$ and (c) Sb, measured detected at different temperatures: (black squares) ~ 300 K, (red circles) ~ 150 K, (blue triangles) ~ 60 K.

## 3.4 Electrical Resistance vs. Temperature and Nanowire Diameter

Figure 3.11 (a) displays the non-monotonic behavior of the normalized resistance *R/R(300 K)* of Bi nanowire arrays between 300 and 20 K. The maximum in resistivity shifts to higher temperatures with decreasing wire diameter, from 90 K for wire size of (753 ± 37) nm to 180 K for wire size of (58 ± 6) nm. Similar behavior was detected before for the resistance of single-crystalline Bi nanowires and ascribed to the influence of finite quantum size effect [Cor06]. It was explained as a consequence of the influence of the nanowire size on the opposite contributions of the carrier charge density and mobility to the resistivity. In fact, in bulk Bi the increase of the charge mobility with decreasing temperature is larger than the decrease in the carrier density, resulting in a metal-like resistance behavior. The gain in mobility is limited for nanowires due to the limited diameter and grain size. Both limit the increase of the charge mean free path with decreasing temperature. Moreover, decreasing the wire size is reported to decrease the number of grain boundaries. This allows a stronger increase of the charge carrier mobility already for higher temperature than in bulk or in wires of larger diameter, shifting the maximum in the resistivity as presented in (figure 3.11).

Moreover, a transition from semimetal to semiconductor phase was predicted for Bi nanowires with diameter ~ 40 nm, depending on the wire orientation and temperature [Lin00]. This transition effect may influence the resistivity ratio of Bi nanowire arrays with wire size 48 ± 7 nm and 41 ± 5 nm, leading to an increase of the resistivity ratio compared to wires with larger diameters, as demonstrated in figure 3.11 (b).

Figure 3.11 (b) and (c) display the resistivity ratio measured for $Bi_{0.85}Sb_{0.15}$ and Sb nanowire arrays with different wire diameter. Sb nanowire arrays exhibit a metal-like behavior with decreasing resistivity ratio from value ~ 1.1 at 300 K to ~ 0.7 at 30 K for all considered wire diameters. These results are not unexpected, because Sb is a semimetal with a lower electron mean free path and a higher energy overlap [Zha06] compared to Bi. The detection of both finite size and transition from semimetal to semiconductor phase effects on the resistivity is only possible for lower wire diameters. On the other hand, the resistivity ratio of $Bi_{0.85}Sb_{0.15}$ nanowire arrays shows a smaller decrease within the temperature range compared to pure Sb array, varying from ~ 1.05 at 300 K to ~ 0.8 K at 30 K for wire diameter between ~ 753 and ~ 58 nm. Alloying Bi and Sb probably leads to a larger charge carrier mean free path than in pure Sb and thus, the gain of the carrier mobility by the nanowire boundaries is limited. Our experiments show that this effect is stronger in $Bi_{0.85}Sb_{0.15}$ nanowire arrays with smaller diameter, namely (48 ± 7) nm and (41 ± 5) nm, where the resistivity ratio is less dependent on temperature, varying from ~1.0 at 300 K to ~ 0.9 at 30 K.

However, theoretical predictions pointed out that for such composition and range of wire diameters, the nanowires are expected to consist of a semiconductor phase [Tan14a]. Based on our data, we cannot confirm this prediction. To better understand, we measured the resistance ratio on a series of nanowire arrays with same diameter, but slightly increasing the *c(Sb)* in the electrolyte used for the deposition. The results are presented in the next section.

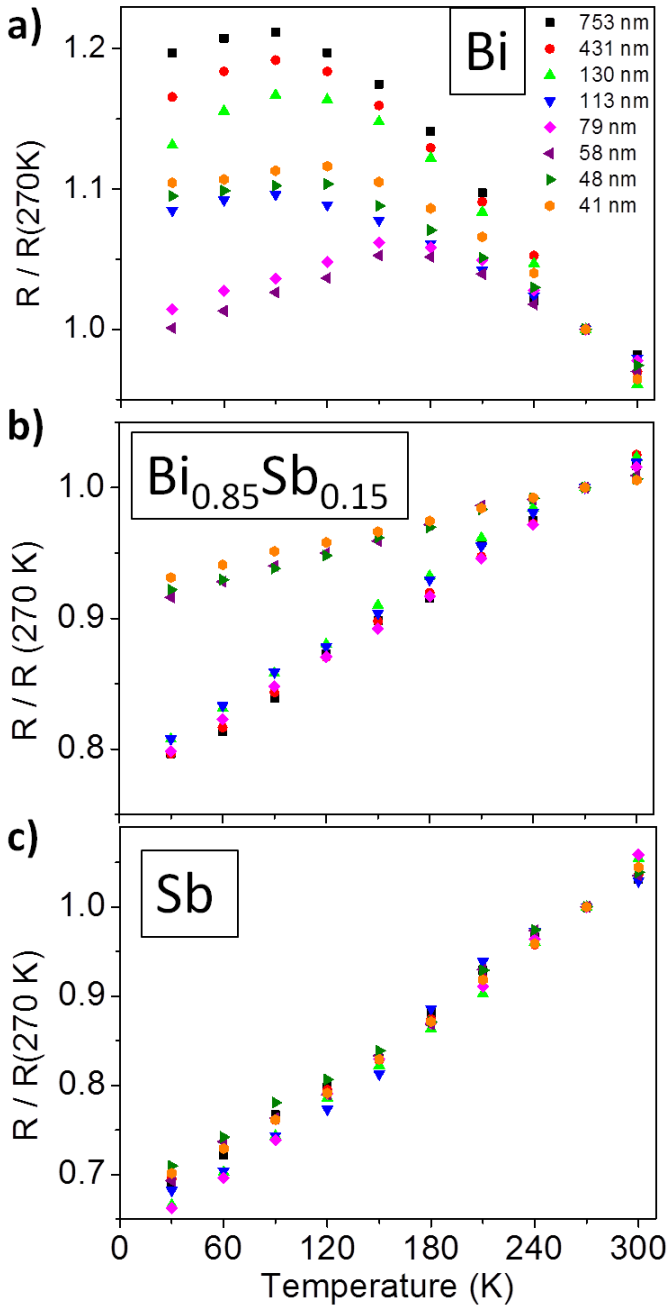


Figure 3.11: Electrical resistance ratio as a function of temperature of nanowire arrays of different composition: (a) Bi, (b) $Bi_{0.85}Sb_{0.15}$ and (c) Sb nanowire arrays. The wire diameters are: (753 ± 37) (black), (431 ± 29) (red), (130 ± 10) (light green), (113 ± 11) (blue), (79 ± 8) (magenta), (58 ± 6) (brown), (48 ± 7) (green) and (41 ± 5) (orange) nm.

## 3.5 Seebeck Coefficient and Resistance as a Function of Wire Composition

Being a semimetal material, bulk Bi thermoelectric performance is lower than that of semiconductor material, because of the opposite contributions from electrons and holes to the total Seebeck coefficient [Dre03, Her05].

As discussed earlier, one strategy to enhance the thermoelectric properties is to nanostructure Bi, which induces a transition to semiconductor phase below a critical wire diameter [Lin00]. Another option is to add Sb. It was reported that the addition of Sb to the Bi structure can transform the alloy into a semiconductor material for a narrow range of Sb concentrations [Jai59]. Moreover, it was predicted that $Bi_{1-x}Sb_x$ alloy nanowires possess a higher critical diameter than pure Bi nanowires, showing a semiconductor phase already in thicker nanowires [Rab01]. Previous experiments, carried out on nanowire arrays, reported higher values for the thermopower of $Bi_{0.95}Sb_{0.05}$ compared to pure Bi nanowires with same diameter. The presence of Sb is expected to reduce the Bi semimetallic band overlap [Tan14a, Lin02]. However, in our measurements, the measured $Bi_{0.85}Sb_{0.15}$ thermopower is lower compared to pure Bi for all diameters, as visible in fig. 3.7 (d).

To investigate this behavior, we measured the Seebeck coefficient of nanowire array with diameter of (79 ± 8) nm and with different amount of *x(Sb)*. The nanowires were electrodeposited using six different amounts of Sb ions (*c(Sb)*)in the electrolyte, namely: 0, 0.01, 0.015, 0.02, 0.03 and 0.1 mol/L. Their composition and orientation were investigated by X-ray diffraction, transmission and electron microscope, as reported in chapter 2 [Cas15a]. The nanowires exhibit a composition *x(Sb)* of 0.10, 0.12, 0.18 and 0.33, respectively, and a preferential orientation along {110} for low composition of Sb and {012} for *x(Sb)* = 0.33 and 1 [Cas15a].

The thermopower for all samples is displayed in figure 3.12 (a). All materials exhibit a monotonic decrease of the absolute value of the Seebeck coefficient as decreasing the temperature. Figure 3.12 (b) displays the measured Seebeck coefficient $Bi_{1-x}Sb_x$ alloy nanowires array as a function of *x(Sb)* at 300 K. The thermopower increases from a value of -(44 ± 4) μV/K for pure Bi to +(10 ± 2) μV/K for pure Sb. These measurements show that electrons dominate the transport in pure Bi and $Bi_{1-x}Sb_x$ ($x \leq 0.33$) alloy nanowires, leading to a negative value of the thermopower. On the contrary, pure Sb shows a higher hole contribution, exhibiting a positive Seebeck coefficient [Iss79]. However, no enhancement of the Seebeck coefficient due to alloying Bi and Sb was measured at room temperature. Similar behavior was measured by Yim et. Al for $Bi_{1-x}Sb_x$ alloy single crystals at room temperature with orientation parallel to the trigonal axis [Yim72]. On the other hand, the authors found an increase of the thermopower towards negative magnitude up to *x(Sb)* = 0.12 and then a decrease for further

addition of Sb for sample oriented perpendicular to the trigonal axis [Yim72]. This was also reported by the measurements of Dutta er al. on $Bi_{1-x}Sb_x$ alloy polycrystals at room temperature [Dut09].

Figure 3.13 displays the electrical resistance ratio measurements on different $Bi_{1-x}Sb_x$ alloy nanowires. The different data evolution can be explained by the shorter charge mean free path of Sb compared to Bi [Cor10b, Zha06]. In fact, pure Bi and $Bi_{0.90}Sb_{0.10}$ nanowires present a non-monotonic behavior of the resistance ratio as decreasing the temperature due to finite size effects on the charge-carrier mean free path, as described in the previous section [Cor06]. On the other hand, higher *x(Sb)* leads to a lower carrier mean free path, which makes their mobility being less influenced by the nanowire boundary, resulting in a metal-like behavior.

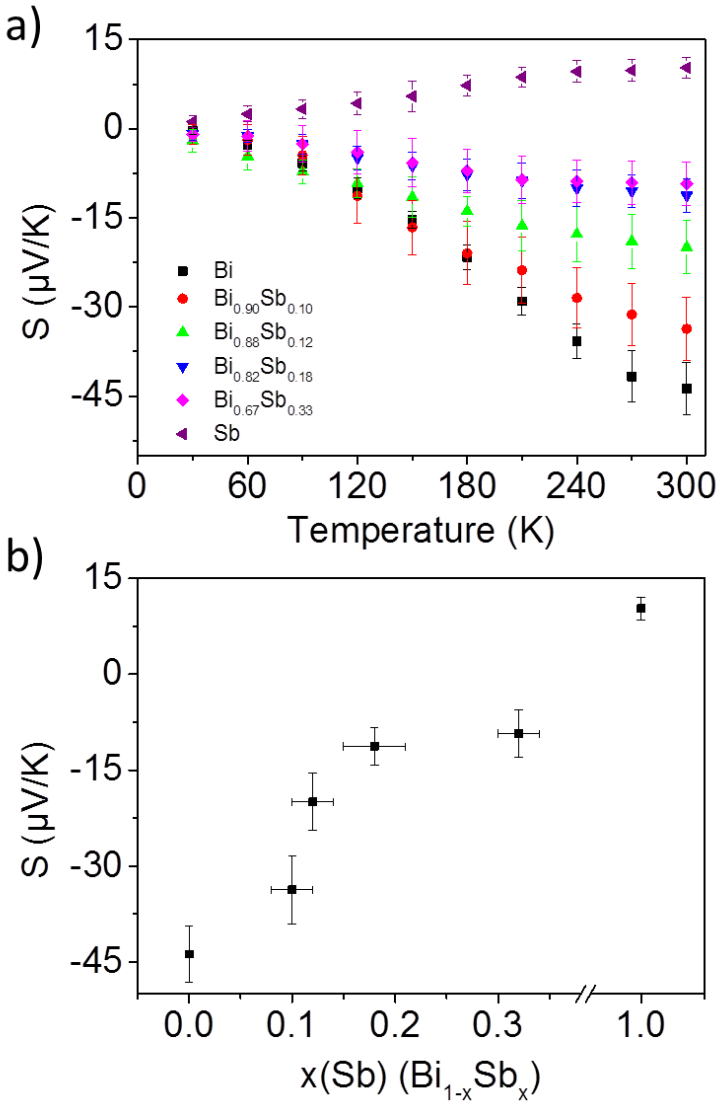


Figure 3.12: (a) Experimental Seebeck coefficient of $Bi_{1-x}Sb_x$ alloy nanowires arrays with $0 \leq x \leq 1$ for wires of diameter of (79 ± 8) nm. In the wires was detected an Sb content *x(Sb)* of: 0 (black), 0.01 (red), 0.012 (green), 0.018 (blue), 0.033 (magenta), 0.1 (violet) mol/L. (b) Seebeck coefficients detected at 300 K as different wire composition and as a function of *x(Sb)*.

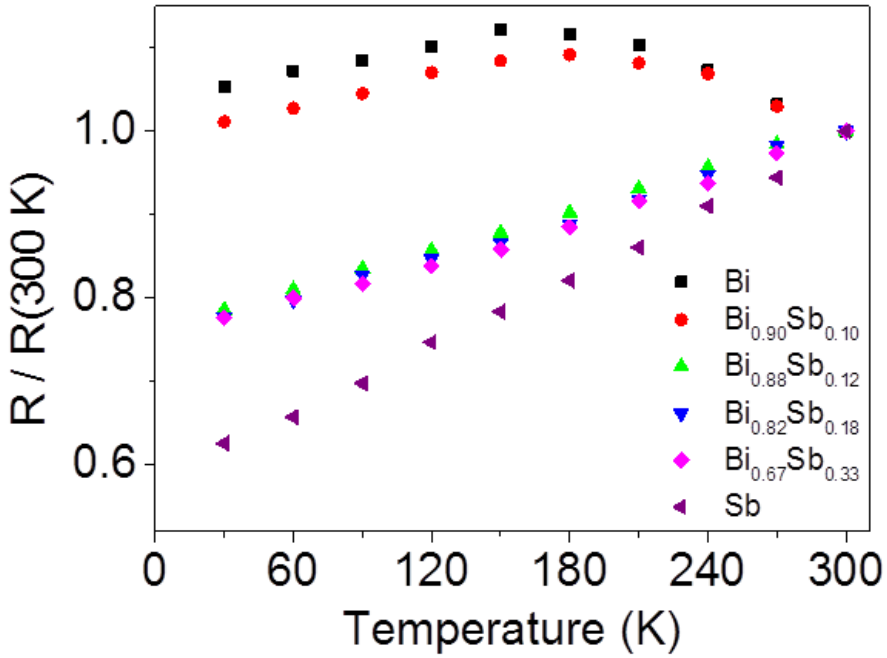


Figure 3.13: Electrical resistance ratio of $Bi_{1-x}Sb_x$ alloy nanowires array with $0 \leq x \leq 1$ as a function of different temperatures. In the wires was detected an Sb content *x(Sb)* of: 0 (black), 0.01 (red), 0.012 (green), 0.018 (blue), 0.033 (magenta), 0.1 (violet) mol/L.

## 3.6 Resume of Thermoelectric Characterization

Systematic and comprehensive measurements of the Seebeck coefficient and electrical resistance of $Bi_{1-x}Sb_x$ ($0 \leq x \leq 1$) nanowire arrays within the temperature range from 300 to 20 K and wire diameters between ~ 750 and ~ 40 allows us to better understand the thermoelectric properties of nanowires. A prerequisite of reliable measurements is the optimal thermal contacts between the sample and the setup.

The thermopower coefficient of all different $Bi_{1-x}Sb_x$ ($0 \leq x \leq 1$) nanowire arrays presents a linear decrease as lowering the temperature. The thermopower of Bi, $Bi_{0.85}Sb_{0.15}$ and Sb nanowire arrays exhibits a non-monotonic behavior lowering the wire diameter.

Theoretical calculations of Hicks & Dresselhaus [Hic93a, Hic93b] predicted a monotonic increase of the Seebeck coefficient of the material for small enough nanowire [Lin02]. This theory had not taken in consideration the presence of surface states on the materials, which has a major role in the explanations of our measurements. In fact, in wires thicker than ~ 130 nm, the surface states do not have any influences on the transport properties. This is supported by our measurements showing

thermopower values similar than for bulk. Lowering the wire diameter enhanced the opposite contribution of the surface states with respect to the bulk states to the total Seebeck coefficient, leading to an overall decrease of the thermopower of the nanostructure. Only in wires thinner than ~ 60 nm the thermopower raised possibly due to quantum effects on both the surface and bulk states of the nanowires, supporting the idea of superior thermoelectric properties in small nanostructures [Dre03].

The resistance of $Bi_{0.85}Sb_{0.15}$ and Sb nanowire arrays displays bulk-like behavior as a function of the temperature. However, a non-monotonic tendency was detected for pure Bi nanowires. We ascribed this to the appearance of finite-size effects, confirming longer mean free path of the Bi electron than in the other two materials.

Finally, adding Sb to the composition of Bi nanowires is expected to increase the thermopower of the nanostructures [Tan14a, Lin02]. However, the measurements did not show any gain of the total Seebeck coefficient due to alloying. This may be related to slightly differences detected in the wire orientation as a function of composition which are reported to have a large influence the electronic band structure of the nanowires [Tan14a].

# 4. Annealing Effect on Nanowire Composition and Stability

Metallic and semiconductor nanowires are expected to be key components of future nanoscale devices. Among other physical properties, the nanowires thermal stability is a crucial parameter to achieve reliable performance of a given nanowire-based module.

Previous experiments demonstrated that metallic nanowires exhibit, at temperatures far below the bulk melting point, the so-called Rayleigh instability, which causes the fragmentation of the cylindrical wires into chains of nanospheres under volume conservation [Zha05, Kar06, Kar07, Rau12, Dal12, Wan15, Vol15]. In particular, for Cu nanowires [Toi04] with diameters below 50 nm, the decay occurs at temperatures between 400-600°C, much lower than the bulk melting temperature (1085°C).

Bi and Sb bulk melting point temperatures are relatively low, 271 and 630°C, respectively. Thus, the possible effect of the Rayleigh instability on the nanowires stability should be studied to assess optimum conditions for the implementation in thermoelectric devices and systems, where the exposition to heat is a fundamental requirement. Another issue relevant for their application is surface oxidation, which leads to high contact resistances and unreliable electrical contacts with the nanostructure [Cro01]. This is the main reason why experimental data are still scarce, although specific chips have already been developed to perform measurements of the thermal and electrical conductivity on individual wires [Völ09, Wha12, Zho05].

The difficulties to electrically contact single $Bi_{1-x}Sb_x$ nanowires constitute a clear challenge for a reliable thermoelectrical characterization of the nanostructure. In particular, it is important to clarify if an oxide layer is formed before and/or after contacting or even during electrical measurements, favored by the increased temperatures produced by Joule heating and by exposure to atmosphere.

In this chapter, we present the study of the influence of the annealing process on the morphology and composition of Bi, $Bi_{0.85}Sb_{0.15}$ and Sb nanowires [Cas15b]. The nanostructures were analyzed by SEM, TEM and Raman spectroscopy before and after the annealing process. The stability of single nanowires was investigated for different annealing temperatures and times [Cas15b].

## 4.1 Experimental Details on Thermal Annealing

The Bi, $Bi_{0.85}Sb_{0.15}$ and Sb nanowires used in this experiment were fabricated following the steps described in chapter 2. The wires were electrochemical grown at room temperature in the channels of polycarbonate membranes (thick 30 μm and with ~ $7\times10^8$ $cm^{-2}$) by pulsed deposition applying $U_1$ = -250 mV vs. SCE for $t_1$ = 20ms and $U_2$ = -150 mV vs. SCE for $t_2$ = 100 ms [Cas15a]. The average diameter of the channels was (79 ± 8), (30 ± 4), and (18 ± 3) nm. Subsequently, the polymer matrix was dissolved, using dichloromethane, and the nanowires were transferred either onto Si wafers or, alternatively, onto Cu-lacey grids for SEM and TEM investigations. The dissolution process caused the nanowires to break into segments with lengths ranging from 1 to 20 μm.

For the annealing, the substrates (Si wafers and TEM grids) with the wires on top were introduced in a tube furnace (Carbolite HST 12/300) at room temperature. To ensure similar conditions during the annealing for the two different substrates, the TEM grids were first placed onto Si substrates and then inserted in the furnace. Then, the furnace was warmed up with a heating rate of 9°C/min. Once the set temperature was achieved, the temperature was kept constant for different annealing times $t_a$, varying between 30 min and 100 h. At the end of the process, the furnace was let cooling down. At room temperature the sample was removed from the furnace and analyzed. Moreover, to understand the influence of oxygen on the thermal stability, additional annealing experiments were performed in an evacuated chamber at a pressure of $10^{-6}$ mbar.

## 4.2 Annealing Effects on Nanowires Morphology

The SEM image of an as-prepared Bi nanowire with initial diameter ~ 30 nm is displayed in figure 4.1 (a). After the dissolution from the polycarbonate membrane and transfer onto the Si substrate, the wire exhibited a cylindrical shape and smooth surface. Figures 4.1 (b-d) display the SEM images of Bi nanowires after annealing in air at 100, 150, and 200°C for $t_a$ = 30 minutes, respectively. The morphology of the nanowires annealed at 100°C does not present any significant changes (figure 4.1 (b)). A slight increase of the surface roughness is visible for the wires annealed at 150°C (figure 4.1 (c)) and 200°C (figure 4.1 (d)). In both cases, the nanowires are still continuous, maintaining their cylindrical shape and structural stability

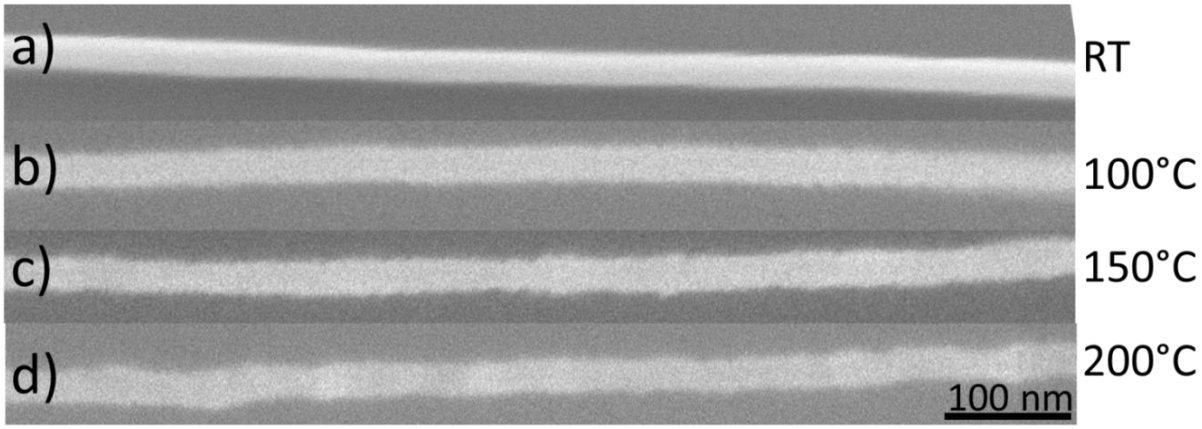


Figure 4.1: SEM images displaying sections of (a) cylindrical Bi nanowires on Si substrate with initial diameter (30 ± 4) nm, nanowires after annealing in air for 30 minutes at (b) 100, (c) 150, and (d) 200°C. The scale bar applies to all images.

This is in contrast to previous annealing experiments carried out on Cu [Toi04], Pt [Rau12] and Au [Kar06, Kar07] nanowires with diameter between ~ 30 and ~ 50 nm, which exhibited Rayleigh instabilities at temperatures far below the bulk melting point.

In a next step, we increased the annealing temperature to 250°C, a temperature very close to the Bi bulk melting point (271.5°C). Figure 4.2 presents SEM images of nanowires annealed at 250°C for (b) 2, (c) 20 and (d) 100 hours, showing evident changes of the morphology in all cases with respect to the as-prepared wire. After 20 hours annealing, the nanowires surface does not any longer exhibit a complete smooth profile. Instead, numerous protuberances are visible along the entire wire length. Both density and size of these protuberances increase significantly with increasing annealing time.

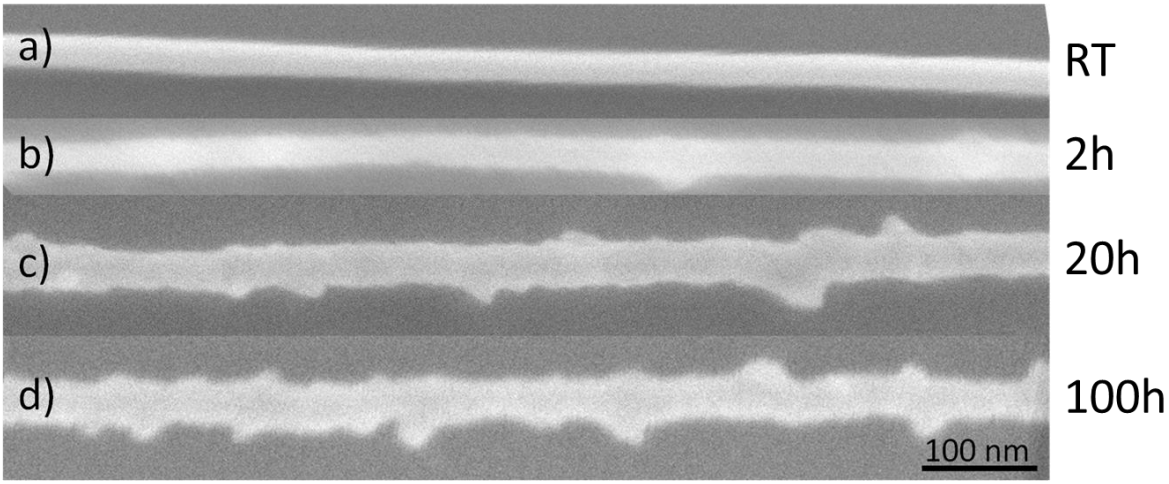


Figure 4.2: SEM images displaying sections of Bi nanowires on Si substrate with initial diameter (30 ± 4) nm (a) before and after annealing in air at 250°C for (a) 2 (b) 20 and (c) 100 hours. The scale bar applies to all images.

To check the possible influence of the substrate on the nanowire stability during annealing, Bi nanowires with initial diameter of ~ 30 nm were transferred onto thin carbon films of Cu-lacey TEM grids and then annealed at 250°C for the same annealing times, as the wires presented in figure 4.2. Similar increasing of the surface roughness as a function of the annealing time was detected (figure 4.3). This suggests that the changes in the nanowires surface do not depend on the substrate on which they are annealed. Note that contrast of SEM images on TEM grids is inverted, since in this case the STEM-in-SEM detector was used [Gol07].

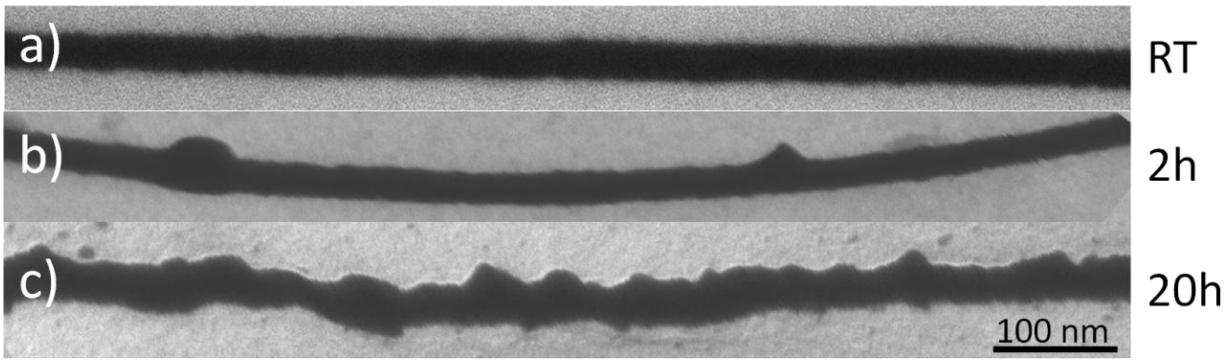


Figure 4.3: SEM images of Bi nanowires on Cu-lacey TEM grids with (a) initial diameter (30 ± 4) nm and after annealing in air at 250°C for (b) 2 and (c) 20 hours. The scale bar applies to all images.

The thermal stability of $Bi_{0.85}Sb_{0.15}$ nanowires was investigated by transferring wires with initial diameter ~ 30 nm onto TEM grids. The annealing was performed under the same conditions as for Bi nanowires reported in figure 4.3. In figure 4.4 (a) we can notice that the as-prepared $Bi_{0.85}Sb_{0.15}$ wires

possess a smooth surface. After 2 hours annealing at 250°C, few protuberances were detected on the nanostructures. Similar to Bi nanowires, the density of these instabilities increases as the annealing time proceeds to 20 hours, finally leading to a structure with a rough surface.

Although the bulk melting temperature of Sb (631°C) is significantly higher than that of bulk Bi, the morphological changes of $Bi_{0.85}Sb_{0.15}$ nanowires were comparable to those in Bi pure wires. Thus, the high percentage of Bi in the wires composition influences strongly the annealing behavior of the alloyed nanostructure.

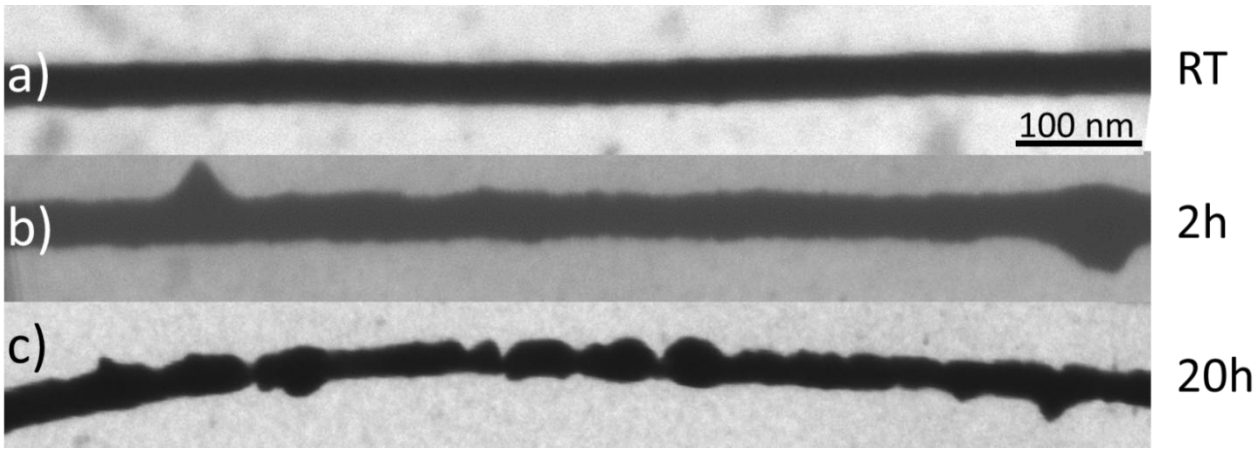


Figure 4.4: SEM images of $Bi_{0.85}Sb_{0.15}$ nanowires on TEM grids with (a) initial diameter (30 ± 4) nm and after annealing in air at 250°C for (b) 2 and (c) 20 hours. The scale bar applies to all images.

We also examined the thermal stability of pure Sb nanowires. The annealing experiments were performed at 600°C, near the melting point of bulk Sb (631°C). We used only Si substrate, since the TEM grids are not stable at such elevated temperatures. As for Bi and $Bi_{0.85}Sb_{0.15}$ wires, as-prepared Sb nanowires exhibit a cylindrical shape with a smooth surface (figure 4.5 (a)). After 2 hours annealing at 600°C, the surface shows a slightly increase in roughness. Even after 20 hours of annealing Sb nanowires do not display clear protuberances along the nanostructure, in contrast with results obtained for Bi and $Bi_{0.85}Sb_{0.15}$ nanowires. However, the morphological undulations presented along the nanowire axis are similar in this case to those appearing in the initials stage of the Rayleigh instability reported for Cu [Toi04] and Au [Kar06, Kar07] nanowires.

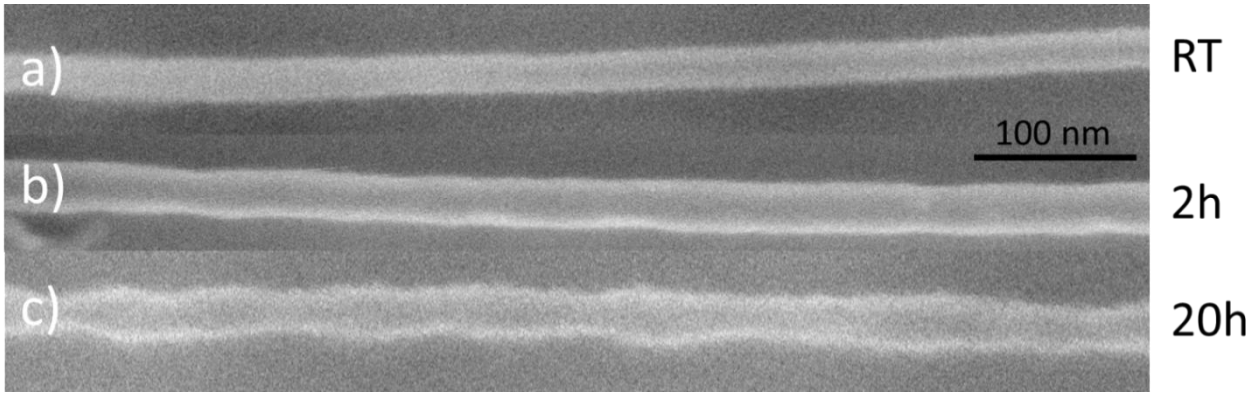


Figure 4.5: SEM images of Sb nanowires on Si substrate with (a) initial diameter (30 ± 4) nm and after annealing in air at 600°C for (b) 2 and (c) 20 hours. The scale bar applies to all images.

In summary, the thermal annealing of pure Bi, $Bi_{0.85}Sb_{0.15}$ and pure Sb nanowires with initial diameter of ~ 30 nm shows no evidence of Rayleigh instabilities. In fact, all the wires maintained their cylindrical continuous shape also after annealing at temperatures near the bulk melting temperature. After annealing at ~ 250°C for 30 minutes, Bi and $Bi_{0.85}Sb_{0.15}$ nanowires show similar protuberances, whose size and density increase with the annealing time. Pure Sb wires did not exhibit any morphological changes at ~ 600°C after 30 minutes of annealing, but small diameter undulations appear after 20 hours at 600°C.

To understand the possible influence of oxygen on the morphology evolution, Bi nanowires on a TEM grid were inserted in a furnace evacuated to a pressure of $10^{-6}$ mbar. The duration between the start of the evacuation and the start of the annealing was about 30 minutes. The annealing was performed at 250°C for 2 and 20 hours. As illustrated in figure 4.6, the wires do not exhibit any Rayleigh instability or protuberances, which on contrary are present in Bi wires annealed in air. Only a slight increase of the roughness appears for the annealed wires.

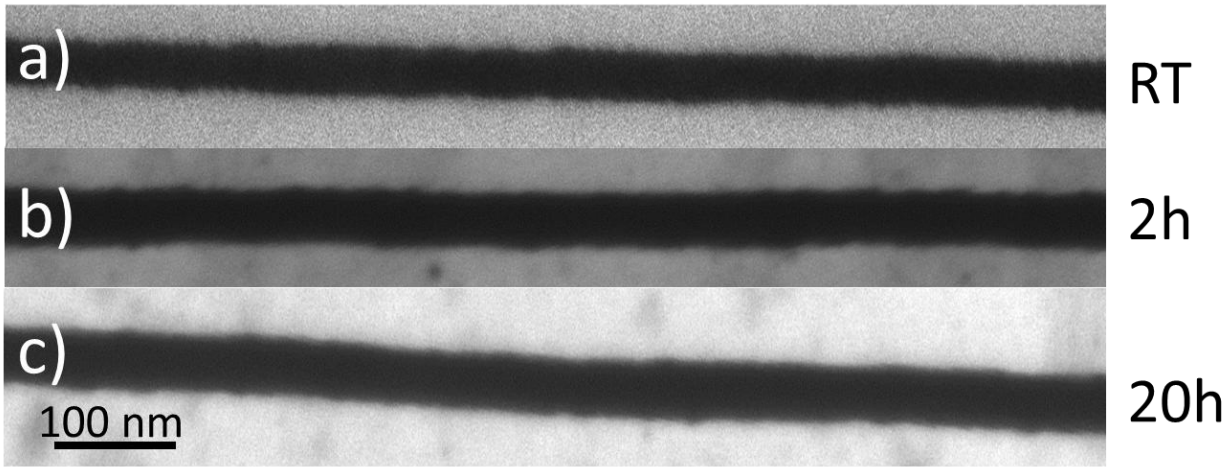


Figure 4.6: SEM images of Bi nanowires on Cu-lacey TEM grids with (a) initial diameter (30 ± 4) nm and after annealing in vacuum (P ~ $10^{-6}$ mbar) at 250°C for (b) 2 and (c) 20 hours. The scale bar applies to all images.

## 4.3 Annealing Effects depending on Wire Diameter

Previous experiments on the thermal behavior of both Pt [Rau12] and Cu [Toi04] nanowires gave clear evidence that the critical temperature of the Rayleigh instability depends on the wire diameter.

Thus, after the investigation of the thermal stability as a function of the composition at temperatures near the bulk melting point, we also studied annealing effects varying the diameter of our wires.

Figure 4.7 shows SEM images of Bi nanowires of diameter (a) ~ 18, (b) ~ 30 and (c) ~ 79 nm after annealing at 250°C for 20 hours. Qualitatively, similar formation of protuberances for all nanowire diameters is observed. The relative average size of these protuberances with respect to the initial wire diameter is in all cases ~ 0.4. However, the number of protuberances decreases with increasing wire diameter, leading to few but large protuberances in bigger wires.

Similar morphological changes, including the formation of protuberances, were previously reported by Kolmakov et al. for Sn nanowires annealed in air [Kol03]. There, the authors ascribed the origin of the formation of these protuberances to the unevenness of the oxide layer on the nanowire surface. In particular, they assumed that the highest oxidation rate was present along the grain boundaries and other crystal defects, forming the protuberances at those positions, while maintaining the integrity and shape of the wire.

The arguments of Kolmakov et al. [Kol03] do not explain the behavior of our Bi nanowires which show a smaller number of protuberances along the wire axis (figure 4.7) for thicker wires. As

described in chapter 2, we expect the number of grain boundaries and crystal defects in the nanowires to be either similar or to decrease with decreasing the wire diameter [Cor06c].

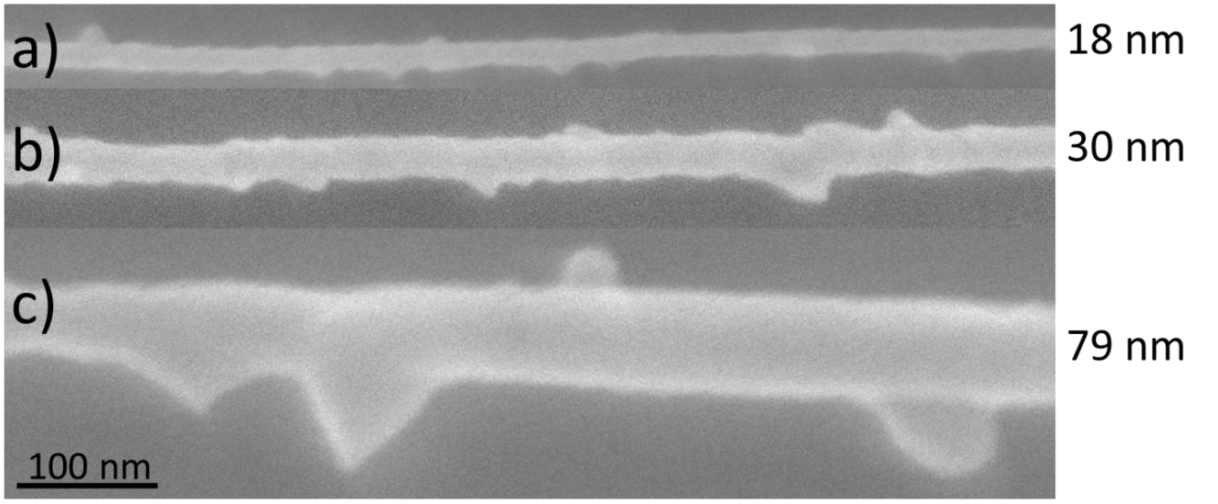


Figure 4.7: SEM images of Bi nanowires on Si substrate with initial diameters (a) (18 ± 3) nm, (b) (30 ± 4) nm and (c) (79 ± 8) nm annealed in air at 250°C for 20 hours. The scale bar applies for to images.

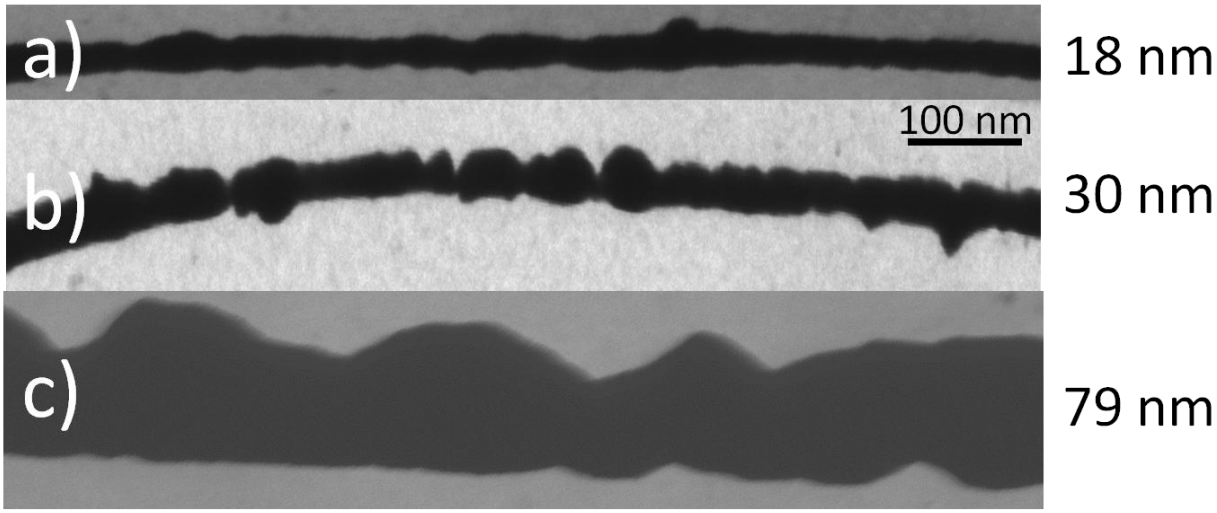


Figure 4.8: SEM images of $Bi_{0.85}Sb_{0.15}$ nanowires on TEM grids with initial diameters (a) (18 ± 3) nm, (b) (30 ± 4) nm and (c) (79 ± 8) nm annealed in air at 250°C for 20 hours. The scale bar applies to all images.

Figure 4.8 shows the thermal stability of $Bi_{0.85}Sb_{0.15}$ nanowires with different diameters annealed on TEM grids at 250°C for 20 hours. The initial diameters of the wires are the same as the Bi nanowires reported in figure 4.7: (a) ~ 18, (b) ~ 30 and (c) ~ 79 nm. The annealed wires presented bigger protuberances on the surface with increasing wire diameter, similar as the Bi nanowires. However, in this case the density of the instabilities along the wire axis is clearly higher than in Bi nanowires. The wires are in general rougher and lost their uniform cylindrical shape. The wire reported in figure 4.8 (b) exhibits pronounced constrictions between two protuberances. This behavior was not observed in Bi nanowires.

Figure 4.9 shows SEM images of Sb nanowires with average diameter, (a) ~ 18, (b) ~ 30 and (c) ~ 79 nm, after annealing in air at 600°C for 20 hours. The quality of the SEM images is low due to the increase amount of impurities present on the Si substrate after the annealing in air, impeding the focusing of the images. However, we clearly observed that the wire contour presents small undulations. This effect is similar for Sb wires of ~ 18 and ~ 30 nm in diameter, whereas Sb nanowires with ~ 79 nm diameter exhibit a rough surface with few small protuberances. The density and dimension of these instabilities are smaller than in Bi and $Bi_{0.85}Sb_{0.15}$ nanowires.

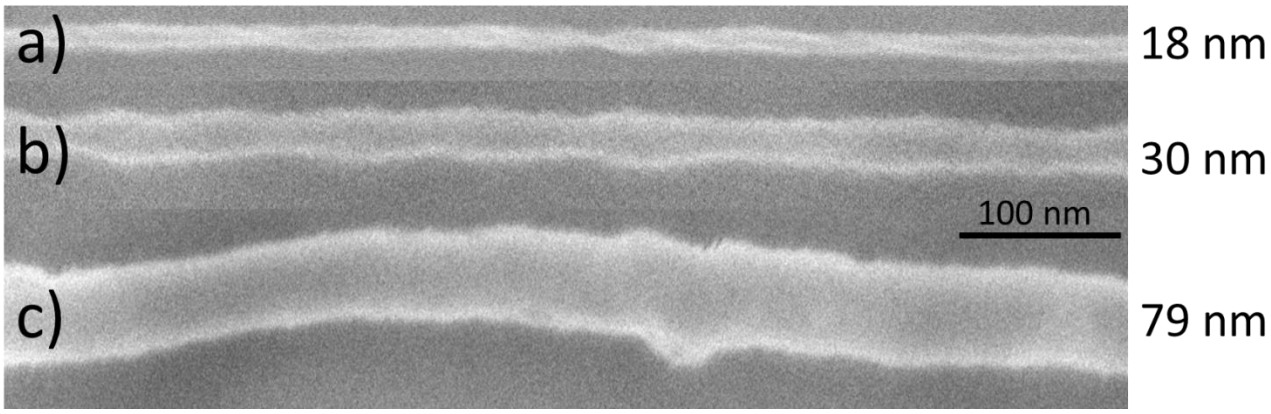


Figure 4.9: SEM images of Sb nanowires on Si substrate with initial diameters (a) (18 ± 3) nm, (b) (30 ± 4) nm and (c) (79 ± 8) nm annealed in air at 600°C for 20 hours. The scale bar applies to all images.

In summary, SEM investigations on annealed Bi, $Bi_{0.85}Sb_{0.15}$, and Sb nanowires with decreasing diameter have revealed no Rayleigh instability at temperatures near Bi and Sb bulk melting point, respectively. Instead, we observed the formation of protuberances in the case of Bi and $Bi_{0.85}Sb_{0.15}$ nanowires and diameter contour undulations for pure Sb wires. We attribute this behavior to the presence of an oxide layer and/or wire oxidation during the annealing in air. Since the melting point of bulk oxide metals is significantly higher than that of the corresponding semimetals (bulk

bismuth(III)oxide ($Bi_2O_3$) is 817°C and Bi bulk 271.5°C, antimony is 630°C and antimony(III)oxide ($Sb_2O_3$) 655°C). Oxidation explains the absence of Rayleigh instability at 250 and 600°C.

To confirm this explanation, we investigated the presence of an oxide phase on the wires by TEM combined with TEM-EDX and by Raman spectroscopy. The results are presented in the following section.

## 4.4 Annealing Effects on Nanowires Composition

The composition of Bi (diameter ~ 18 nm) and of $Bi_{0.85}Sb_{0.15}$ (diameter ~ 30 nm) nanowires before and after annealing in air was studied by TEM-EDX, in a JEM ARM 200CF operated at 400 keV at the Max Planck Institute for Intelligent systems (Stuttgart, Germany).

Figure 4.10 shows the TEM images (left) and the corresponding EDX line scans (right) measured across individual Bi nanowires (a) as-prepared and after annealing at 250°C for (b, c) 2 and (d) 20 hours. The blue background on the EDX line scans indicates the wire position.

The line scans provide information on the atomic percentage of Bi and oxygen (O) in the wires. The oxygen content across the nanowires is about 30% in the as-prepared nanowires (figure 4.10 (a)). In addition, the oxygen concentration increases up to ~ 60% towards the edges of the wire (edge of the blue area on the scan). This indicates that the oxidation process occurs already during the time between drop-casting and TEM analysis of the nanowire (in this case ~ 50 hours).

Figure 4.10 (b) presents the EDX line scan measured across a wire annealed for 2 hours at 250°C. The atomic composition is ~ 60% O and ~ 40% Bi. It remains almost constant across the nanostructure, indicating the complete and homogenous transformation of the Bi nanowire into $Bi_2O_3$ nanowire. In figure 4.10 (c) the line scan was performed on a protuberance, resulting in the same composition ($Bi_2O_3$). Figure 4.10 (d) presents the line scan across a wire annealed for 20 hours at 250°C, confirming that the annealed nanowires are fully oxidized to $Bi_2O_3$. The composition is maintained independently of the annealing time.

Figure 4.11 reports the TEM images (left) and the corresponding results of the line scan EDX measurements performed on $Bi_{0.85}Sb_{0.15}$ wires with initial diameter of ~ 30 nm before and after the annealing process. The line scan presents the atomic percentage of Bi, Sb and O recorded across the nanostructures. As in the case of Bi, the as-prepared alloy nanowires (figure 4.11 (a)) present already a high percentage of O (~ 40%), confirming that the oxidation process started even before the annealing. In this case, the wires were analyzed 25 hours after the membrane dissolution. During this time, the samples were exposed to air. Figure 4.11 (b) and (c) presents the measurements on wires annealed at 250 °C for 2 and 20 hours, respectively. Compared to the as-prepared nanowires, the atomic

percentage of Bi and Sb decreased and the O percentage reached a value of ~ 70%, confirming that, as in the case of pure Bi nanowires, the $Bi_{0.85}Sb_{0.15}$ nanowires are also strongly oxidized during annealing. The composition of a protuberance (figure 4.11 (d)) shows a higher percentage of Bi with respect to the other part of the annealed wire (figure 4.11 (c)). Moreover, for all analyzed wires, we noticed a small increase of the Sb percentage accompanied by a decrease of Bi towards the wire surface. This is an indication of a thin Sb oxide shell on the wire surface.

To investigate deeper the probable presence of a Sb-rich shell on the edge of the nanostructure and the precise composition of the analyzed nanowire, the TEM-EDX line scans of figure 4.11 were recalculated only taking in account Bi and Sb signals (figure 4.12). The as-prepared $Bi_{0.85}Sb_{0.15}$ nanowire line scan in figure 4.12 (a) exhibits a Bi-Sb ratio of 70% to 30% on the left edge, in the central area of the wire the average ratio is 86% to 14%, decreasing on the right edge to 60% to 40%. The higher concentration of Sb with respect to Bi on the edges is an indication of a possible Sb-rich shell on the wire surface. The average composition in the central area is similar to the concentration of Bi and Sb in the electrolyte. After 2 hours (figure 4.12 (b)) and 20 hours (figure 4.12 (c)) of annealing, both analyzed $Bi_{0.85}Sb_{0.15}$ nanowires display both on the edges a Bi-Sb ratio of 60%-40% (b)), while in the central part the average composition is 88%-12%, confirming a higher relative contents of Sb on the nanostructure edges. Although on the protuberance (figure 4.12 (d)) the line scan reveals in the central part an amount of Bi ~ 94%, an increase of Sb is still visible on the right edge of the nanostructure.

The nanowire composition after annealing was also investigated performing a TEM-EDX line scan along the nanowire axis showing the atomic percentage of Bi, Sb and O in the center of the nanostructures (figure 4.13). Taking into account the uncertaintes, the oxygen content varies along the nanostructure between ~ 65% and ~ 76%. The high percentage of oxygen indicates that the wire is completed oxidized. The same line scan was used to deduce the atomic percentage of Bi and Sb and the results are reported in figure 4.13 (b). The plot shows the Bi content varying from 93% to 78% along the wire axis, with an average value (~ 88%), slightly higher than the concentration used in the electrolyte (~85%).

The TEM-EDX measurements demonstrate that Bi and $Bi_{0.85}Sb_{0.15}$ nanowires are complete oxidized during annealing in air at 250°C for 2 and 20 hours. The as-prepared wires show that the oxidation process occurs already during the time between the wire release from the polymer matrix and the TEM analysis. However, since the waiting time between the wire release and the subsequent TEM analysis was about 50 hours (Bi) and 25 hours ($Bi_{0.85}Sb_{0.15}$), this makes difficult to conclude at which stage the oxide layer was formed. For this reason, we performed additional Raman spectroscopy on nanowires only few minutes after the membrane dissolution. The results are explained in the follow section.

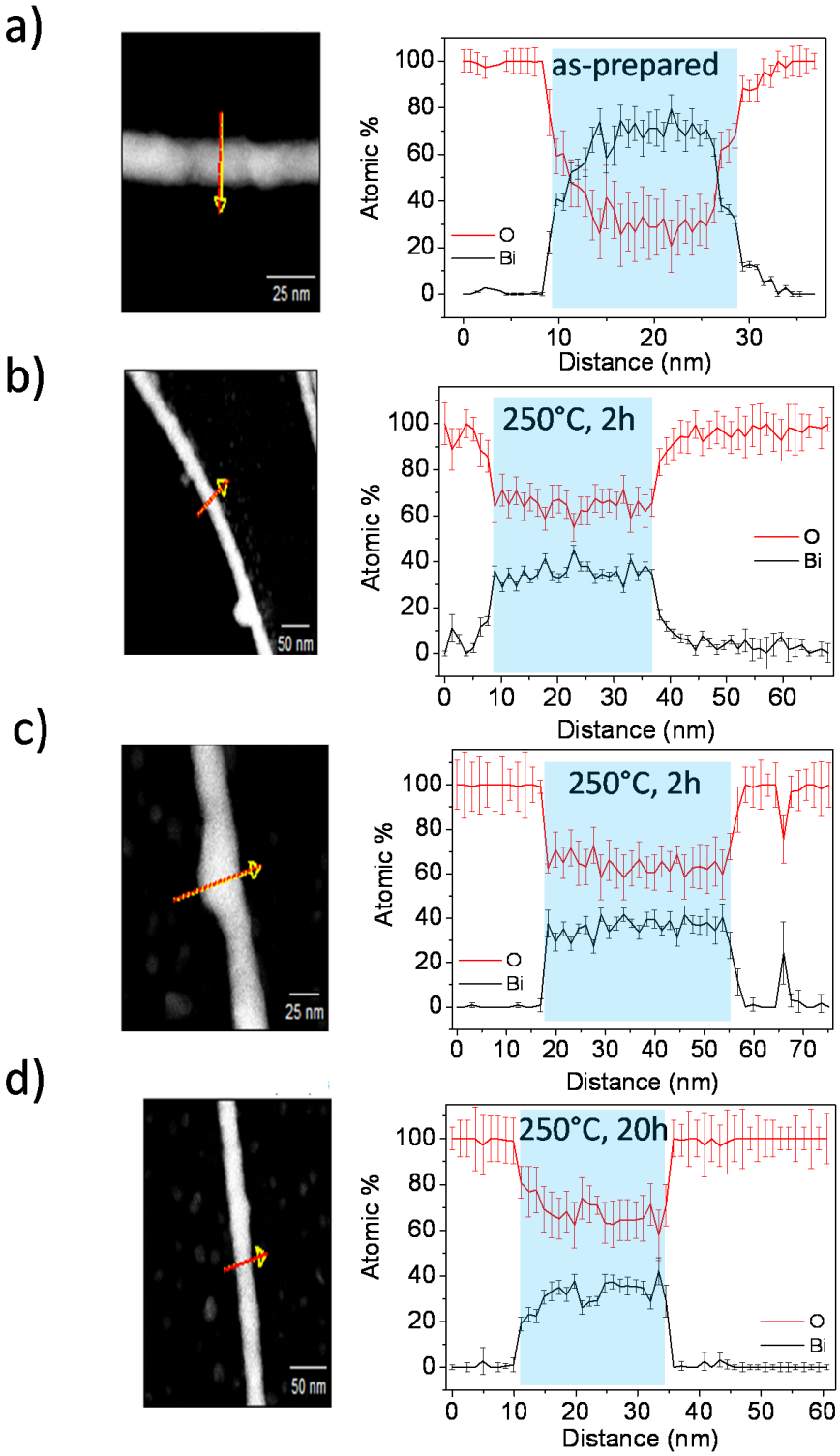


Figure 4.10: TEM images (left) of Bi nanowires with initial diameter (18 ± 3) nm drop-casted on TEM grids (a) as-prepared and after annealing in air at 250°C for (b,c) 2 and (d) 20 hours and the corresponding TEM-EDX line scans (right) measured across the wire diameter (red-yellow arrow), displaying the Bi and O atomic % content. The blue background areas on the scan represent the position of the wire.

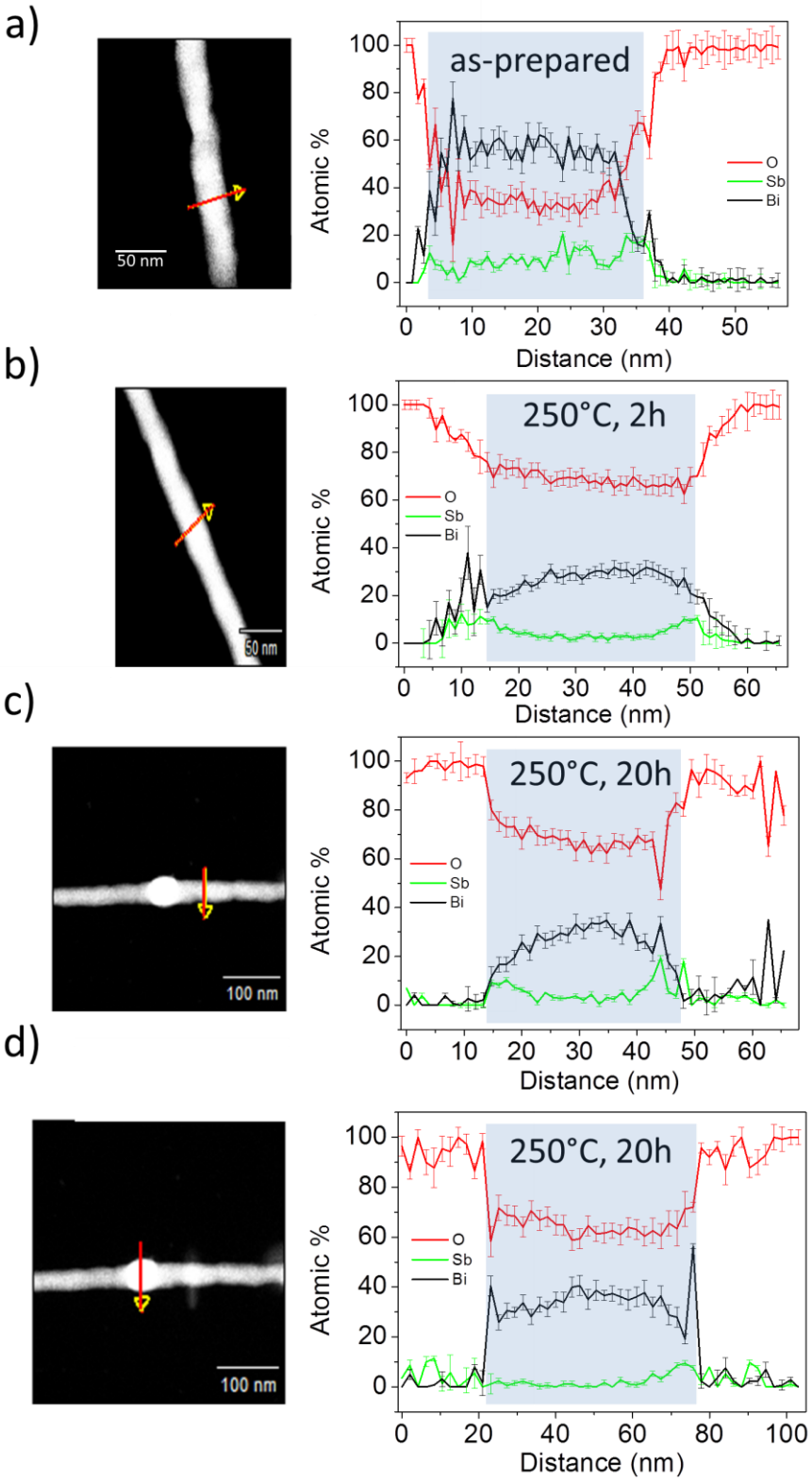


Figure 4.11: TEM images (left) of $Bi_{0.85}Sb_{0.15}$ nanowires with initial diameter of (30 ± 4) nm drop-casted on TEM grids (a) as-prepared, after annealing in air at 250°C for (b) 2 and (c, d) 20 hours and the corresponding TEM-EDX line scans (right) measured across the wires (red-yellow arrow), displaying the Bi, Sb and O atomic % content. The blue background area on the scan represents the experimental points ascribed to the nanostructure.

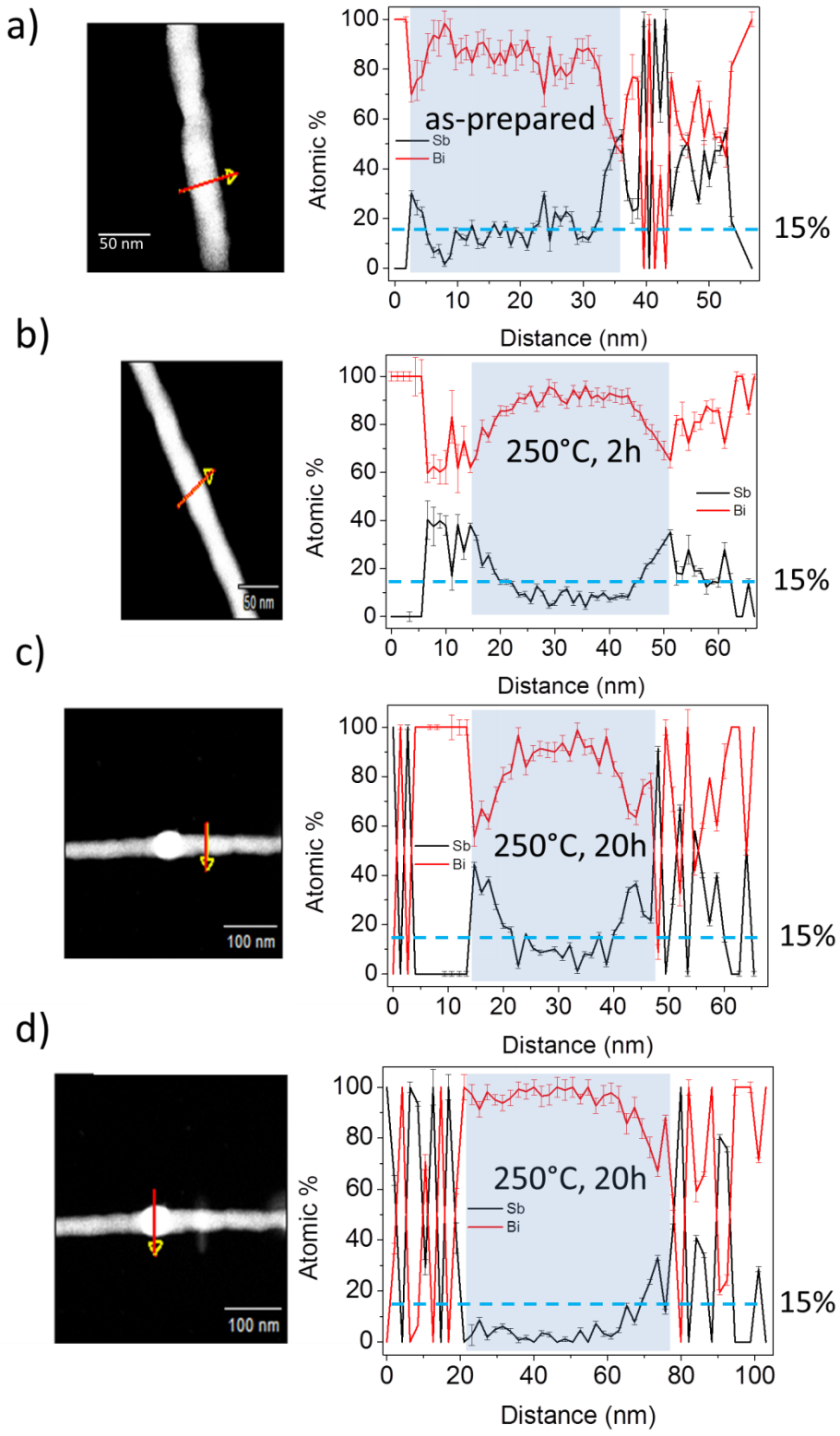


Figure 4.12: TEM images (left) of $Bi_{0.85}Sb_{0.15}$ nanowires with initial diameter of (30 ± 4) nm drop-casted on TEM grids (a) as-prepared, after annealing in air at 250°C for (b) 2 and (c,d) 20 hours and the corresponding TEM-EDX line scans (right) measured across the wires (red-yellow arrow), displaying only Bi and Sb atomic % content. The blue background areas on the scans represent the experimental points ascribed to the nanostructure, the blue dashed line is the nominal composition of Sb 15%.

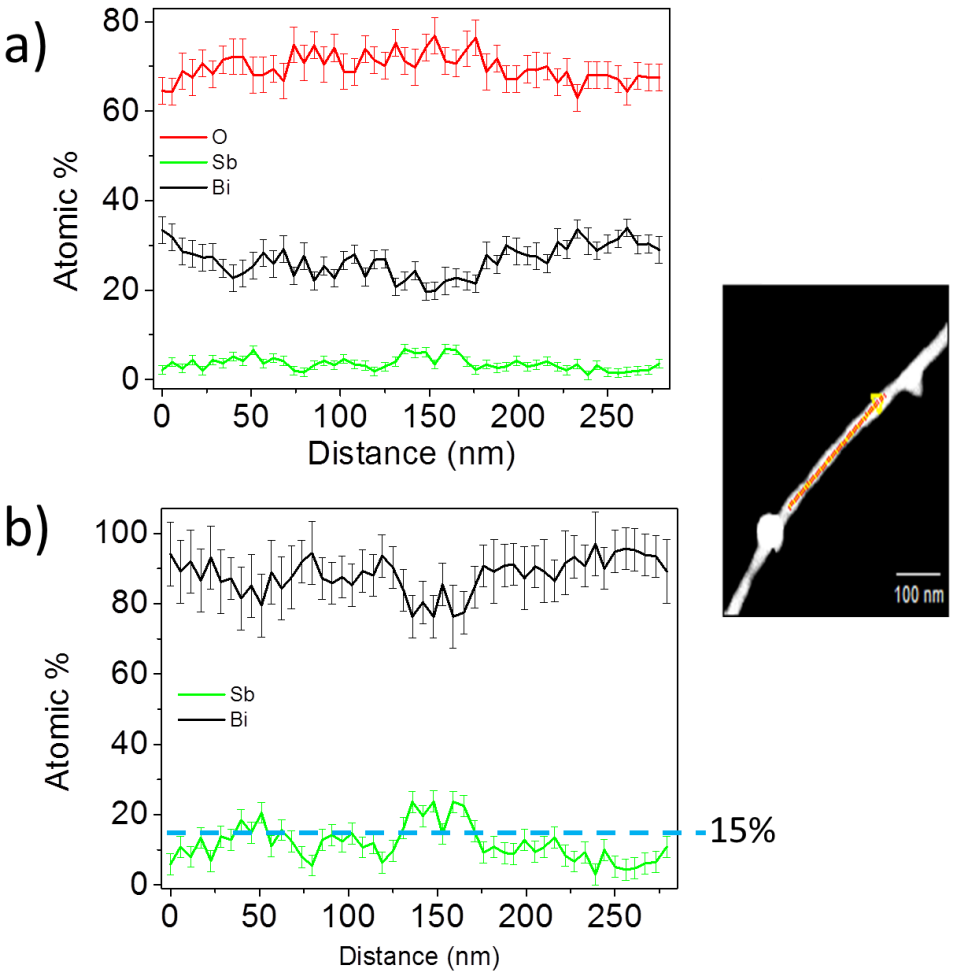


Figure 4.13: TEM images (right) of $Bi_{0.85}Sb_{0.15}$ nanowires with initial diameter of (30 ± 4) nm after annealing in air at 250°C for 2 hours and the corresponding TEM-EDX line scans (red-yellow arrow) along the wire axis (left) considering the (a) Bi, Sb and O , and (b) only Bi and Sb atomic % content. The blue dashed line indicates the nominal composition of Sb 15%.

## 4.5 Raman Spectroscopy Measurements on Nanowires

Raman spectroscopy is a powerful in-situ and non-destructive technique to probe the local atomic arrangements and vibrations of a given materials [Cho09, Cao07]. Raman spectroscopy was performed on Bi, $Bi_{0.85}Sb_{0.15}$ and Sb nanowires with diameter of ~ 79 nm using a commercial Horiba Jobin Yvon LabRam HR800 system with He-Ne laser of wavelength $\lambda = 632.82$ nm and power P = 0.96 mW. This wavelength is suitable to analyze both the semimetal and oxide phase of bismuth [Don09, Wan12]. The sample exposition time was 30 sec in all cases. Laser power and sample exposition times were kept low to avoid heating of the wires.

To understand the possible presence of oxide layers on the nanostructure before the annealing process, the nanowires were drop casted onto Si wafers and Raman spectra were recorded few minutes after the nanowires had been released from the polymer matrix. Thus, the analyzed samples represent the nanowires in the same condition as when they are inserted in the tube furnace for the annealing.

Figure 4.14 shows the Raman spectrum of the as-prepared Bi nanowires (red). The spectrum exhibits five different peaks ascribed to: (i) the $A_{1g}$ first order vibration mode of Bi atoms (98 $cm^{-1}$) [Tre09, Lan75], (ii) the $B_g$ displacement mode of both Bi and O atoms in α-$Bi_2O_3$ phase (108 $cm^{-1}$) [Nar94], (iii) and (iv) displacements in the $A_g$ mode of α-$Bi_2O_3$ (184 $cm^{-1}$ and 228 $cm^{-1}$) [Den97, Kuz96], and (v) silicon substrate (304 $cm^{-1}$) [Yan08]. This latter peak was used to normalize the spectra of the different nanowire.

As expected, the Bi peak at 98 $cm^{-1}$ is the highest for Bi nanowires right after the membrane dissolution. However, the detected peaks, assigned to α-$Bi_2O_3$ vibrations atoms, indicate that the oxidation process in the nanostructure starts after the PC dissolution, most probably at the nanowire surface as indicated by the TEM measurements. In particular, $Bi_2O_3$ has four different polymorphism, namely α, β, γ and δ phase [In11]. However, the α-phase is the only thermodynamically stable at room temperature [Sam99, Har79]. This result reveals that the semimetal nanowire presents already a small contribution of the α-phase of Bi oxide even before the annealing process.

In order to simulate conditions under which wires would operate during normal device usage, we annealed Bi wires in air at 100 °C for 30 days (i.e. 720 h). The spectrum (figure 4.14 (green)) displays a band at 98 $cm^{-1}$ ascribed to the vibration of Bi atoms in the rhombohedral structure [Tre09, Lan75]. This peak remains the strongest band, but peaks ascribed to the oxide phase are clearly visible at 108 $cm^{-1}$ (same as detected in the as-prepared nanowires), 144 $cm^{-1}$ ($B_g$ mode of α-$Bi_2O_3$) [Nar94], 184 $cm^{-1}$ and 228 $cm^{-1}$ ($B_u$ mode of α-$Bi_2O_3$)[Den97, Nar94]. Compared to the as-prepared nanowires, the annealed nanostructures present a larger presence of α-$Bi_2O_3$. Finally, Raman spectrum of Bi nanowire annealed at 250°C for 2 hours (blue spectrum in figure 4.14) is dominated by the band at 144 $cm^{-1}$. There is no band visible at 98 $cm^{-1}$ is not visible, indicating that the Bi nanowires are completely oxidized after annealing at 250°C for 2 hours, in full agreement with the TEM-EDX composition measurements presented in figure 4.10.

We noticed that only few Bi oxide bands are detected and that they exhibit very low intensities compared to other Raman measurements carried on Bi oxide wires of similar diameter [In11]. Thus, we additionally analyzed ~ 10 µm large Bi caps grown on top of our Bi nanowires. The caps were exposed to air for longer than 1 year (i.e. 9600 h) at room temperature. Their Raman spectrum (magenta in figure 4.14) confirms the position of the bands ascribed to the vibration of Bi atoms at 98 $cm^{-1}$ [Tre09, Lan75], and to the Bi alpha oxide phase at 108, 144, 184 and at 204 $cm^{-1}$ [Den97, Kuz96, Nar94], as well as the absence of additional $Bi_2O_3$ bands for this material up to 700 $cm^{-1}$. The absence of the peak at 304 $cm^{-1}$ confirms that we correctly assigned the band to Si (the laser spot is smaller than the cap size, thus excluding a signal from the Si substrate).

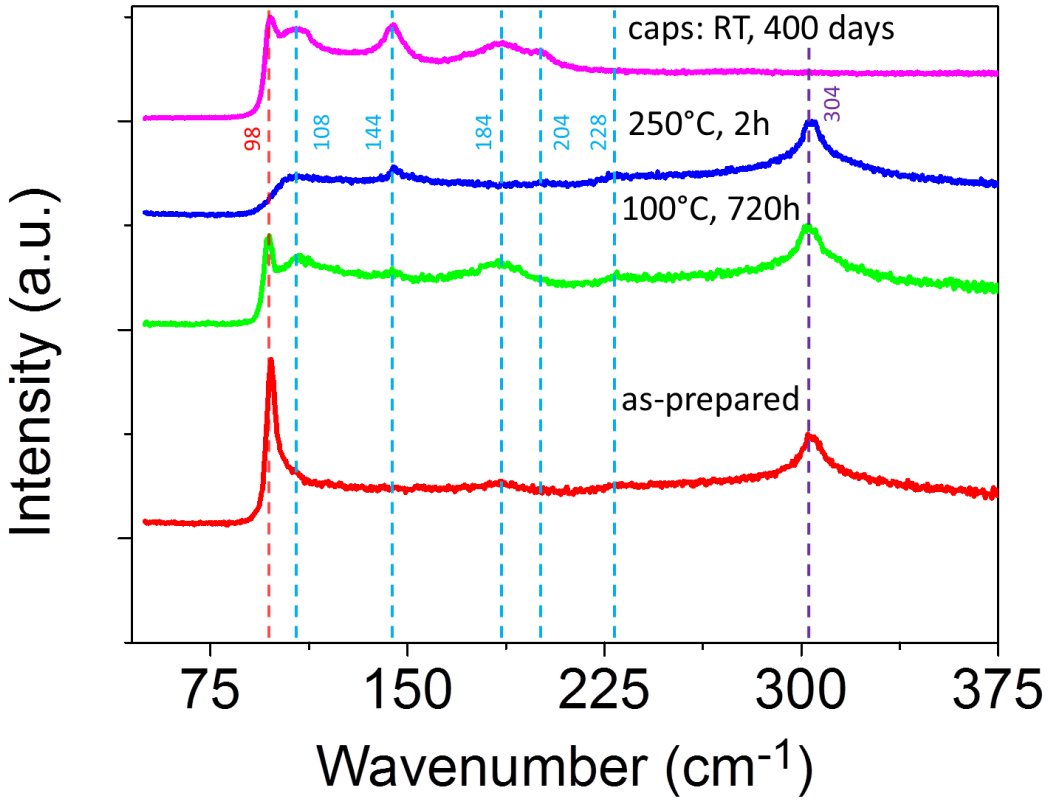


Figure 4.14: Raman spectra of Bi nanowires with diameter ~79 nm on Si substrate: (red plot) as-prepared, (green plot) after annealing at 100°C for 720 hours and (blue plot) after annealing at 250°C for 2 hours. The vertical dashed lines indicate the Raman bands assigned to Bi (red at 98 $cm^{-1}$), Bi and O atoms in α-$Bi_2O_3$ phase (light blue, at 108, 144, 184 and 228 $cm^{-1}$) and Si atoms (violet at 304 $cm^{-1}$).

Raman spectroscopy was also performed on $Bi_{0.85}Sb_{0.15}$ and pure Sb nanowires. The spectra, normalized to the Si peak at 304 $cm^{-1}$, are reported in figure 4.15. Before the annealing (magenta plot) the spectrum of Sb nanowires displays two peaks which are assigned to the displacements of Sb atoms in the $E_g$ mode (at 114 $cm^{-1}$) and in the $A_g$ mode, (150 $cm^{-1}$) [Deg07, Ban86].

Also a small band was detected at 189 $cm^{-1}$ that is ascribed to the presence of a small amount of $Sb_2O_3$ [Den06] in the nanostructure. As-prepared $Bi_{0.85}Sb_{0.15}$ nanowires show four different peaks in the spectra (blue plot) ascribed to the $A_{1g}$ first order vibrations mode of Bi atoms (at 98 $cm^{-1}$) [Tre09, Lan75], to the vibrations of $Sb_2O_3$ atoms (peaks at 121 and at 140 $cm^{-1}$) [Cod79], and to the $B_u$ mode of α-$Bi_2O_3$ (at 184 $cm^{-1}$)[Nar94]. Finally, the spectrum of $Bi_{0.85}Sb_{0.15}$ after annealing presents an intense peak at 144 $cm^{-1}$ ascribable to the $B_g$ mode of α-$Bi_2O_3$ [Nar94] as well as to a possible contribution of $Sb_2O_3$ atom oscillations, since also this material has a Raman band at this wavenumber [Den06]. Small bands were also detected at 206 and 228 $cm^{-1}$, ascribed to atom displacements in α-$Bi_2O_3$ in the $A_u$ [Nar94] and $A_g$ [Den97] mode, respectively.

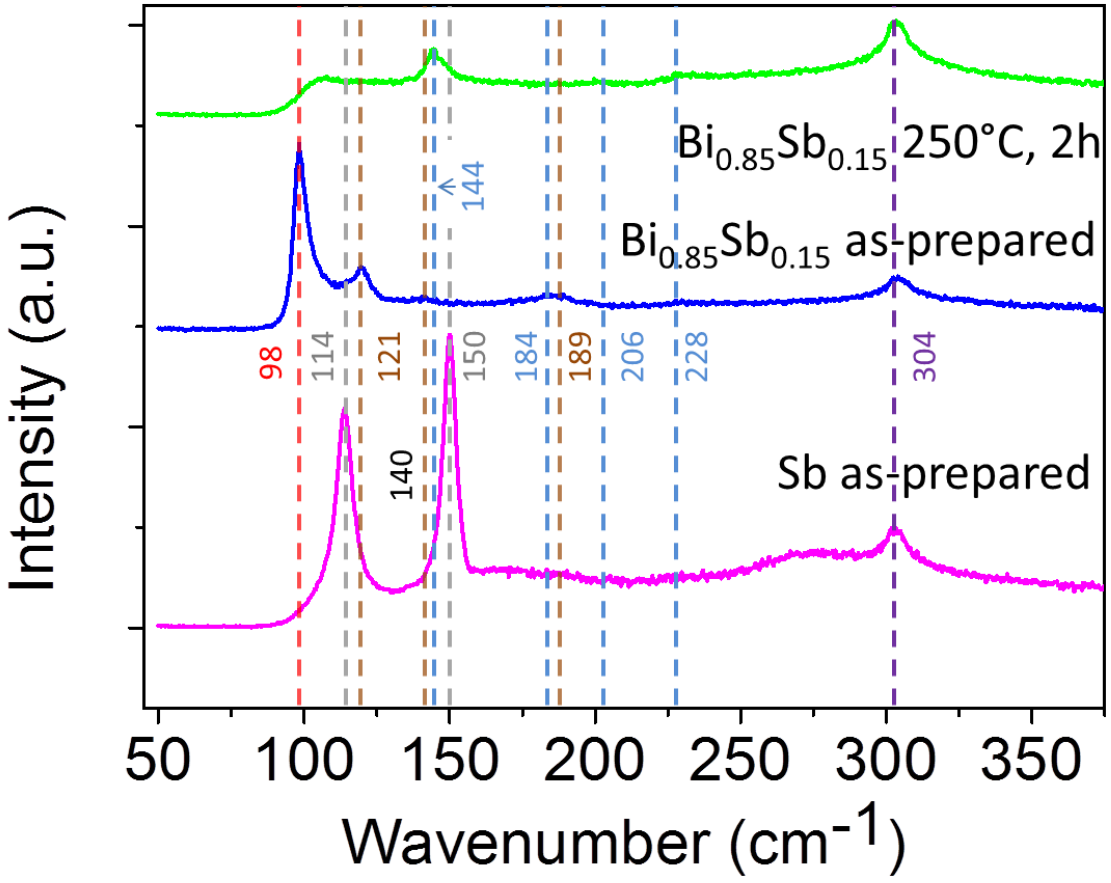


Figure 4.15: Raman spectra of $Bi_{0.85}Sb_{0.15}$ and Sb nanowires with diameter ~79 nm on Si substrate: (magenta plot) as-prepared Sb nanowire, (blue plot) as-prepared $Bi_{0.85}Sb_{0.15}$ nanowire and (green plot) $Bi_{0.85}Sb_{0.15}$ nanowire after annealing at 250°C for 2 hours. The vertical dashed lines indicate the wavenumber at which the peaks of the various atom vibrations are found: Bi atoms (dark red at 98 $cm^{-1}$), Sb atoms (grey at 114 and 150 $cm^{-1}$), Bi and O atoms in α-$Bi_2O_3$ (light blue at 144, 184, 206 and 226 $cm^{-1}$), Sb and O atoms in $Sb_2O_3$ (brown at 124, 144 and 189 $cm^{-1}$) and Si atoms (violet at 304 $cm^{-1}$).

In conclusion, Raman results give clear evidence that the oxidation process of Bi, $Bi_{0.85}Sb_{0.15}$ and Sb nanowires starts during or shortly after the dissolution of the polymer matrix. The presence of the Bi oxide phase explains the reported difficulties to provide good electrical contacts for single Bi nanowires [Cas15b, Cro01]. On the other hand, our Raman spectroscopy results together with the TEM-EDX results presented in section 4.5 indicate an interesting route to fabricate $Bi_2O_3$ nanowires by the oxidation of Bi nanowires under controlled annealing conditions. This allows us to study the annealing effects on the oxide wires. The results are presented in the next section.

## 4.6 Annealing Effects on $Bi_2O_3$ and $Sb_2O_3$ Nanowires

$Bi_2O_3$ is a semiconductor material characterized by a large bandgap ($E_g$ ~ 2.85 eV for the α-phase), high refractive index ($n$ ~ 2.9) and high dielectric permittivity ($\varepsilon_r$ = 190) as well as marked photoconductivity and photoluminescence [Qiu11, Qiu06]. These properties make Bi oxide suitable for a large range of applications, such as sensors, optical coating, photovoltaic cells and microwave integrated circuits [Fu97, Kan01]. Recently, the possible usage of interconnected photovoltaic and thermoelectric devices was discussed based on theoretical predictions pointing out an increase of the thermoelectric figure-of-merit of the system [Pen14].

Here, we present first studies on the thermal stability of $Bi_2O_3$ nanowires fabricated by controlled oxidation of Bi nanowires. Bi nanowires with initial diameter of ~ 30 nm were transferred onto a Si substrate and annealed for 20 hours at 250°C in air to completely transform them to $Bi_2O_3$. Several samples of oxidized Bi nanowires were then each further annealed for 20 hours at different temperatures near the $Bi_2O_3$ bulk melting point, reported to be 817°C [Cas15b].

Figure 4.16 displays sections of $Bi_2O_3$ nanowires fabricated by annealing of a Bi wire for 20 hours at 250°C before (a) and after annealing for 20 hours at (b) 700, (c) 750 and (d) 800°C in air. The wires in figure (b) and (c) exhibit a continuous structure, but the surfaces are rough and have few small protuberances. The roughness seems to increase with increasing annealing time. The annealing at 800°C results in the wires decay into chains of small spheres (figure 4.16 (d)). This disintegration is known as Rayleigh effect and has previously been reported for metallic nanowires (such as Ag [Vol15], Cu [Toi04a], Pt [Rau12] and Au [Kar06, Kar07]).

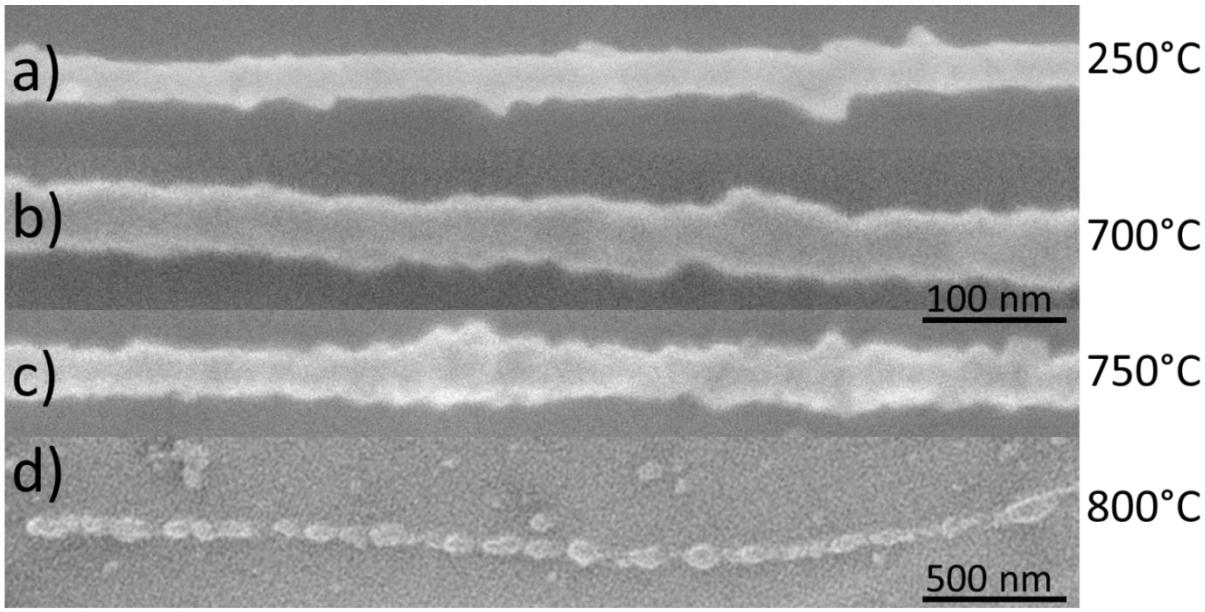


Figure 4.16: SEM images of section of (a) $Bi_2O_3$ nanowire produced by annealing of Bi nanowires with initial diameter 30 ± 4 nm for 20 hours at 250°C. The $Bi_2O_3$ nanowires were then subsequently annealed for 20 hours at (b) 700, (c) 750 and (d) 800°C. The scale bar is 100 nm for (a-c) and 500 nm for (d).

Also, $Sb_2O_3$ is considered as an interesting metal-oxide semiconductor material [Lou99] that was widely used in the past century as enclosure of electric devices [Sat98, Cha91].

To check the annealing behavior of this material, Sb nanowires with initial diameter of ~ 30 nm on a Si substrate were first oxidized by annealing for 20 hours at 600°C (temperature near Sb melting point (630°C) and then for 20 hours at 650°C. The final temperature is close to the melting point of bulk $Sb_2O_3$ (655°C). Due to the Si substrate, it was not possible to investigate the exact composition of the nanowire by means of SEM-EDX, because the signal from the wires was too low compared to the Si signal.

After 20 hours 600°C, the annealed Sb nanowires with initial diameter ~ 30 nm display undulations on the wire surface (figure 4.17 (a))). The absence of protuberances of the nanostructure underlines the different annealing effects with respect to Bi nanowires. After a further annealing of 20 hours at 650°C, the nanowires exhibit the formation of spherical features on the wire surface (figure 4.17 (b))) and, for some wires, the complete decomposition into a chain of spheres (figure 4.17 (c)). These wires obviously decayed according to the Rayleigh instability, similar to $Bi_2O_3$ nanowires. It is important to note that such long annealing times (20 + 20 hours) in air increases the amount of impurities on the Si substrate, making the focus of the image in the SEM difficult.

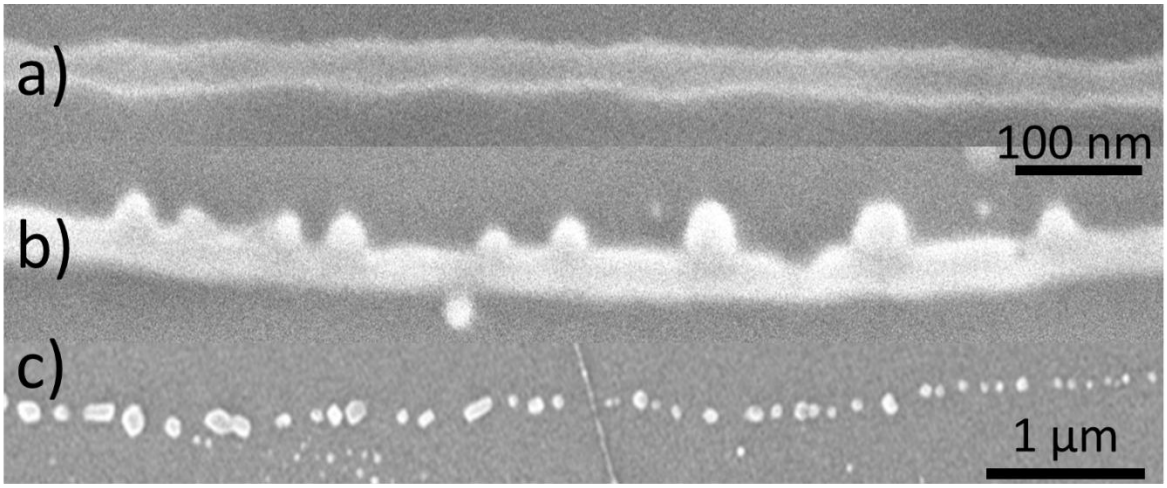


Figure 4.17: SEM images of section of Sb wires with initial diameter of 30 ± 4 nm annealed (a) first for 20 hours at 600°C for oxidation and then followed by (b, c) 20 hours at 650°C.

## 4.7 Resume of Thermal Annealing

Thermal annealing of electrodeposited Bi, $Bi_{1-x}Sb_x$ and Sb nanowires reveals several unexpected observations. In contrast to other metal wires, $Bi_{1-x}Sb_x$ nanowires, no evidences of Rayleigh instability at temperature near the melting point of Bi and Sb bulk material are detected.

The surface of Bi wires becomes rough after annealing at T < 200°C. Large protuberances develop at 250°C, which increase as the annealing time proceeds from 2 to 100 hours. TEM-EDX and Raman spectroscopy measurements provide clear evidence that oxidation started before annealing at the Bi wire surface and continues until the wires are fully transformed into $Bi_2O_3$.

The same morphological instabilities and oxidation appear for $Bi_{0.85}Sb_{0.15}$ wires. TEM-EDX measurements on annealed $Bi_{0.85}Sb_{0.15}$ show a homogenous presence of oxygen, Bi and Sb along the wire axis. At the wire surface, the Sb content is slightly higher, suggesting the existence of a thin Sb-rich shell (< 5 nm). The atomic percentage of Bi detected along the wire axis was found to be slightly higher (~ 88%) than the composition of the electrolyte (~ 85%) used for the wires growth.

Pure Sb nanowires display no protuberances after annealing. However, thin wires (~ 30 nm) show diameter fluctuations after annealing.

Pronounced oxidation effects of metallic Bi, $Bi_{1-x}Sb_x$ and Sb nanowires explain the reported difficulties for the electrical contacting of these wires. Moreover, our experiments reveal an interesting new approach to produce α-Bi2O3 under controlled annealing of metallic Bi nanowires. The nanowire

oxidation process starts at the surface and continues towards the inner part of the wire with longer annealing times.

The Rayleigh instability of fully oxidized Bi and Sb nanowires occurs at temperatures close the melting point of the oxide bulk material, specifically 800°C for $Bi_2O_3$ and 650°C for $Sb_2O_3$ wires, respectively.

Our results on oxidation and thermal stability need to be taken in consideration for possible future applications and implementation of $Bi_{1-x}Sb_x$ nanowires in thermoelectric systems and devices, since the exposition to ambient condition and heat is a fundamental requirement for such applications.

# Summary

$Bi_{1-x}Sb_x$ nanowires are an excellent model system to study the influence of size effects on the thermoelectric efficiency of the material. Given by the long Fermi wavelength of the electrons, quantization effects can be measured in $Bi_{1-x}Sb_x$ wires of relatively large diameter. Nanowires are also expected to be suitable to unravel contributions of the recently discovered metallic surface states of crystalline Bi in confined geometries to the thermoelectric properties. However this requires nanowires of well-defined structure and composition, because the thermoelectric properties of $Bi_{1-x}Sb_x$ are anisotropic and strongly depend on both parameters. The objective of this thesis was to fabricate nanostructures with tailored diameter, crystallographic orientation, crystallinity and composition and investigate the influence of the different wire parameters on the thermoelectric behavior.

In the first part of this thesis, $Bi_{1-x}Sb_x$ nanowires were synthesized by both potentiostatic and pulsed deposition in etched ion-track membranes. The influence of the deposition conditions on both wire composition and crystallographic orientation was studied. A more homogenous growth and larger single-crystalline segments within the nanostructure were obtained for samples grown by pulsed deposition. Systematic XRD and SEM-EDX analysis revealed that the preferential crystallographic orientation and the composition of the wires depend on the Bi:Sb ratio concentration in the electrolyte and to a smaller extend on the pore diameter. Based on this knowledge, it was possible to tailor the wire composition by varying the Sb concentration in the electrolyte.

For Seebeck coefficient and electrical resistance measurements, excellent thermal contacts are mandatory in order to reduce heat losses. Nanowires of defined structure and composition were mounted and thermally contacted in a special setup that was optimized for thermoelectric measurements. Bi, $Bi_{0.85}Sb_{0.15}$ and Sb nanowire arrays were characterized varying systematically the wire diameter from ~ 750 to ~ 40 nm. For all three compositions the Seebeck coefficients exhibit a non-monotonic behavior when decreasing the wire diameter. The data suggests three different regimes: (i) wires of diameters between ~ 750 and ~ 130 nm, with thermopower values similar to bulk material; (ii) wires of diameters between ~ 130 and ~ 60 nm, whose Seebeck coefficients decrease with decreasing diameter; (iii) thinnest wires of diameter below 60 nm, whose thermopower increases with decreasing wire diameter due to surface and/or inner states influences. These results are interpreted considering the contributions to the total thermopower from both surface and bulk states as well as from quantum-size effects. Our measurements provide the first systematic results of Seebeck

coefficients of $Bi_{1-x}Sb_x$ nanowire arrays as a function of wire diameter and composition, while maintaining all other parameters (wire length, measuring set up, surface) constant.

Finally, the chemical and thermal stability in air both at room and moderate temperatures of Bi, $Bi_{0.85}Sb_{0.15}$ and Sb nanowires were investigated, revealing the rapid formation of a metal-oxide phase layer after dissolution of the polymer template. During annealing the oxidation proceeds from the surface towards the center of the wires, causing an increase of the surface roughness at low annealing temperatures and the formation of protuberances at 250°C. Wire oxidation can explain the difficulties reported by other groups to electrically contact single $Bi_{1-x}Sb_x$ nanowires as well as the disparate and high values of the electrical resistance available in literature. The positive aspect of this finding is that annealing of Bi nanowires provides a well-controllable route for the synthesis of $Bi_2O_3$ nanowires under defined conditions. $Bi_2O_3$ is an interesting semiconductor material suitable for applications in many fields, such as sensors, photovoltaic cells and microwave integrated circuits.

# Bibliography

[Afs12] O. Afshar, R. Saidur, M. Hasanuzzaman, M. Jameel, "A review of thermodynamics and heat transfer in solar refrigeration system", *Renewable and Sustainable Energy Reviews 16 (2012) 5639.*

[Ala13] H. Alam, S. Ramakrishna, "A review on the enhancement of the figure of merit from bulk to nano-thermoelectric materials", *Nano Energy* 2 (2013) 190.

[Ang96] N. Angert, C. Trautmann, "Swift heavy ion tracks in materials", *Proceedings of the 7$^{th}$ international symposium on advanced nuclear energy research: recent progress in accelerator beam application (March 18-20, 1996), Tasaki (Japan).*

[Ape98] P. Apel, A. Schulz, R. Spohr, C. Trautmann, V. Vutsadakis, "Track size and track structure in polymer irradiated by heavy ions", *Nuclear Instruments and Methods in Physics Research B 146 (1998) 468.*

[Ast03] C.R. Ast, H. Hochst, "Electronic structure of a bismuth bilayer", *Physical Review B 67 (2003) 113102.*

[Ban86] M.L. Bansal, A.P. Roz, "Raman study of phonons and intraband electronic excitations in antimony", *Physical Review B 33 (1986) 1526.*

[Bäß13] S. Bäßler, T. Böhnert, J. Gooth, C. Schumacher, E. Pippel, K. Nielsch, "Thermoelectric power factor of ternary single-crystalline $Sb_2Te_3$- and $Bi_2TE_3$-based nanowires", *Nanotechnology* 24 (2013) 495402.

[Bea67] J.A. Bearden, "X-ray wavelengths", *Reviews of Modern Physics 39 (1967) 78.*

[Bej08] I. Bejenari, V. Kantser, "Thermoelectric properties of bismuth telluride nanowires in the constant relaxation-time approxiamtion", *Physical Review B 78 (2008) 115322.*

[Bel08] L.E. Bell, "Cooling, heating, generating power, and recovering waste heat with thermoelectric systems", *Science 321 (2008) 1457.*

[Bet30] H. Bethe, "Zur Theorie des Durchgangs schneller Korpuskular Strahlen durch Materie", *Annual Physik 5 (1930) 325.*

[Bhi05] G. Bhimarasetti, M. K. Sunkara, “Synthesis of Sub-20-nm-Sized Bismuth 1-d Structures Using Gallium-Bismuth Systems”, *Journal of Physical Chemistry Letters B* 109 (2005) 16219.

[Bla76] F.J. Blatt, P.A. Schroeder, C.L. Foiles, “Thermoelectric power of metals”, 227 West 17th Street, New York, Pleanum Press (1976).

[Blo33] F. Bloch, “Zur Bremsung rasch bewegter Teilchen beim Durchgang durch Materie”, *Annual Phyisik 16 (1933) 285.*

[Bou06] A. Boukai, K. Xu, J.R. Heath, “Size-Dependent Transport and Thermoelectric Properties of Individual Polycrystalline Bismuth Nanowires”, *Advanced Materials* 18 (2006) 864.

[Bra72] N.B. Brandt, S.M. Chudinov, V.G: Karavaev, “Investigation of gapless states in bismuth-antimony alloys under pressure”, *Soviet Physics JETP 34 (1972) 2*.

[Cao07] L. Cao, L. Laim, P.D. Valenzuela, B. Nabet, J.E. Spanier, “On the Raman Scattering from semiconducting nanowires”, *Journal of Raman Spectroscopy* 38 (2007) 697.

[Cas08] G. Casati, C. Mejia-Monasterio, T. Prosen, “Increasing thermoelectric efficiency: a dynamical systems approach”, *Physical Review Letters 101 (2008) 016601.*

[Cas15a] M. Cassinelli, S. Müller, Z. Aabdin, N. Peranio, O. Eibl, C. Trautmann, M.E. Toimil-Molares, “Structural and composition characterization of $Bi_{1-x}Sb_x$ nanowire arrays grown by pulsed deposition to improve growth uniformity”, *Nuclear Instruments and Methods in Physics Research B 365 (2015) 668.*

[Cas15b] M. Cassinelli, A. Romanenko, A. Reith, F. Völklein, F. Sigle, C. Trautmann, M.E. Toimil-Molares, ”Low temperature annealing effects on the stability of Bi nanowires”, *Physica Status Solidi A 213 (2015) 603.*

[Cha91] N. Chand, S. Verma, “Surface and Strenght Properties of PVC-$Sb_2O_3$ Flame Retardant Coated Sunhemp Fiber”, *Journal of Fire Sciences* 9 (1991) 251.

[Che12] L. Chen, F. Meng, F. Sun, ”Effect of the heat transfer on the performance of thermoelectric generator driven thermoelectric generator systems”, *Cryogenics 120 (2011) 58.*

[Chi04] P. Chiu, I. Shih, “A study of the size effect on the temperature-dependent resistivity of bismuth nanowires with rectangular cross-sections”, *Nanotechnology 15 (2004) 1489*.

[Cho09] J.Y. Chous, J.L. Lensch Falk, E.R: Hemesath, L.J. Lauhon, “Vanadium oxide nanowire phase and orientation analyzed by Raman spectroscopy”, *Journal of Applied Physics 105 (2009) 034310*.

[Cod79] C.A. Cody, L. Di Carlo, R.K. Darlington, “Vibrational and Thermal Study of Antimony Oxides”, *Inorganic Chemistry 18 (1979) 6*.

[Con14] E. Condrea, A. Nicorici, A. Gilewski, S. Matyjasik, “Thermopower peculiarities of uniaxial-strained bismuth nanowires”, *Journal of Low Temperature Physics 174 (2014) 232*.

[Cor05] T. Cornelius, J. Brötz, N. Chtanko, D. Dobrev, G. Miehe, R. Neumann, M.E. Toimil-Molares, “Controlled fabrication of poly- and single-crystalline bismuth nanowires”, *Nanotechnology 16 (2005) s246*.

[Cor06] T. Cornelius, M.E. Toimil-Molares, R. Neumann, S. Karim, “Finite-size effects in the electrical transport properties of single bismuth nanowires”, *Journal of Applied Physics 100 (2006) 114307*.

[Cor06b] T. Cornelius, M.E. Toimil-Molares, R. Neumann, G. Fahlsold, R. Lovrincic, A. Pucci, S. Karim, “Quantum size effects manifest in infrared spectra of single bismuth nanowires”, *Applied Physics Letters 88 (2006) 103114*.

[Cor06c] T. Cornelius, PhD thesis, University of Heidelberg (2006) pp.30-32.

[Cor10] T. Cornelius, B. Schiedt, D. Severin, G. Pepy, M. Toulemonde, P.Y. Apel, P.Boesecke, C. Trautmann, “Nanopores in track-etched polymer membranes characterized by small-angle x-ray scattering“, *Nanotechnology 21 (2010) 155702*.

[Cor10b] T. Cornelius, M.E. Toimil-Molares, “Finite- and Quantum-size Effects of Bismuth Nanowires“, Nanowires, book edited by: Paola Prete, ISBN 978-953-7619-79-4, pp.414 (2010) INTECH, Croatia.

[Cor11a] J.E. Cornett, O. Rabin, “Universal Scaling relations for the thermoelectric power factor of semiconducting nanostructures“, *Physical Review B 84 (2011) 205410*.

[Cor11b] J.E. Cornett, O. Rabin, “Thermoelectric figure of merit calculations for semiconduting nanowires“, Applied Physics Letters *98 (2011) 182104*.

[Cro01] S.B. Cronin, Y.M. Lin, P.L. Gai, O. Rabin, M.R. Black, G. Dresselhaus, M.S. Dresselhaus, "4-point Resistance Measurements of Individual Bi Nanowires", *Material Research Society Symposium Proceedings 635 (2001) C5.7.1.*

[Cuc62] P. Cucka, C.S. Barrett, "The crystal structure of Bi and of solid solutions of Pb, Sn, Sb, and Te in Bi", Acta Crystallographica *15 (1962) 865.*

[Cus58] N. Cusack, P. Kendall, "The Absolute Scale of Thermoelectric Power at High Temperature", *Proceedings Physics Society 72 (1958) 898.*

[Dal12] C.J: Dalmaschio, E.R. Leite, "Detachment induced by Rayleigh-Instability in metal oxide nanorods: insights from $TiO_2$", *Crystal Growth & Design 12 (2012) 3668.*

[Dav11] K. Davami, J.S. Lee, M: Meyyappan, "Nanowires in Thermoelectric Devices", *Transactions on Electrical and Electronic Materials 12 (2011) 227.*

[Deb13] J. De Boor, C. Stiewe, P. Ziolkowski, T. Dasgupta, G. Karpinski, E. Lenz, F. Edler, E. Mueller, "High-temperature measurement of Seebeck coefficient and electrical conductivity", *Journal of Electronic Materials 42 (2013) 7.*

[Deg07] O. Degtyareva, V.V: Struzhkin, R.J. Hemley, "High-pressure Raman spectroscopy of antimony: As-type, incommensurate host-guest, and bcc phases", *Solid State Communications 141 (2007) 164.*

[Deh03] F. Dehaye, E. Balanzat, E. ferain, R. Legras, "Chemical modifications induced in bisphenol A polycarbonate by swift heavy ions", *Instruments and Method in Physics Research B 209 (2003) 103.*

[Den97] V.N. Denisov, A.N. Ivlev, A.S. Lipin, B.N. Mavrin, V.G. Orlov, "Raman spectra and lattice dynamics of single-crystal α-$Bi_2O_3$", *Journal of Physics: Condensed Matter* 9 (1997) 4967.

[Den06] Z. Deng, F. Tang, D. Chen, X. Meng, L. Cao, B. Zou, "A Simple Solution Route to Single-Crystalline $Sb_2O_3$ Nanowires with Rectangular Cross Sections", *J. Phys. Chem. B 110 (2006) 18225.*

[DeS79] W. DeSorbo, "Ultraviolet effects and aging effects on etching characteristics of fission tracks in polycarbonate film", *Nuclear Tracks 3 (1979) 13.*

[Dism68] J.P. Dismukes, R.J. Paff, R.T. Smith, R. Ulmer, "Lattice Parameter and Density in Bismuth-Antimony Alloys", *Journal of Chemical and Engineering Data 13 (1968) 317.*

[Don09] E.U. Donev, R. Lopez, L.C. Feldman, R.F. Haglund, “Confocal Raman Microscopy across the Metal-Insulator Transition of Single Vanadium Dioxide Nanoparticles”, *Nano Letters 9 (2009) 702.*

[Dre99] M.S. Dresselhaus, G. Dresselhaus, X. Sun, Z. Zhang, S.B. Cronin, T. Koga, „Low-dimensional thermoelectric Materials“, *Physics of the Solid State 41 (1999) 679.*

[Dre03] M.S. Dresselhaus, Y.M. Lin, O. Rabin, A. Jorio, A.G. Souza Filho, M.A. Pimenta, R. Saito, Ge.G. Samsonidze, G. Dresselhaus, “Nanowires and nanotubes“, *Materials Science and Engineering C* 23 (2003) 129-140.

[Dre07] M.S. Dresselhaus, G. Chen, M.Y. Tang, R. Yang, H. Lee, D. Wang, Z. Ren, J.-P. Fleurial, P. Gogna, “New directions for low-dimensional thermoelectric materials“, *Advanced Materials 19 (2007) 1043.*

[Dut09] S. Dutta, V. Shubha, T.G. Ramesh, F. D’Sa, “Thermal and electronic properties of $Bi_{1-x}Sb_x$ alloys”, *Journal of Alloys and Compounds 467 (2009) 305.*

[Els14] M.H. Elsheikh, D.A. Shnawah, M.F.M.Sabri, S.B.M. Said, M.H. Hassan, M.B. A. Bashir, M. Mohamad, “A review on the thermoelectric renewable energy: Principle parameters that affect their performance“, *Renewable and Sustainable Energy Reviews 30 (2014) 337.*

[Eve60] T.E. Everhart, “Simple theory concerning the reflection of electron from solids”, *Journal of Applied Physics 31 (1960) 1483.*

[Eyi01] D. Eyidi, D. Maier, O. Eibl, M. Westphal, “Chemical Composition and Crystal Lattice Defects of $Bi_2Te_3$ Peltier Device Structures”, *Physics Status Solidi A 187 (2001) 585.*

[Fan13] Z. Fan, J.C. Ho, B. Huang, “One dimensional nanostructures for energy harvesting”, published by John Wiley & Sons, Oxford (2013) pp. 237-270.

[Far06] S. Farhangfar, ”Quantum size effects in one-dimensional semimetal”, *Physical Review B 74 (2006) 2053181.*

[Fis14] M. Fisac, F.X. Villasevil, A.M. Lopez, ”High-efficiency photovoltaic technology including thermoelectric generation”, *Journal of Power Sources 252 (2014) 264.*

[Fis83] B.E. Fisher, R. Spohr, “Production and use of nuclear tracks: imprinting structure on solids”, *Review Modern Physics 55 (1983) 907.*

[Fle65] R.L. Fleischer, P.B. Price, R.M. Walker, “Ion explosion spike mechanism for formation of charged-particle tracks in solids”, *Journal of Applied Physics* 36 (1965) 3645.

[Fle75] R.L. Fleischer, P.B. Price, R.M. Walker, “Nuclear Tracks in Solids”, University of California Press (1975).

[Fu97] J. Fu, “Electrical properties of glasses in the systems Bi2O3-RO-Li2O (R = Ca, Sr, Ba”, *Journal of Materials Science Letters 16 (1997) 1433.*

[Gal63] C.F. Gallo, B.S. Chandrasekhar, P.H. Sutter, “Transport Properties of Bismuth Single Crystals”, *Journal of Applied Physics 34 (1963) 1.*

[Gar72] N. Garcia, Y.H. Kao, M. Strongin, ”Galvanomagnetic Studies of Bismuth Films in the Quantum-Size-Effect Region”, *Physical Review B 5 (2011) 2029.*

[Gha10] P. Ghaemi, R.S.K. Mong, J.E. Moore, “In-plane transport and enhanced thermoelectric performance in thin films of the topological insulators $Bi_2Te_3$ and $Bi_2Se_3$”, *Physical Review Letters 105 (2010) 166603.*

[Goo15] J. Gooth, J.G. Glushke, R. Zierold, M. Leijnse, H. Linke, K. Nielsch, ”Thermoelectric performance of classical topological insulator nanowires”, *Semiconductors Science and Technology 30 (2015) 015015.*

[Glo77] D.A. Glocker, M..J. Skove, “Field effect and magnetoresistance in small bismuth wires”, *Physical Review B 15 (1977) 608.*

[Gmz12] http://www.gmzenergy.com.

[Gol07] J. Goldstein, D. Newbury, D. Joy, C. Lyman, P. Echlin, E. Lifshin, L. Sawyer, J. Michael, “Scanning Electron Microscopy and X-Ray Micronalaysis“, Springer-Edition, New York, Third Edition, pp 297 – 353 (2007).

[Gol10] H.J. Goldsmid, “Introduction to Thermoelectricity”, Springer-Verlag, Berlin, Heidelberg (2010).

[Hah05] T. Hahn, “International Tables for Crystallography Volume A: Space-Group Symmetry”, Springer (2005).

[Ham07] C.H. Hamann, A. Hammett, W. Vielstich,“Electrochemistry“, Wiley, VCH Verlag GmbH KGaA, 2007.

[Ham13] B. Hamdou, J. Kimling, A. Dorn, E. Pippel, R. Rostek, P. Woias, K. Nielsch, “Thermoelectric Characterization of Bismuth Telluride Nanowires, Synthesized Via Catalytic Growth and Post-Annealing“, *Advanced Materials 25 (2013) 239.*

[Har52] G.B. Harris, “Quantitative measurement of preferred orientation in rolled uranium bars” *Philosophical Magazine Series 7 (1952) 43:336, 113.*

[Har79] H.A. Harwing, A.G. Gerads, “The polymorphism of bismuth sesquioxide”, *Thermochim. Acta* 28 (1979) 121.

[Har02] T.C. Harman, P.J. Taylor, M.P. Walsh, B.E. LaForge, “Quantum dot superlattice thermoelectric materials and devices”, *Science 297 (2002) 2229.*

[Har05] P. Harrison, ”Quantum wells, wires and dots”, John Wiley & Sons edition, London (2005) pp. 243-270.

[Has09] Y. Hasegawa, D. Nakamura, M. Murata, H. Yasamoto, T. Komine, T. Taguchi, S. Nakamura, “Crystal orientation and transport properties of a 633-nm-diameter bismuth nanowire”, *Journal of Electronic Materials 40 (2009) 5.*

[Her00] J. Heremans, C.M. Trush, Y.-M. Lin, S. Cronin, Z. Zhang, M.S. Dresselhaus, J. F. Mansfield, “Bismuth nanowire arrays: Synthesis and galvanomagnetic properties“, Physical Review B 61 (2000) 2921 – 2930.

[Her01] J. Heremans, C.M. Trush, Y.-M. Lin, S.B. Cronin, M.S. Dresselhaus, “Transport properties of antimony nanowires”, *Physical Review B 63 (2001) 085406.*

[Her02] J. Heremans, C. Trush, D. Morelli, M.-C. Wu, “Thermoelectric power of bismuth nanocomposites”, *Physical Review Letters 88 (2002) 21.*

[Her05] J.P. Heremans, “Low-Dimensional Thermoelectricity”, *Acta Physica Polonica A, Proceedings of the XXXIV International School of Semiconducting Compounds, 108 (2005) 609.*

[Her99] J. Heremans, C.M. Trush, ”Thermoelectric power of bismuth nanowires”, *Physical Review B 59 (1999) 12579.*

[Hic93a] L.D. Hicks and M.S. Dresselhaus, “Thermoelectric figure of merit of one-dimensional conductor“, *Physical Review B* 47 (1993) 16631.

[Hic93b] L.D. Hicks and M.S. Dresselhaus, “Effect of quantum-well structures on the thermoelectric figure of merit“, *Physical Review B* 47 (1993) 12727.

[Hoc08] A.I. Hochbaum, R. Chen, R.D. Delgado, W. Liang, E.C. Garnett, M. Najarian, A. Majumdar, P. Yang, “Enhanced thermoelectric performance of rough silicon nanowires”, *Nature Letters 451 (2008) 163.*

[Hof06] Ph. Hofmann, “The surfaces of bismuth: structural and electronic properties”, Progress in *Surface Science 81 (2006) 191*.

[Höl97] G. Hölzer, M. Fritsch, M. Deutsch, J. Härtwig, E. Förster, “$K_{\alpha 1,2}$ and $K_{\beta 1,3}$ x-ray emission lines of the 3d transition metals”, *Physical Review A 56 (1997) 4554.*

[Hsi08] D. Hsieh, D. Qian, L. Wray, Y. Xia, Y.S. Hor, R.J. Cava, M.Z. Hasan, ”A topological Dirac insulator in a quantum spin Hall phase (first experimental realization of a 3D Topological Insulator”, *Nature 452 (2008) 970.*

[Hub09] T.E. Huber, A. Nikolaeva, L. Konopko, M.J. Graf, “Observation of three-dimensional behavior in surface states of bismuth nanowires and the evidence for bulk-Bi surface quasiparticles”, *Physical Review B 79 (2009) 201304(R).*

[Hub11] T.E. Huber, A. Adeyeye, A. Nikolaeva, L. Konopko, R.C. Johnson, M.J. Graf, “Surface state band mobility and thermopower in semiconducting bismuth nanowires”, *Physical Review B* 83 (2011) 235414.1 – 235414.5

[Hub12] T.E. Huber, K. Owusu, S. Johnson, A. Nikolaeva, L. Konopko, R.C. Johnson, M.J. Graf, Thermoelectric prospects of nanomaterials with spin-orbit surface bands“, *Journal of Applied Physics 111 (2012) 043709.*

[Huz11] D. Huzel, F. Völklein, M.C. Schmitt, H. Reith, ”Characterization and Application of Thermoelectric Nanowires”, in Nanowires-Implementations and Applications, ISBN: 978-953-307-318-7, InTech, Doi: 10.5772/19656 (2011).

[IEO09] International Energy Outlook 2009, http://eia.doe.gov/oiaf/ieo/pdf/world.pdf .

[In11] J. In, I. Yoon, K. Seo, J. Park, J. Choo, Y. Lee, B. Kim, ”Polymorph-Tuned Synthesis of α- and β-Bi2O3 Nanowires and Determination of Their Growth Direction from Polarized Raman Single Nanowire Microscopy”, *Chemistry a European Journal 17 (2011) 1304.*

[Ish09] Y. Ishikawa, Y. Hasegawa, H. Morita, A. Kurokouchi, K. Wada, T. Komine, H. Nakamura, “Resistivity and Seebeck coefficient measurements of a bismuth microwire array”, *Physica B 368 (2005) 163 – 167.*

[Iss79] J.P. Issi,”Low Temperature Transport Properties of the Group V Semimetals”, *Australian Journal of Physics 32 (1979) 585.*

[Iss06] J.P Issi, Thermoelectric Handbook: Macro to Nano, Taylor and Francis, New York (2006), pp 30.1 - 30.12.

[Jai59] A.L. Jain, “Temperature dependence of the electrical properties of Bismuth-Antimony alloys”, *Physical Review B 114 (1959) 6.*

[Kal12] N. Kalkan, E.A. Young, A. Celiktas, “Solar thermal air conditioning technology reducing the footprint of solar thermal air conditioning”, *Renewable and Sustainable Energy Reviews 16 (2012) 6352.*

[Kan01] E. Kanazawa, G. Sakai, K. Shimanoe, Y. Kanmura, Y. Teraokoa, N. Miura, N. Yamazoe, ”Metal oxide semiconductor $N_2O$ sensor for medical use”, *Sensor and Actuators B 77 (2001) 72.*

[Kar06] S. Karim, M.E. Toimil-Molares, A.G. Balogh, W. Ensinger, T. Cornelius, E.U. Khan, R. Neumann, ”Morphological evolution of gold nanowires controlled by Rayleigh instability”, *Nanotechnology 17 (2006) 5954.*

[Kar07] S. Karim, M.E. Toimil-Molares, W. Ensinger, A.G. Balogh, T. Cornelius, E.U. ´Khan, R. Neumann, ”Influence of crystallinity on the Rayleigh instability of gold nanowires”, *Journal of Applied Physics D 40 (2007) 3767.*

[Kas01] S. Kasap, “Thermoelectric Effects in Metals: Thermocouples”, e-booklet © S.O. Kasap 1997-2001, web material.

[Kim14] J. Kim, S. Lee, Y.M. Brovman, M. Kim, P. Kim, W. Lee, “Weak antilocalization and conductance fluctuation in a single crystalline Bi nanowire”, *Applied Physics Letters 104 (2014) 043105.*

[Kim15] J. Kim, S. Lee, Y.M. Brovman, P. Kim, W. Lee, ”Diameter-dependent thermoelectric figure of merit in single-crystalline Bi nanowires” *Nanoscale 7 (2015) 5053.*

[Koj15] D. Kojda, R. Mitdank, M. Handweg, A. Mogilatenko, M. Albrecht, Z. Qang, J. Ruhhammer, M. Kroener, P. Woias, S.F. Fischer, “Temperature-dependent thermoelectric properties of individual silver nanowires”, *Physical Review B 91 (2015) 024302.*

[Kol03] A. Kolmakov, Y. Zhang, M. Moskovits, ”Topotactic Thermal Oxidation of Sn Nanowires: Intermediate Suboxides and Core-Shell Metastable Structures” *Nano Letters 3 (2003) 1125.*

[Kum93] G.S. Kumar, G. Prasad, R.O. Pohl, “Experimental determinations of the Lorenz number”, *Journal of Materials Science 16 (1993) 4261.*

[Kuz96] A.B. Kuz´menko, E.A. Tischchenko, V.G. Orlov, ”Transverse optic modes in monoclinic α-$Bi_2O_3$”, *Journal of Physics: Condensed Matter 8 (1996) 6199.*

[Lan75] J.S. Lannin, J.M. Calleya, M. Cardona, ”Second-order Raman scattering in the group-$V_b$ semimetals: Bi, Sb, and As” *Physical Review B 12 (1975) 585.*

[Lax60] B. Lax, J.G. Mavroides, H.J. Zieger, R.J. Keyes, “Infrared magnetoreflection in bismuth”, *Physical Review Letters 5 (1960) 241.*

[Len96] B. Lenoir, M. Cassart, J. Michenaud, H. Scherrer, S. Scherrer, ”Transport properties of Bi-rich Bi-Sb alloys”, *Journal of Physics and Chemistry of Solids 57 (1996) 89.*

[Len96b] B. Lenoir, A. Dauscher, M. Cassart, Y.I. Ravich, H. Scherrer, “Effect of antimony content on the the thermoelectric figure of merit of Bi1-xSbx alloys”, *Journal Physics Chemistry Solids 59 (1998) 129.*

[Len98] B. Lenoir, A. Dauscher, M. Cassart, Y.I. Ravich, H.J. Scherrer, “Effect of antimony content of the thermoelectric figure of merit of $Bi_{1-x}Sb_x$ alloys“, *Journal of Physics and Chemistry Solids 59 (1998) 129.*

[Li10] J.-F. Li, W.-S. Liu, L.-D. Zhao, M. Zhou, “High-performance nanostructured thermoelectric materials“, *NPG Asia Materials 2 (2010)152.*

[Lid92] D.R. Lide,“ CRC Handbook of Chemistry and Physics: a ready Reference Book of Chemical and Physical Data“, CRC Press (1992).

[Lim15] J. Limmer, L. Medlin, P. Siegal, M. Hekmaty, J.L. Lnesch-Falk, K. Erickson, J. Pillars and W. Graham Yelton, *Journal of Material Research 30 (2015) 2.*

[Lin00] Y.-M. Lin, X. Sun, M.S. Dresselhaus, "Theoretical investigation of thermoelectric transport of cylindrical Bi nanowires", *Physical Review B 62 (2000) 4610.*

[Lin00b] Y.-M. Lin, S.B. Cronin, J.Y. Ying, M.S. Dresselhaus, J.P. Heremans, "Transport properties of Bi nanowire arrays", *Applied Physics Letters 76 (2000) 3944.*

[Lin02] Y.-M. Lin, O. Rabin, S.B. Cronin, J.Y. Ying, M.S. Dresselhaus, "Semimetal-semiconductor transition in $Bi_{1-x}Sb_x$ alloy nanowires and their thermoelectric properties", *Applied Physics Letters 81 (2002) 13.*

[Lin02b] Y.-M. Lin, S.B. Cronin, O. Rabin, J.Y. Zing, M.S. Dresselhaus, "Thermoelectric properties of $Bi_{1-x}Sb_x$ nanowire arrays", *Material Research Society Symposium Proceedings 691 (2002) G10.6.*

[Liu12] W. Liu, X. Yan, G. Chen, Z. Ren, "Recent advances in thermoelectric nanocomposites", *Nano Energy 1 (2012) 42.*

[Lon99] M. Longerey, J.M. Cuesta, P. Gaudon, A. Crespy, "Talcs and brominated trimethylphenyl indane/$Sb_2O_3$ blend in a PP-PE copolymer", *Polymer Degradation and Stability* 64 (1999) 489.

[Mah96] G.D. Mahan, J.O. Sofo, "The best thermoelectric", *Proceedings of the National Academy of Sciences USA 93 (1996) 7436.*

[Mar03] M. S. Martin-Gonzalez, A. L. Prieto, M. S. Knox, R. Gronsky, T. Sands, A. M. Stacy, "Electrodeposition of $Bi_{1-x}Sb_x$ Films adn 200-nm Wire Arrays from a Nonaqueous Solvent", *Chemical Materials 15 (2003) 1676.*

[Mei01] M.M. Meier, G. Reitz, "Determination of charge states of single swift heavy projectiles by high-energy delta-electrons", *Radiation Measurements 34 (2001) 281.*

[Mob12] Mobay Chemical Corporation Product Information, Makrofol (2012).

[Moo09] A.L. Moore, M.T. Pettes, F. Zhou, L. Shi, "Thermal conductivity suppression in bismuth nanowires", *Journal of Applied Physics 106 (2009) 034310.*

[Mot71] N.F. Mott, E.A. Davis, "Electronic processes in non-crystalline material", Oxford University Press (1971).

[Mül12a] S. Müller, C. Schötz, O. Picht, W. Sigle, P. Kopold, M. Rauber, I. Alber, R. Neumann, M.E. Toimil-Molares, “Electrochemical Synthesis of Bi1-xSbx Nanowires with Simultaneous Control on Size, Composition and Surface Roughness“, *Crystal Growth & Design 12 (2012) 615.*

[Mül12b] S. Müller, PhD thesis, University of Heidelberg (2012).

[Nab13] Y. Nabatame, T. Matsumoto, Y. Ichige, T. Komine, R. Sugita, M. Murata, Y. Hasegawa, ”Numerical analysis of the boundary scattering effect on transport properties in Bi-Sb nanowires”, *Journal of Electronic Materials 42 (2013) 7.*

[Nak11] F. Nakamura, Y. Kousa, A.A. Taskin, Y. Takeichi, A. Nishide, A. Kakizaki, M. D´Angelo, P. Lefevre, F. Bertran, A. Talb-Ibrahimi, F. Komori, S. Kimura, H. Kondo, Y. Ando, I. Matsuda, “Topological transition in $Bi_{1-x}Sb_x$ studied as function of Sb doping”, *Physical Review B 84 (2011) 235308.*

[Nak11b] D. Nakamura, M. Murata, H. Yamamoto, Y. Hasegawa, T. Komine, “Thermoelectric properties for single crystal bismuth nanowires using a mean free path limitation model”, *Journal of Applied Physics 110 (2011) 053702.*

[Nar94] S.N. Narang, N.D. Patel, V.B. Kartha, ”Infrared and Raman spectral studies and normal modes of α-$Bi_2O_3$”, *Journal of Molecular Structure 327 (1994) 221.*

[Nik08] A. Nikolaeva, T.E. Huber, D. Gitsu, L. Konopko, ”Diameter-dependent thermopower of bismuth nanowires”, *Physical Review B 77 (2008) 035422.*

[Nol01] G.S. Nolas, J. Sharp, H.J. Goldsmid, “Thermoelectrics”, Springer-Verlag, Berlin-Heidelberg (2001).

[Oat72] C.W. Oatley, “The scanning electron microscope”, Cambridge University Press, Cambridge (UK), pp.194-196.

[Okr11] G.S. Okram, N. Kaurav, “Size-dependent resisitivity and thermpower of nanocrystalline copper”, *Journal of Applied Physics 110 (2011) 023713.*

[Ome08] A.M. Omer, “Focus on low carbon technologies: The positive solution”, *Renewable and Sustainable Energy Reviews 12 (2008) 2331.*

[Pen14] G. Pennelli, ”Review of nanostructured devices for thermoelectric applications”, *Beilstein Journal of Nanotechnology 5 (2014) 1268.*

[Pep07] G. Pepy, P. Boesecke, A. Kuklin, E. Manceau, B. Schiedt, Z. Siwy, M. Toulemonde, C. Trautmann, “Cylindrical nanochannels in ion-track polycarboante membranes studied by small-angle X-ray scattering“, *Journal of Applied Crystallography 40 (2007) s388.*

[Per07] N. Peranio, O. Eibl, ”Quantitative EDX microanalysis of $Bi_2Te_3$ in the TEM”, *Physica Status Solidi A 204 (2007) 3243.*

[Per12] N. Peranio, M. Winkler, D. Bessas, Z. Aabdin, J. König, H. Böttner, R.P. Hermann, O. Eibl, ”Room-temperature MBE deposition thermoelectric properties and advanced structural of binary $Bi_2Te_3$ and $Sb_2Te_3$ thin films”, *Journal of Alloys and Compounds 521 (2012) 163.*

[Pet95] F. Peterson, W. Enge, “Energy loss dependent transversal etching rates of heavy ion track ion tracks in plastic”, *Radiation Measurements 25 (1995) 43.*

[Pro] http://www.prolimatech.com/en/products/detail.asp?id=163&subid=1528#showtab

[Qiu06] Y. Qiu, D.F. Liu, J.H. Yang, S.H. Yang, ”Controlled Synthesis of Bismuth Oxide Nanowires by an Oxidative Metal Vapor Transport Deposition Technique”, *Advanced Materials 18 (2006) 2604.*

[Qiu11] Y. Qiu, M. Yang, H. Fan, Y. Zuo, Y. Shao, Y. Xu, ”Phase-transitions of α- and β-$Bi_2O_3$ nanowires”, *Materials Letters 65 (2011) 780.*

[Rab01] O. Rabin, Y.M. Lin, M.S. Dresselhaus, “Anomalously high thermoelectric figure of merit in Bi1-xSbx nanowires by carrier pocket alignment”, *Applied Physics Letters 79 (2001) 81.*

[Rau12] M. Rauber, F. Münch, M.E. Toimil-Molares, W. Ensinger, ”Thermal stability of electrodeposited platinum nanowires and morphological transformations at elevated temperatures”, *Nanotechnology 23 (2012) 475710.*

[Rei98] L. Reimer, “Scanning Electron Microscopy: physics of image formation and microanalysis”, Springer series in optical sciences, Vol. 45 (1998).

[Rep07] J. Reppert, R. Rao, M. Skove, J. He, M. Craps, T. Tritt, A. M. Rao, ”Laser-assisted synthesis and optical properties of bismuth nanorods”, *Chemical Physics Letters 442 (2007) 334.*

[Row06] D.M. Rowe, Thermoelectric Handbook: Macro to Nano, Taylor and Francis, New York (2006), pp 1.1 - 1.10.

[Saf01] K. Safa, E-booklet: “Thermoelectric Effects in Metals: Thermocouples”, http://Materials.Usask.Ca (2001).

[Sal11] R. Salh, “Defect related luminescence in silicon dioxide network: a review, crystalline silicon – properties and uses”, Prof. Sukumar Basu (ed.), ISBN: 978-953-307-587-7, Intech, DOI: 10.5772/22607. Available from http://www.intechopen.com/crystalline-silicon-properties-and-uses/defect-related-luminescence-in-silicon-dioxide-network-a-review .

[Sam99] N.M. Sammers, G.A. Tompsett, H. Nafe, F. Aldinger, ”Bismuth based oxide electrolytes structure and ionic conductivity”, *Journal of the European Ceramic Society 19 (1999) 1801.*

[Sat98] H. Sato, K. Kondo, S: Tsuge, H. Ohtani, N. Sato, “Mechanism of thermal degradation of a polyester flame-retarded with antimony oxide/brominated polycarbonate studied by temperature-programmed analytical pyrolisis”, *Polymer Degradation and Stability 62 (1998) 41.*

[See26] T.J. Seebeck, “Über die magnetische Polarisation der Metalle und Erze durch Temperatur-Differenz”, *Annalen der Physik 3 (1826) 253.*

[Sel13] A. Sellitto, V.A. Cimmelli, D. Jou, “Thermoelectric effects and size dependency of the figure-of-merit in cylindrical nanowires”, *International Journal of Heat and Mass Transfer 57 (2013) 109.*

[Sha08] L.S. Sharath Chandra, A. Lakhani, D. Jain, S. Pandya, P.N. Vishwakarma, M. Gangrade, V. Ganesan, ”Simple and precise thermoelectric power measurement setup for different environments”, *0*79 (2008) 103907.

[Shi12] L Shi, “Thermal and thermoelectric transport in nanostructures and low-dimensional systems”, *Nanoscale and Microscale Thermophysical Engineering 16 (2012) 79.*

[Sin03] M.P: Singh, C.M. Bhandari, “Thermoelectric properties of bismuth telluride quantum wires”, *Solid State Communications 127 (2003) 649.*

[Sny08] G.J. Snyder, E.S. Toberer, “Complex thermoelectric materials”, *Nature Materials 7 (2008) 105.*

[Som07] J. Sommerlate, K. Nielsch, H. Böttner, “Thermoelektrische Multilatente“, *Physik Journal 6 (2007) 35.*

[Soo09] J.R. Sootsman, D.Y. Chung, M.G. Kanatzidis, “New and old concepts in thermoelectric materials“, *Angewandte Chemie International Edition 48 (2009) 8616.*

[SPP] Bi (JCPDS-44-1246, PDF-2, Sets 1-89), Sb (JCPDS-35-732, PDF-2, Sets 1-89), Au (JCPDS-4-784, PDF-2, Sets 1-89) ***S****tandard* ***P****owder* ***P****atterns*.

[Sta12] S. A. Stanley, C. Stuttle, A. J. Caruana, M. D. Cropper, A. S. O. Walton, "An investigation of the growth of bismuth whiskers and nanowires during physical vapour deposition", *Journal of Physics: Applied Physics D 45 (2012) 435304.*

[Su14] S. Su, T. Liu, Y. Wang, X. Chen. J. Wang, J. Chen, "Performance optimization analyses and parametric design criteria of a dye-sensitized solar cell thermoelectric hybrid device", *Applied Energy 120 (2014) 16.*

[Sun03] Y. Sun, Z. Zhu, Z. Wang, Y. Jin, J. Liu, M. Hou, Q. Zhang, "Swift heavy ion induced amorphisation and chemical modification in polycarbonate", *Nuclear Instruments and Methods in Physics Research B 209 (2003) 188.*

[Szc11] J.R. Szczech, J.M. Higgins, S: Jin, "Enhancement of the thermoelectric properties in nanoscale and nanostructured materials", *Journal of Materials Chemistry 21 (2011) 4037.*

[Tak12] R. Takahashi, S. Murakami, "Thermoelectric transport in topological insulators", *Semiconductor Science and Technologies 27 (2012) 124005.*

[Tan07] X. Tang, W. Xie, H. Li, W. Zhao, Q. Zhang, M. Niinom, "Preparation and thermoelectric transport properties of high-performance p-type $Bi_2TE_3$ with layered nanostructure", *Applied Physics Letters 90 (2007) 012102.*

[Tan09] C. J. Tang, G. H. Li, X. C. Dou, Y. X. Zhang, L. Li, "Thermal Expansion Behaviors of Bismuth Nanowires", *Journal of Physics and Chemistry C 113 (2009) 5422.*

[Tan12] S. Tang, M.S. Dresselhaus, "Phase diagrams of $Bi_{1-x}Sb_x$ thin films with different growth orientations", *Physical Review B 86 (2012) 075436.*

[Tan14a] S. Tang, M.S: Dresselhaus, "Electronic phases, band gaps, and band overlaps of bismuth antimony nanowires", *Physical Review B 89 (2014) 045424.*

[Tan14b] S. Tang, M.S. Dresselhaus, "Electronic properties of nano-structured bismuth-antimony materials", *Journal of Materials Chemistry C 2 (2014) 4710.*

[Tan15] S. Tang, M.S. Dresselhaus, "Electronic phases, band gaps, and band overlaps of bismuth antimony nanowires", *Physical Review B 89 (2014) 045424.*

[Teo08] J.C.Y. Teo, L. Fu, C.L. Kane, „Suface states and topological invariants in three-dimensional topological insulators: applications to $Bi_{1-x}Sb_x$“, *Physical Review B 78 (2008) 045426.*

[TES11] TES NewEnergy Corporation, Retrieved November 2011 from http://www.tes-ne.com/ .

[Tho51] W. Thomson, “On the dynamical theory of heat transport“, *Research Society Science 3 (1851) 91.*

[Tie13] S.F. Tie, C.W. Tan, “A review of energy sources and energy management system in electric vehicles“, *Renewable and Sustainable Energy Reviews 20 (2013) 82.*

[Toi01] M.E. Toimil-Molares, V. Buschmann, D. Dobrev, G. Miehe, R. Neumann, R. Scholz, I.U. Schuchert, J. Vetter, “Single-Crystalline Copper Nanowires Produced by Electrochemical Deposition in Polymeric Ion Track Membranes“, *Advanced Materials 13 (2001) 62.*

[Toi03] M.E. Toimil-Molares, E.M. Höhberger, Ch. Schaeflein, R.H. Blick, R. Neumann, C: Trautmann, “Electrical characterization of electrochemically grown single copper nanowires“, *Applied Physics Letter 82 (2003) 13.*

[Toi04a] M.E. Toimil-Molares, A.G. Balogh, T. Cornelius, R. Neumann, C. Trautmann, “Fragmentation of nanowires driven by Rayleigh instability”, *Applied Physics Letters 85 (2004) 22.*

[Toi04b] M.E. Toimil-Molares, N. Chtanko, T. Cornelius, D. Dobrev, I. Enculescu, R.H. Blick, R. Neumann, “Fabrication and contacting of single Bi nanowires”, *Nanotechnology 15 (2004) s201.*

[Toi12] M.E. Toimil-Molares, “Characterization and properties of micro- and nanowires of controlled size, composition and geometry fabricated by electrodeposition and ion-track technology“, *Beilstein Journal of Nanotechnology 3 (2012) 860.*

[Tra95] C. Trautmann, “Observation and chemical treatment of heavy-ion tracks in polymers”, *Nuclear Instruments and Methods in Physics Research B 105 (1995) 81.*

[Tra96] C. Trautmann, W. Brüchle, R. Spohr, J. Vetter, N. Angert, “Pore geometry of etched ion tracks in polymide”, *Nuclear Instruments and Methods in Physics Research B 111 (1996) 70.*

[Tra10] C. Trautmann, "Particle Acceleration and Detection“, Springer-Verlag Berlin Heidelberg, (2010) pp 369-387.

[Tre09] K. Trentelman, ”A note on the characterization of bismuth black by Raman microspectroscopy”, *Journal of Raman Spectroscopy 40 (2009) 585.*

[Tri11] T.M. Tritt, “Thermoelectric Phenomena Materials, and Applications”, *The Annual Review of Material Research´s 41 (2011) 433.*

[Ung01] T. Ungar, J. Gubicza, G. Ribariki, A. Borbely, “Crystallite size distribution and dislocation structure determined by diffraction profile analysis: principles and practical application to cubic and hexagonal crystals”, *J. Appl. Crystal. 34 (2001) 777.*

[Vec74] M.P. Vecchi, M.S. Dresselhaus, “Temperature dependence of the band parameters of bismuth”, *Physical Review B 10 (1974) 2.*

[Ven01] R. Venkatasubramanian, E. Siivola, T. Colpitts, B. O´Quinn, “Thin-film thermoelectric devices with high room-temperature figures of merit”, *Nature 413 (2001) 597.*

[Ver03] P.M. Vereecker, S. Ren, L. Sun, P.C. Searson, “Electrodeposition of $Bi_{1-x}Sb_x$ thin films”, *Journal of the Electrochemical Society 150 (2003) c131.*

[Vin10] C.J. Vineis, A. Shakouri, A. Majumdar, M.G. Kanatzdis, “Nanostructured Thermoelectrics: Big Efficiency Gains from Small Features”, *Advanced Materials 22 (2010) 3970.*

[Vol15] A. Volk, D. Knez, P. Thaler, A.W: Hauser, W. Grogger, F. Hofer, W.E. Ernst, “Thermal instabilities and Rayleigh breakup of ultrathin silver nanowires grown by nanodroplets”, *Physical Chemistry Chemical Physics 17 (2015) 24570.*

[Völ09] F. Völklein, M. Schmitt, T. Cornelius, O. Picht, S. Müller, R. Neumann, ”Microchip for the Measurement of Seebeck Coefficients of Single Nanowires”, *Journal of Electronics Materials 38 (2009) 1109.*

[Völ09b] F. Völklein, H. Reith, T. Cornelius, M. Rauber, R. Neumann, “The experimental investigation of thermal conductivity and the Wiedemann-Franz law for single metallic nanowires”, *Nanotechnology 20 (2009) 325706.*

[Wan94] Z.G. Wang, C. Dufour, E. Paumier, M. Toulemonde, “The $S_e$ sensitivity of metals under swift-heavy-ion irradiation: a transient thermal process”, *Journal of Physics: Condensed Matter 6 (1994) 6733.*

[Wan12] W. Wang, M. Liu, Z. Yang, W. Mai, J. Gong, ”Synthesis and Raman optical properties of single-crystalline Bi nanowires”, *Physica E 44 (2012) 1142.*

[Wan12b] Y. Wang, Y. Sui, F. Li, L. Xu, X. Wang, W. Su, X. Liu, ”Thermoelectrics in misfit-layered oxides: From bulk to nano”, *Nano Energy 1 (2012) 456.*

[Wan13] H. Wang, W.D. Porter, H. Böttner, J. König, L. Chen, S. Bai, T.M. Tritt, A. Mayolet, J. Senawiratne, C. Smith, F. Harris, P. Gilbert, J.W. Sharp, J. Lo, H. Kleinke, L. Kiss, “Transport Properties of bulk thermoelectrics- an international round-robin study, Part 1: Seebeck coefficient and electrical resistivity”, *Journal of Electronic Materials 42 (2013) 4.*

[Wan15] Y. Wang, J. He, S. Yu, H. Chen, “Exploiting rayleigh instability in creating parallel Au nanowires with exotic arrangements”, *Small* http://dx.doi.org/10.1002/smll.201503211

[Wag15] M.F.P. Wagner, F. Völklein, H. Reith, C. Trautmann, M.E. Toimil-Molares, “Fabrication and thermoelectrical characterization of three dimensional nanowire networks”, *Physica Status Solidi A* http://dx.doi.org/10.1002/pssa.201532616

[Wer09] H. Werheit, U. Kuhlmann, B. Herstell, W. Winkelbauer, “Reliable measurement of Seebeck coefficient in semiconductors”, *Journal of Physics: Conference Series 176 (2009) 012037.*

[Wha12] Z. Whang, M. Kroner, P. Woias, ”Design and fabrication of a thermoelectric nanowire characterization platform and nanowire assembly by utilizing dielectrophoresis ”, *Sensors and Actuators A 188 (2012) 417.*

[Wie53] G. Wiedemann, R. Franz, ”Über die Wärme-Leitungsfähigkeit der Metalle”, *Annalen der Physik und Chemie 8 (1853) 497.*

[Wil96] D.B. Williams, C.B. Carter, “Transmission Electron Microscopy (A Text Book for Material Science“, Plenum Press, New York (1996).

[Xi07] H. Xi, L. Luo, G. Fraisse, “Development and applications of solar-based thermoelectric technologies”, *Renewable and Sustainable Energy Reviews 11 (2007) 923*.

[Yao06] W.M. Yao, “Passage of particles through matter”, *Journal of Physics G 33 (2006) 258.*

[Yad11] G.G. Yadav, J.A. Susoreny, G. Zhang, H. Yang, Y. Wu, “Nanostructure-based thermoelectric conversion: an insight into the feasibility and sustainability for large scale deployment”, *Nanoscale 3 (2011) 3555.*

[Yam02] O. Yamashita, S. Tomiyoshi, “Effect of geometrical shape on magneto-Peltier and Ettingshausen cooling in Bi and Bi0.88Sb0.12 polycrystals”, *Journal of Applied Physics 92 (2002) 3794.*

[Yan08] J. Yang, D. Wang, L. Yang, Y. Zhang, G. Xing, J. Lang, H. Fan, M. Gao, Y. Wang, ”Effects of suply time of Ar gas gas current on structural properties of Au-catalyzed ZnO nanowires on silicon (110) grown by vapor-liquid-solid process”, *Journal of Alloys and Compounds 450 (2008) 508.*

[Yim72] W.M. Yim, A. Amith, “Bi-Sb alloys for magneto-thermoelectric and thermomagnetic cooling”, *Solid State Electronics 15 (1972) 1141.*

[Zha05] F. Zhang, R. Barrowcliff, S.T. Hsu, “Thermal Stability of $IrO_2$ Nanowires”, *Proceedings of the 2005 International Conference on MEMS, NANO and Smart Systems (ICMENS 05) (2005).*

[Zha06] Y. Zhang, L. Li, G.H. Li, L.D. Zhang, ”Electrical transport properties of single-crystal antimony nanowire arrays”, *Physical Review B 73 (2006) 113403.*

[Zho05] J. Zhou, C. Jin, J.H. Seol, X. Li, L. Shi, “Thermoelectric properties of individual electrodeposited bismuth telluride nanowires”, *Applied Physics Letters 87 (2005) 133109.*

[Zho07] B. Zhou, X.-H. Li, J.-J. Zhu, “Controllable Synthesis of One-Dimensional Chinelike Superstructures of Homogenous Bi100-xSbx Alloys via a Template-Free Electrodeposition”, *Crystal Growth & Design 7 (2007) 2276.*

[Zie04] J.F. Ziegler, “SRIM-2003”, *Nuclear Instruments and Methods in Physical Research Section B 219 (2004) 1027.*

[Zue09] Y.M. Zuev, W. Chang, P. Kim, “Thermoelectric and Magnetothermoelectric transport Measurements of Graphene”, *Physical Review Letters 102 (2009) 096807.*

# Acknowledgments

With great pleasure I want to thank the many people who have supported and contributed to the success of this work:

- First of all I want to thank Prof. Dr. Christina Trautmann for supervising and supporting my doctoral work. I sincerely appreciate that she gave me the possibility of working in the Material Research Department at GSI and to attend several interesting international conferences and workshops where I presented my work within the framework of the group's international collaborations.

- Dr. M.E. Toimil-Molares for helping and guiding me during these years of work with many suggestions and ideas. I want to thank her also for the interesting and deeply corrections of this and other manuscripts.

- Prof. Dr. Wolfgang Ensinger from the Technical University of Darmstadt for acting as a second referee for this dissertation.

- Prof. Dr. Friedemann Völklein from the Hochschule RheinMain for acting as external supervisor during these years and for the helpful suggestions and interesting discussions.

- Prof. Dr. Robert Stark from The Technical University of Darmstadt to be part of the commission of my final exam.

- Dr. K.-O. Voss for his patient helps and suggestions for the development of the setup and many other devices.

- Dr. W. Sigle of the Max Planck Institute for Intellige Systems of Stuttgart for introducing me in the field of TEM and measuring interesting properties of my wire, which were very helpful for the conclusions of the second publication.

- Dr. N. Peranio from the Institute for Applied Physics of Tübingen for the TEM measurements of my wire and precious helps and suggestions during the development of the first publication.

- Dr. J. Gooth from the University of Hamburg for the infinite and awesome discussions about the field of the wire surface states and their influences.

- The whole group of the Material Research Department of GSI for the very pleasant working conditions and diverting coffee breaks. In particular, I want to thank Michael, Janina, Anne, Ina, Katharina and Christian (Danke schön), Wouter (Heel hartelijk bedankt), Liana (շատ շնորհակալություն), Loic (Merci beaucoup), Alexey and Anton (большое спасибо) for the infinite supports and encouragements during these years. They are not only outstanding colleagues but also precious friends.

- The GSI football team "Unified Field Heroes", which I have the honor to lead as Captain (der Spielführer). I want to thank all the players with nicknames: Alex, Cebayogi, Orona, Spiderleg, Black Sheep, Tomàs, Nena, Valente, Dexu, Temisnike, Txorflaks, Lollipop, Lili, Bee Do, Cayt, Christoph, Segfault, Good Sam, Samwise, Ironman, Wazinho…. I want to thank all for the awesome football time and for the funny evenings spent together.

- Here, I want to thank also the new friends met at GSI (Francesco, Enrico, Dimitri, Peter, Daria, Fabio, Damian, Sofija, Namita, ….) and the old friends at home (Giulia, Gerardo, Giulio, Emanuele, Marcone, ….) which always support me and cheer me up whenever needed.

Finally, I would like to thank my family for their constant encouragements and optimisms in this adventure in a new country. In particular, I thank from the bottom of my heart my darling Darya. Her daily supports and smile made easier to achieve the end of this work.

Grazie mille a tutti!!!!

*Marco*

# List of Publications

[1] **M. Cassinelli**, A. Romanenko, A. Reith, F. Völklein, F. Sigle, C. Trautmann, M.E. Toimil-Molares, ”Low temperature annealing effects on the stability of Bi nanowires”, *Physica Status Solidi A 213 (2016) 603.*

[2] **M. Cassinelli**, S. Müller, Z. Aabdin, N. Peranio, O. Eibl, C. Trautmann, M.E. Toimil-Molares, “Structural and composition characterization of $Bi_{1-x}Sb_x$ nanowire arrays grown by pulsed deposition to improve growth uniformity”, *Nuclear Instruments and Methods in Physics Research B 365 (2015) 668.*

[3] C. Jean, L. Belliard, T. Cornelius, O. Thomas, M.E. Toimil-Molares, **M. Cassinelli**, L. Becerra, B. Perin, “Direct observation of gigahertz coherent guided acoustic phonons in free-standing single copper nanowires”, *The Journal of Physical Chemistry Letters 5 (2014) 4100.*

[4] L. Belliard, T. Cornelius, B. Perrin, N. Kacemi, L. Becerra, O. Thomas, M.E. Toimil-Molares, **M. Cassinelli**, “Vibrational response of free standing single copper nanowire through transient reflectivity microscopy”, *Journal of Applied Physics 114 (2013) 193509.*

*In preparation:*

**M. Cassinelli**, S. Müller, K.-O. Voss, C. Trautmann, F. Völklein, J. Gooth, K. Nielsch, M.E. Toimil-Molares, “Study of the Influence of Surface States and Size Effects on the Seebeck coefficient and electrical resistance of $Bi_{1-x}Sb_x$ Nanowires Arrays”, *to be submitted (2016).*

*Scientific Reports:*

[a] **M. Cassinelli**, A. Romanenko, W. Sigle, C. Trautmann, and M.E. Toimil-Molares, “Annealing Effects on the Morphology and Composition of Thermoelectric Bi Nanowires fabricated by Ion-track technology”, *Annual Report 2015 of the faculty Materials and Geo Sciences, Ion-beam Modified Materials, to be printed (2015).*

[b] S. Müller, **M. Cassinelli**, K.-O. Voss, C. Trautmann, M.E. Toimil-Molares, "Seebeck Measurements on $Bi_{1-x}Sb_x$ Nanowire Arrays", *GSI Scientific Report 2013-1, p.416 (2013).*

[c] O. Picht, J. Gronenfeld, **M. Cassinelli**, S. Müller, C. Trautmann, M.E. Toimil-Molares, "Influence of Electrolyte Concentration on Crystal Orientation and Seebeck Coefficient of $Bi_2Te_3$ Nanowire Arrays", *GSI Scientific Report 2013-1, p.415 (2013).*

[d] Y.H. Chen, M.E. Toimil-Molares, S. Müller, I. Alber, **M. Cassinelli**, J. Liu, C. Trautmann, "Synthesis CuNi coreshell nanowires by a twostep etching and electrodeposition", *GSI Scientific Report 2013-1, p.419 (2013).*

# Curriculum Vitae

**Personal Details**

Name: Marco Cassinelli

Date of Birth: 01.04.1986

Birthplace: Mantova (Italy)

**Education**

09/2011 - 06/2016 **PhD student** in the Department of Materials and Earth Science at the Technical University of Darmstadt in the group of "Ion-Beam Modified Materials" under the supervision of Prof. Dr. Christina Trautmann.

Topic: Investigation of the thermoelectric properties of $Bi_{1-x}Sb_x$ nanowire arrays electrodeposited in etched ion-track membranes.

**External PhD student** of the GSI Helmholtz Centre for Heavy Ion Research GmbH, Department of Material Science under the supervision of Dr. Maria Eugenia Toimil-Molares.

03/2009 - 03/2011 **Master student** in physics with specialization in solid state physics at the University of Bologna, Bologna (Italy).

Degree: Master of Science in Physics

Title of the thesis: "Optoelectronic properties of Nitride Based Heterostructure", under the supervision of Prof. Dr. Daniela Cavalcoli.

09/2005 – 03/2009 **Bachelor student** in physics at the University of Bologna, Bologna (Italy).

Degree: Bachelor of Science in Physics

Title of the thesis: "The project EEE (Extreme Energy Events): installation and data analysis of a muon telescope", under the supervision of Prof. Dr. Gabriella Sartorelli.